Norwegian University of
Science and Technology

A study on commercial SiC-powders sintered by hot pressing

Kent Mogstad

Materials Science and Engineering
Submission date: June 2016
Supervisor: Kjell Wiik, IMTE
Co-supervisor: Mari-Ann Einarsrud, IMT
Pål Runde, Saint-Gobain Ceramic Materials AS Lillesand

Norwegian University of Science and Technology
Department of Materials Science and Engineering

Declaration

I declare that the work described in this project report has been performed independently and in accordance with the rules and regulations for examinations at NTNU, the Norwegian University of Science and Technology.

Kent Mogstad

Trondheim, June 10th, 2016

Abstract

Hot-pressing of a commercial silicon carbide powder was performed with 0, 5 and 10wt% added hexagonal boron nitride. Density, microstructural and compositional development has been studied *ex situ* with different holding times at sintering temperature. Although other authors have reported poor sinterability for this type of composite, hot-pressing was shown to result in >99% dense materials. Grain growth was restrained, and X-ray diffraction showed no other phases or compounds than BN and graphite with the additions. Hot-pressed SiC-BN composites are therefore promising as self-lubricating, high-performance ceramics, and should be mechanically tested.

The microstructure of the sample containing the highest amount of boron nitride showed signs of exaggerated grain growth upon reaching the sintering temperature, with subsequent recrystallization. A boron-carbon exchange mechanism between SiC and BN is proposed, based on BNC_x-regions detected in Si-B-C-N polymers. The mechanism is believed to assist vacancy formation in SiC, increasing the sinterability of SiC-BN composites. GDOES measurements and XRD scans support the existence of BNC_x regions in the samples with 5 and 10 wt% BN.

Sammendrag

Hot-pressing av kommersielle silisiumkarbidpulver ble utført med 0, 5 og 10 vektprosent tilsatt heksagonal bornitrid. Endringer i tetthet, mikrostruktur og sammensetning ble analysert *ex situ* med forskjellige holdetider på sintringstemperatur. Selv om andre forfattere har rapportert dårlige sintringsegenskaper for lignende materialer, ble det dokumentert >99% tette prøver med 10 vektprosent bornitrid med hot-pressing. Kornvekst ble begrenset, og røntgendiffraksjon viste ingen andre faser enn grafitt og bornitrid ved tilsats av BN. Hot-pressede SiC-BN kompositter er dermed lovende som selvsmørende høy-ytelseskeramer, og mekaniske egenskaper bør undersøkes.

Mikrostrukturen til prøven med høyest innhold av bornitrid viste tegn til overdreven kornvekst allerede ved starten av sintring, deretter rekrystalliserte kornene seg. En utvekslingsmekanisme mellom bor og karbon er foreslått mellom SiC og BN, basert på BNC_x-områder funnet i Si-B-C-N polymerer. Mekanismen kan bidra til vakansformasjon i SiC, som bidrar positivt i sintringsegenskapene til SiC-BN kompositter. Optisk emisjonsspektroskopi med glødeutladning og røntgenanalyse støtter formasjon av BNC_x-regioner i prøvene med 5 og 10 vektprosent BN.

Acknowledgements

I would like to thank my main supervisor Kjell Wiik at IMT and co-supervisor Pål Runde at Saint-Gobain for guidance, support, and the opportunity to work with silicon carbide in cooperation between NTNU and the industry. Second, I want to thank Development Engineer Benoit Watremetz at Saint-Gobain and Professor Mari-Ann Einarsrud at IMT for valuable input and guidance. Special thanks to Sergey Khromov and Yingda Yu at IMT, as well as other staff, PhD-candidates and students at IMT who have assisted me in my work and in my breaks. I thank God for always watching over me, and Hanne, thank you for letting me be yours.

Table of contents

Declaration i

Abstract ii

Sammendrag iii

Acknowledgements v

1 Introduction 1

1.1 Background 1

1.2 Aim 1

2 Theory 3

2.1 Silicon carbide 3
2.1.1 Properties 4
2.1.2 Structure 5
2.1.3 Thermodynamic stability and polytype transition 8
2.1.4 Production of silicon carbide by the Acheson process 9

2.2 Hexagonal boron nitride 13

2.3 Theory of sintering 15
2.3.1 Global driving forces for sintering 15
2.3.2 Local driving force for sintering 18
2.3.3 Mass transport mechanisms 20
2.3.4 Sintering stages 21

2.4 Sintering silicon carbide 23
2.4.1 The effect of boron addition 23
2.4.2 The effect of carbon additions 25
2.4.3 The effect of boron nitride additions 27

2.5 Si-(B-)C-N ceramics and phase equilibriums 28

2.6 Glow Discharge Optical Emission Spectroscopy (GDOES) 32

2.7 Electron Backscatter Diffraction 34

3 Experimental 37

3.1 Powders and Equipment 37

3.2 Procedures 39
3.2.1 Powder preparation 39
3.2.2 Hot-press description 39
3.2.3 Sintering procedure 40
3.2.4 X-ray diffraction 41
3.2.5 Glow Discharge Optical Emission Spectroscopy (GDOES) 41
3.2.6 Electron Backscatter Diffraction 41

4 Results 43

4.1 Powder description 43

4.2 Densities ... 44
4.3 X-ray diffraction ... 45
4.4 Electron backscatter diffraction ... 49
4.5 Glow discharge optical emission spectroscopy ... 53
5 Discussion ... 57
5.1 Densification ... 57
5.2 Composition ... 57
5.3 Microstructure ... 59
6 Conclusions and further work ... 61
References ... 63
7 Appendix A – Product specification for the SiC powder before spray drying 68
8 Appendix B – Datasheet for spray dried SiC ... 69
9 Appendix C – Density measurements ... 70
10 Appendix D – Stacked XRD scans ... 71
11 Appendix E – All EBSD figures ... 73
12 Appendix F – Secondary electron images of EBSD surfaces with scanned area highlighted ... 75
13 Appendix G – Weight percent to atomic percent calculations ... 78
14 Appendix H – Lattice parameter and d-spacing measurements ... 79

List of Figures

FIGURE 1. THE BASIC TETRAHEDRAL UNIT OF ALL SILICON CARBIDE POLYTYPE STRUCTURES. [18]......................... 5

FIGURE 2. STACKING OF TETRAHEDRA IN THE SIC STRUCTURES. TOP: STACKING WITHOUT ROTATION, MAY BE TAKEN AS THE TWO FIRST LAYERS IN THE CUBIC STACKING ABC… MIDDLE: THE A LAYER SEEN FROM ABOVE, SHOWING THAT EVERY SECOND LAYER IS OUT OF THE PLANE OF THE PAPER. BOTTOM: STACKING WITH ROTATION, MAY BE TAKEN AS THE REPEATING AC' UNIT OF THE SMALLEST HEXAGONAL STRUCTURE, 2H. [10] (ADAPTED FROM [16]) 6

FIGURE 3. SOLID TETRAHEDRA MODELS FOR THE FOUR MOST COMMON SIC POLYTYPE STRUCTURES, TOGETHER WITH "TRAMLINE" STRUCTURE DIAGRAMS. 'ABC' AND RAMSDELL NOTATION SHOWN BELOW [16]. (A) 3C ABCABC (B) 6H ABCB'A'C' (C) 4H ABA'C' (D) 15R ABCB'A'BCAC'B'CABA'C' 7

FIGURE 4. AMOUNT OF POLYTYPES AFTER ANNEALING OF 90% 6H A-SIC DOPED WITH 2WT% BORON (ARGON ATMOSPHERE, 2150°C). [25].. 9

FIGURE 5. SCHEMATIC OF CROSS AND LONGITUDINAL SECTIONS OF A FURNACE RUNNING THE ACHESON PROCESS. (A) ARE REMOVABLE SIDE WALLS MADE OUT OF REFRACTORY BRICKS, (B) ARE REFRACTORY END WALLS AND (C) ARE ELECTRODES. [10] 9

FIGURE 6. SECTIONS OF THE FURNACE AFTER THE ACHESON PROCESS RUN. APPROXIMATE CROSS SECTION DIAMETERS IN MM. [10]... 10

FIGURE 7. EQUILIBRIUM PRESSURES OF SIO AND/OR CO_2 FOR REACTIONS BETWEEN CARBON AND SILICA. PRESSURES FOR REACTION (3), (4) AND (5) ARE CALCULATED FOR P_{CO} = 1BAR, AND (4) WITH $P_{SiO} = P_{CO2}$. THERMAL DISSOCIATION OF SILICA FOR COMPARISON, WITH THE ASSUMPTION $P_{O2} = ½ P_{SiO}$. [10] 12

FIGURE 8. CRYSTAL STRUCTURE OF HEXAGONAL BORON NITRIDE (H-BN) COMPARED TO GRAPHITE. [32] 13

FIGURE 9. SCANNING ELECTRON MICROGRAPH OF NECK GROWTH BETWEEN 32 μM NICKEL SPHERES DURING SINTERING AT 1050ºC FOR 30 MIN IN VACUUM. PRIOR TO SINTERING THE PARTICLES WERE LOOSELY PACKED INTO A CRUCIBLE.[34] 15

FIGURE 10. SCHEMATIC OF PARTICLE CHANGES DURING SINTERING. SHRINKAGE IS NOTICEABLE. [36]......... 16

FIGURE 11. SKETCH ILLUSTRATING THE CHANGE IN GRAIN SHAPE THAT OCCURS DURING HOT-PRESSING. GRAINS ARE FLATTENED IN THE DIRECTION OF THE APPLIED PRESSURE. IF MATTER TRANSPORT OCCURS BY DIFFUSION, GRAIN BOUNDARY SLIDING IS NECESSARY TO ACCOMMODATE THE CHANGE IN GRAIN SHAPE. [37] 17

FIGURE 12. CHANGE IN SURFACE ENERGY E_S AS A FUNCTION OF AVERAGE PARTICLE SIZE *A*. 18

FIGURE 13. SCHEMATIC OF VACANCY FLUX ON A CURVED SURFACE. [44] 19

FIGURE 14. SCHEMATIC OF MECHANISMS THAT CONTRIBUTE TO MATERIAL TRANSPORT IN SINTERING OF A POLYCRYSTALLINE POWDER. [44] 20

FIGURE 15. SCHEMATIC OF SINTERING STAGES DURING SINTERING OF SPHERICAL PARTICLES (A) IN CONTACT AT THE ONSET OF SINTERING, (B) NEAR THE END OF THE INITIAL SINTERING STAGE, AS NOTED BY NECK FORMATION, (C) INTERMEDIATE STAGE WITH NECK GROWTH AND (D) FINAL STAGE OF SINTERING. NOTE HOW PARTICLES ARE CLOSER TO TETRADEKAIDECAHEDRAL IN SHAPE IN (C) AND (D). THERE IS CONTINUOUS POROSITY ALONG EDGES IN (C), AND CLOSED PORES AT EACH CORNER IN (D). [44]...................................... 21

FIGURE 16. EQUILIBRIUM DIHEDRAL ANGLE (A) BETWEEN TWO GRAINS AND (B) INSIDE A PORE. [37]................... 22

FIGURE 17. FRACTIONAL CHANGE IN LATTICE PARAMETER *C* OF 6H-SIC AS A FUNCTION OF B CONCENTRATION. OPEN CIRCLES ARE EXPERIMENTAL VALUES, WHILE SOLID LINES SHOW CALCULATED VALUES IF BORON REPLACED ONLY SI OR C LATTICE POINTS. [53] 24

FIGURE 18. SCHEMATIC REPRESENTATION OF SINTERED DENSITY OF SILICON CARBIDE WITH CHANGES IN (A) CARBON AND (B) BORON ADDITIONS. THERE WAS A CONSTANT BORON ADDITIONS (A), AND CONSTANT CARBON ADDITIONS (B). [47] (ADAPTED FROM [54]) 24

FIGURE 19. SCHEMATIC REPRESENTATION OF SINTERED DENSITY VARIATION WITH INCREASING BORON ADDITIONS FOR SIC POWDERS WITH DIFFERENT PARTICLE SIZES. [47] (ADAPTED FROM [55])....................... 25

FIGURE 20. OXYGEN CONTENT AS A FUNCTION OF TEMPERATURE FOR A) SIC CONTAINING 3WT% CARBON B) PURE SIC. [65] 26

FIGURE 21. WEIGHT LOSSES DURING SINTERING FOR THE FOLLOWING SYSTEMS: A) PURE SIC B) SIC CONTAINING 0.5WT% B C) SIC CONTAINING 3WT% C D) SIC CONTAINING 3WT% C AND 0.5WT% B. [65] .. 26

FIGURE 22. X-RAY DIFFRACTOGRAMS OF VARIOUS SI-(B-)C-N CERAMICS IN THE AS-THERMOLYZED (PRODUCED FROM POLYMERS) STATE AND AFTER ANNEALING AT ELEVATED TEMPERATURES FOR 4H (TEMPERATURE SHOWN IN TOP-RIGHT CORNER). THE BRAGG PEAKS CORRESPONDING TO THE CRYSTALLIZED PHASE ARE MARKED: SIC (●), A-SI_3N_4 (◊) AND B-SI_3N_4 (□). THE BROAD STRUCTURE MARKED ○ IS REMINISCENT OF AN AMORPHOUS PHASE. [68] 28
FIGURE 23. ISOTHERMAL SECTIONS IN THE SI-B-C-N SYSTEM AT T = (A) 1673 K AND (B) 2273 K. [71] 29
FIGURE 24. CONCENTRATION SECTIONS IN THE SI-B-C-N SYSTEM AT CONSTANT BORON CONTENT (10 AT%) AND TEMPERATURES (A) 1673 K AND (B) 2273 K. [71] 29
FIGURE 25. HRTEM IMAGE OF POLYMER DERIVED SI-B-C-N CERAMIC AFTER ANNEALING AT 1800°C FOR 50 H IN NITROGEN ATMOSPHERE. [72] 30
FIGURE 26. SCHEMATIC ILLUSTRATION OF PHASE SEPARATION OF $SI_AC_CN_D$ AND $SI_AB_BC_CN_D$ COMPOSITIONS, FALLING WITHIN THE LIMIT OF THE THREE-PHASE REGION SIC-SI3N4-C AND THE FOUR-PHASE REGION SIC-SI3N4-BN-C OF THE QUATERNARY SI-B-C-N SYSTEM, RESPECTIVELY. [70] 30
FIGURE 27. TEMPERATURE-ACTIVITY (A_C) DIAGRAM IN THE SI-C-N SYSTEM. PRESSURES ARE NITROGEN PARTIAL PRESSURES. [71] 31
FIGURE 28. ILLUSTRATION OF THE GDOES PROCESS. IN PHASE 1, ARGON ATOMS ARE IONIZED AND BOMBARD THE CATHODE SURFACE. IN PHASE 2, SAMPLE AND ARGON ATOMS AND IONS, AS WELL AS ELECTRONS, ARE EJECTED FROM THE SAMPLE SURFACE AND JOIN THE PLASMA IN THE FIRING CHAMBER. IN PHASE 3, THE ATOMS ARE EXCITED BY ELECTRONS AND IONS IN THE PLASMA, AND WILL THEN EJECT A PHOTON. THIS PHOTON WILL THEN BE ANALYZED BY AN OPTICAL SPECTROMETER. [76] 32
FIGURE 29. ILLUSTRATION OF SAMPLE AND EBSD DETECTOR PLACEMENT DURING EBSD OPERATION. [83] 34
FIGURE 30. SCHEMATIC OF ELECTRON DIFFRACTION IN SILICON WITH CRYSTAL PLANES AND ASSOCIATED DIFFRACTION BANDS SHOWN. [83] 35
FIGURE 31. PARTICLE SIZE DISTRIBUTION, SPECIFIC SURFACE ENERGY AND CHEMISTRY OF THE SILICON CARBIDE STARTING POWDER BEFORE SPRAY DRYING. 37
FIGURE 32. PICTURE OF THE HOT-PRESS. 39
FIGURE 33. PICTURE OF GRAPHITE MOLDS USED FOR HOT-PRESSING. 39
FIGURE 34. SCHEMATIC DRAWING OF THE HOT-PRESS USED IN THIS WORK. 39
FIGURE 35. STANDARD HOT-PRESSING PROGRAM FOR SINTERING SIC-0BN. 40
FIGURE 36. AGGLOMERATE SIZE DISTRIBUTION MEASURED BY DRY LASER DIFFRACTION FOR THE AUTHOR'S SPECIALIZATION PROJECT. [81] 43
FIGURE 37. CUMULATIVE AGGLOMERATE SIZE DISTRIBUTION MEASURED BY DRY LASER DIFFRACTION FOR THE AUTHOR'S SPECIALIZATION PROJECT. [81] 43
FIGURE 38. SECONDARY ELECTRON IMAGE OF SIC 5BN POWDER FOR THE AUTHOR'S SPECIALIZATION PROJECT. [81] 44
FIGURE 39. SECONDARY ELECTRON IMAGE OF SIC 0BN POWDER FOR THE AUTHOR'S SPECIALIZATION PROJECT. [81] 44
FIGURE 40. SECONDARY ELECTRON IMAGE OF SIC 10BN POWDER FOR THE AUTHOR'S SPECIALIZATION PROJECT. [81] 44
FIGURE 41. DENSITIES OF HOT-PRESSED SAMPLES, AS MEASURED BY ARCHIMEDES' PRINCIPLE. THE RED LINE CORRESPONDS TO THE TEMPERATURE REACHED IN THE HOT-PRESSING PROGRAM. 44
FIGURE 42. DENSITIES OF SAMPLES HELD AT 2050°C FOR DIFFERENT TIMES. 45
FIGURE 43. STACKED XRD SCANS FOR SIC 10BN SAMPLES. (□) SIGNIFIES SIC 4H FROM *TOPAS* STRUCTURE FITTING, (○) SIC 6H FROM COD #9010158, (■) BN FROM COD #9008997, (●) GRAPHITE FROM COD #9008569. NOTE THAT THE SCANS ARE STACKED IN ASCENDING ORDER OF HOT-PRESSING, WHILE THE LEGEND IS IN DESCENDING ORDER. THE 46
FIGURE 44. XRD-SCANS OF SIC 0BN ZOOMED AT THE BN-C PEAKS IN THE RANGE 25-30°. THE GRAPHITE PEAKS ARE MARKED WITH (●). 46
FIGURE 45. XRD-SCANS OF SIC 10BN ZOOMED AT THE BN-C PEAKS IN THE RANGE 25-30°. (■) SIGNIFIES BN-PEAK, (●) GRAPHITE PEAK. 46
FIGURE 46. XRD SCANS FOR SIC 10BN SHOWING SMALL CHANGES IN LATTICE PARAMETER FOR SIC WITH SINTERING. (□) SIGNIFIES SIC 4H, (○) SIC 6H. 47

Figure 47. Changes in c-parameter for 6H SiC as measured by *Topas* software. The lines are a guide to the eye. 47
Figure 48. d-spacing for BN and graphite peaks, as measured manually in *EVA* software. The lines are a guide to the eye. 48
Figure 49. 4H to 6H ratio as measured by Rietveld fitting in *Topas*. The lines are a guide to the eye. 48
Figure 50. Phase map for the area scanned in Fig. 50, SiC 0BN 60 min 49
Figure 51. Secondary electron image of the area scanned for ESBD analysis of SiC 0BN 60min. 49
Figure 52. Inverse pole figure for the area scanned in Fig. 50, SiC 0BN 60min. 50
Figure 53. Inverse pole figures of sintered SiC 0BN with 0 (left), 30 (middle) and 60 min (right) holding time. The scale bar is 15 μm. 50
Figure 54. IPF images of sintered SiC 5BN with 0 (left), 30 (middle) and 60 min (right) holding time. The scale bar is 15 μm. 51
Figure 55. IPF images of sintered SiC 10BN with 0 (left), 30 (middle) and 60 min (right) holding time. The scale bar is 15 μm. 51
Figure 56. Inverse pole figures for SiC 0BN sintered at 60 min. Viewing angle is parallel (left) and normal (right) to pressure direction. The scale bar is 15 μm. 51
Figure 57. IPF images for SiC 5BN 60 min with viewing angle parallel to (left) and normal to (right) pressing direction. The scale bar is 15 μm. 52
Figure 58. IPF images for SiC 10BN 60 min with viewing angle parallel to (left) and normal to (right) pressing direction. The scale bar is 15 μm. 52
Figure 59. 4H to 6H ratio measured in the EBSD scans. The lines are a guide for the eye. 52
Figure 60. GDOES profiles for samples hot-pressed for 60 min. Note that the detected voltage cannot be directly converted to weight percent; it is also influenced by atomic weight and bonding properties. The final depth of the measurement was measured in SEM to be between 30 and 40 μm for all samples. 53
Figure 61. Average value for the last 10 seconds of GDOES analysis, separated by element, powder and holding time at sintering temperature. Detected voltage has been replaced with arbitrary units, as voltages for different elements cannot be related without a reference. The final depth of the measurement was between 30 and 40 μm (measured in SEM). 54
Figure 62. GDOES measurements for carbon, reprinted from Fig. 61. The intensities are average values for the last 10 seconds of each measurement. 58
Figure 63. Product specification for SiC powder used before spray drying. Delivered by Development Engineer Benoit Watremetz at Saint-Gobain Ceramic Materials AS Lillesand. 68
Figure 64. Datasheet for Densitec 13H, a ready-to-press (RTP) powder produced by Saint-Gobain. Delivered by Development Engineer Benoit Watremetz at Saint-Gobain Ceramic Materials AS Lillesand. 69
Figure 65. Stacked XRD scans for SiC 0BN. 71
Figure 66. Stacked XRD scans for SiC 5BN. 71
Figure 67. Stacked XRD scans for SiC 10BN. 72
Figure 68. IPF and phase map for SiC 0BN 0min. 73
Figure 69. IPF and phase map for SiC 0BN 30min. 73
Figure 71. IPF and phase map for SiC 0BN 60min with viewing angle normal to pressing direction. 73
Figure 70. IPF and phase map for SiC 0BN 60min. 73
Figure 72. IPF and phase map for SiC 5BN 0min. 73
Figure 73. IPF and phase map for SiC 5BN 30min. 73
Figure 75. IPF and phase map for SiC 5BN 60min with viewing angle normal to pressing direction. 74
Figure 74. IPF and phase map for SiC 5BN 60min. 74
Figure 77. IPF and phase map for SiC 10BN 30min. 74
Figure 76. IPF and phase map for SiC 10BN 0min. 74

FIGURE 79. IPF AND PHASE MAP FOR SIC 10BN 60MIN WITH VIEWING ANGLE NORMAL TO PRESSING DIRECTION.......... 74
FIGURE 78. IPF AND PHASE MAP FOR SIC 0BN 60MIN. 74
FIGURE 80. ELECTRON IMAGES OF POLISHED SIC 0BN SAMPLES WITH 0MIN (TOP LEFT), 30 (TOP RIGHT) AND 60 MINUTE (BOTTOM) SINTERING TIME. BOTTOM RIGHT IS VIEWED NORMAL TO PRESSING DIRECTION, THE REST PARALLEL. THE RED SQUARE IS THE AREA SCANNED IN EBSD. THE SCALE BAR IS 60 μM.......... 75
FIGURE 81. ELECTRON IMAGES OF POLISHED SIC 5BN SAMPLES WITH 0MIN (TOP LEFT), 30 (TOP RIGHT) AND 60 MINUTE (BOTTOM) SINTERING TIME. BOTTOM RIGHT IS VIEWED NORMAL TO PRESSING DIRECTION, THE REST PARALLEL. THE RED SQUARE IS THE AREA SCANNED IN EBSD. THE SCALE BAR IS 60 μM.......... 76
FIGURE 82. ELECTRON IMAGES OF POLISHED SIC 10BN SAMPLES WITH 0MIN (TOP LEFT), 30 (TOP RIGHT) AND 60 MINUTE (BOTTOM) SINTERING TIME. BOTTOM RIGHT IS VIEWED NORMAL TO PRESSING DIRECTION, THE REST PARALLEL. THE RED SQUARE IS THE AREA SCANNED IN EBSD. THE SCALE BAR IS 60 μM.......... 77

List of tables

TABLE 1. PROPERTIES OF MAJOR SIC POLYTYPES [13, 14].......... 4
TABLE 2. USES FOR H-BN POWDER. [32].......... 14
TABLE 3. SUMMARY OF SINTERING MECHANISMS IN A POLYCRYSTALLINE MATERIAL. [37].......... 20
TABLE 4. SIC AND SIC-BN POWDERS HOT-PRESSED IN THIS REPORT.......... 37
TABLE 5. COMPOSITION OF SIC 0BN POWDER.......... 38
TABLE 6. LIST OF EQUIPMENT USED IN THIS WORK.......... 38
TABLE 7. SAMPLE NAMING PATTERN RELATED TO HOT-PRESSING PROGRAM. X MEANS THE MENTIONED TEMPERATURE HAS NOT BEEN REACHED, WHILE 0 MEANS HOT-PRESSING WAS STOPPED UPON REACHING SAID TEMPERATURE. A HAS THE VALUE 0, 5 OR 10.......... 41
TABLE 8. DENSITIES OF SAMPLES HEAT-TREATED AT 1600°C WITH DIFFERENT HOLDING TIMES, MEASURED USING ARCHIMEDES' PRINCIPLE IN WATER.......... 70
TABLE 9. DENSITIES OF SAMPLES SINTERED WITH DIFFERENT HOLDING TIMES, MEASURED USING ARCHIMEDES' PRINCIPLE IN WATER.......... 70
TABLE 10. WT% TO AT% CONVERSION FOR SIC-5BN, USING VALUES FROM SI CHEMICAL DATA [85].......... 78
TABLE 11. WT% TO AT% CONVERSION FOR SIC-10BN, USING VALUES FROM SI CHEMICAL DATA [83].......... 78
TABLE 12. LATTICE PARAMETERS FOR SIC IN SIC 0BN, AS MEASURED BY RIETVELD FITTING IN *TOPAS*.......... 79
TABLE 13. LATTICE PARAMETERS FOR SIC IN SIC 5BN, AS MEASURED BY RIETVELD FITTING IN *TOPAS*.......... 79
TABLE 14. LATTICE PARAMETERS FOR SIC IN SIC 10BN, AS MEASURED BY RIETVELD FITTING IN *TOPAS*.......... 79
TABLE 15. D-SPACING FOR BN AND GRAPHITE PEAKS IN SIC 5BN, MEASURED MANUALLY IN *EVA*.......... 80
TABLE 16. D-SPACING FOR BN AND GRAPHITE PEAKS IN SIC 5BN, MEASURED MANUALLY IN *EVA*.......... 80

1 Introduction

1.1 Background

Silicon carbide (SiC) is a highly desired non-oxide ceramic in a wide range of technical applications. Excellent mechanical properties, high thermal stability and corrosion resistance, combined with low weight, makes SiC a high-performance material in abrasive, refractory, turbine and space technologies [1]. Dense silicon carbide parts are made by sintering sub-micron SiC with boron and carbon provided as either elemental substances or as compounds such as boron carbide (B_4C) or boron nitride (BN) [2].

Historically, boron carbide has been the cheapest way to provide boron in the sintering of SiC. Recent optimizations in the production of hexagonal boron nitride (h-BN) have lowered its price, and open up new possibilities for creating SiC-BN composites. These composites could take advantage of the lubricating properties, high temperature and chemical stability of h-BN, making a self-lubricating SiC ceramic suitable for operations where other lubricants (graphite, molybdenum disulfide, waxes and oils) simply will not survive.

Previous authors [2] have shown that small additions of h-BN (~2wt%) and carbon will sinter SiC to high densities, but additions above 7wt% deteriorate sintering [3]. This is caused by the low self-sinterability of BN, and external pressure is often used to sinter pure h-BN to high densities [4]. This has led to this work, where SiC-powders containing high amounts of h-BN have been sintered with external pressure (hot-pressed).

1.2 Aim

The aim of this work was to hot-press commercial silicon carbide powders with 5 and 10wt% added boron nitride to high densities. Time at maximum temperature was varied to investigate density, microstructural and compositional development. X-ray diffraction (XRD), electron backscatter diffraction (EBSD) and glow discharge optical emission spectroscopy (GDOES) techniques were used. The latter provides information on elemental composition, while the two former provide structural information. The results are presented and discussed along with recommendations for further studies and mechanical testing.

2 Theory

2.1 Silicon carbide

Silicon carbide is the most widely used non-oxide ceramic [5]. It is believed that the compound was first produced by Jöns Jacob Berzelius in 1824 [6]. Most known for his discovery of silicon, he speculated that one of his samples had a chemical bond between Si and C, yet this discovery claimed little attention at the time. It was not until Eugene and Alfred Cowles invented the electric smelting furnace in 1885 [7], and the adaptation by Edward Goodrich Acheson in 1892 [8], that silicon carbide was rediscovered. Acheson mixed coke and silica in an electric furnace, and discovered a crystalline material with great hardness and high temperature resistance. The material was found to consist of silicon and carbon, Acheson named the compound "carborundum", and gave it the correct formula SiC. There was an interest in silicon carbide as an abrasive and for cutting tools, and large scale production ensued.

Today, the process Acheson invented is still in use for large-scale production of technical silicon carbide, although the furnaces have been scaled up alongside leading technology. The product from the Acheson process is a porous, crystalline mass with long, integrated crystals roughly 0.1 centimeter in diameter. The Acheson process is described further in section 2.1.4.

Although SiC is opaque and colorless, different impurities result in different colors; Black from iron, green from nitrogen and aluminum result in blue, purple and black [9]. The crystalline mass is crushed for all applications, a demanding process with extreme equipment wear [10]. Silicon carbide has been discovered in nature; in a meteor from Cañon Diablo in Arizona. The meteor and the unknown compound in it were studied by Henri Moissan. He first believed the material was diamond, but in 1904 concluded it was silicon carbide [11]. The compound was named moissanite in his honor, and the name is still being used in mineralogy. Larger deposits have never been found.

2.1.1 Properties

The properties of silicon carbide quickly gained attention, as it could scratch ruby. This meant SiC claimed a 9 on Mohs hardness scale, between diamond (10) and topaz (8) [10]. The thermal stability of silicon carbide also gained interest, as it is impossible to melt at atmospheric pressure. At high temperatures, it will instead dissociate into graphite and silicon vapor, with the graphite remaining in the shape of the silicon carbide structure. Other thermal properties include high thermal conductivity and low thermal expansion. Silicon carbide has high specific strength, and is a semiconductor that can be doped to be insulating or conducting [12]. Table 1 show typical ranges for the two most common SiC structures, 3C and 6H, which will be discussed in the next section.

Table 1. Properties of major SiC polytypes [13, 14]

Property	3C	6H
Crystal structure	Zinc blende (cubic)	Hexagonal
Lattice constants [Å]	4.3596	3.0810; 15.118
Density [g/cm^3]	3.21	3.21
Band gap [eV]	2.36	3.05
Bulk modulus [GPa]	250	220
Thermal conductivity @ 300K [W/mK]	360	490
Thermal expansion [°C^{-1}]	3.8	4.3 (c-axis)

2.1.2 Structure

Silicon carbide crystallizes into a large number of different polymorphs called "polytypes". Polytypes was long believed to exist only in SiC, but polytypism has been shown to be rather common in crystals containing more than one chemical element [15]. One of the SiC polytypes is cubic and is called β-SiC, while the different hexagonal and rhombohedral variants are called α-SiC. The structure of SiC polytypes, and the transitions between them, have been thoroughly investigated by Jepps and Page [16, 17], and a brief recollection will be given here.

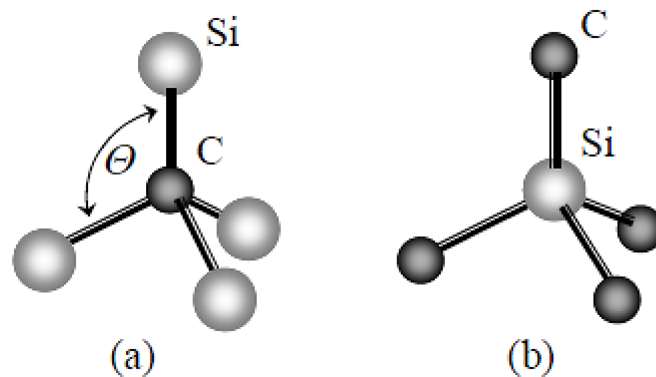

Figure 1. The basic tetrahedral unit of all silicon carbide polytype structures. [18]

All silicon carbide polytypes use the SiC_4 and CSi_4 tetrahedra as fundamental building blocks (Fig. 1), but different polytypes appear based on different stacking of tetrahedron layers. The stacking is analogue to the stacking of atom layers in a closely packed structure. Layers in ABCABC…-structure result in the cubic zinc blende structure (β-SiC), while ABAB… result in a hexagonal structure. There are, however, a few differences between stacking atoms and tetrahedra. Fig. 2 shows how the cubic ABC-packing gives tetrahedra pointing in the same direction, but hexagonal structures need a rotation as well in order to "get back" to an A position from the C layer. This rotation is denoted by an apostrophe, and the smallest hexagonal structure (bottom in Fig. 2) will then be denoted AC'AC'… Two other illustrations of SiC polymorph structures are shown in Fig. 3.

Ramsdell notation uses a letter for the type of structure (C for cubic, H for hexagonal and R for rhombohedral) and a number representing the smallest amount of layers in the repeating unit. The cubic packing ABC becomes 3C (β-SiC), while AC' becomes 2H, ABA'C' becomes 4H, and ABCB'A'C' becomes 6H, which are the most common hexagonal polytypes and called α-SiC. 6H can also be regarded as a cubic structure with twinning. A large number of SiC polytypes are mixes of these polytypes, having numerous layers before repetition; these have an overall hexagonal structure.

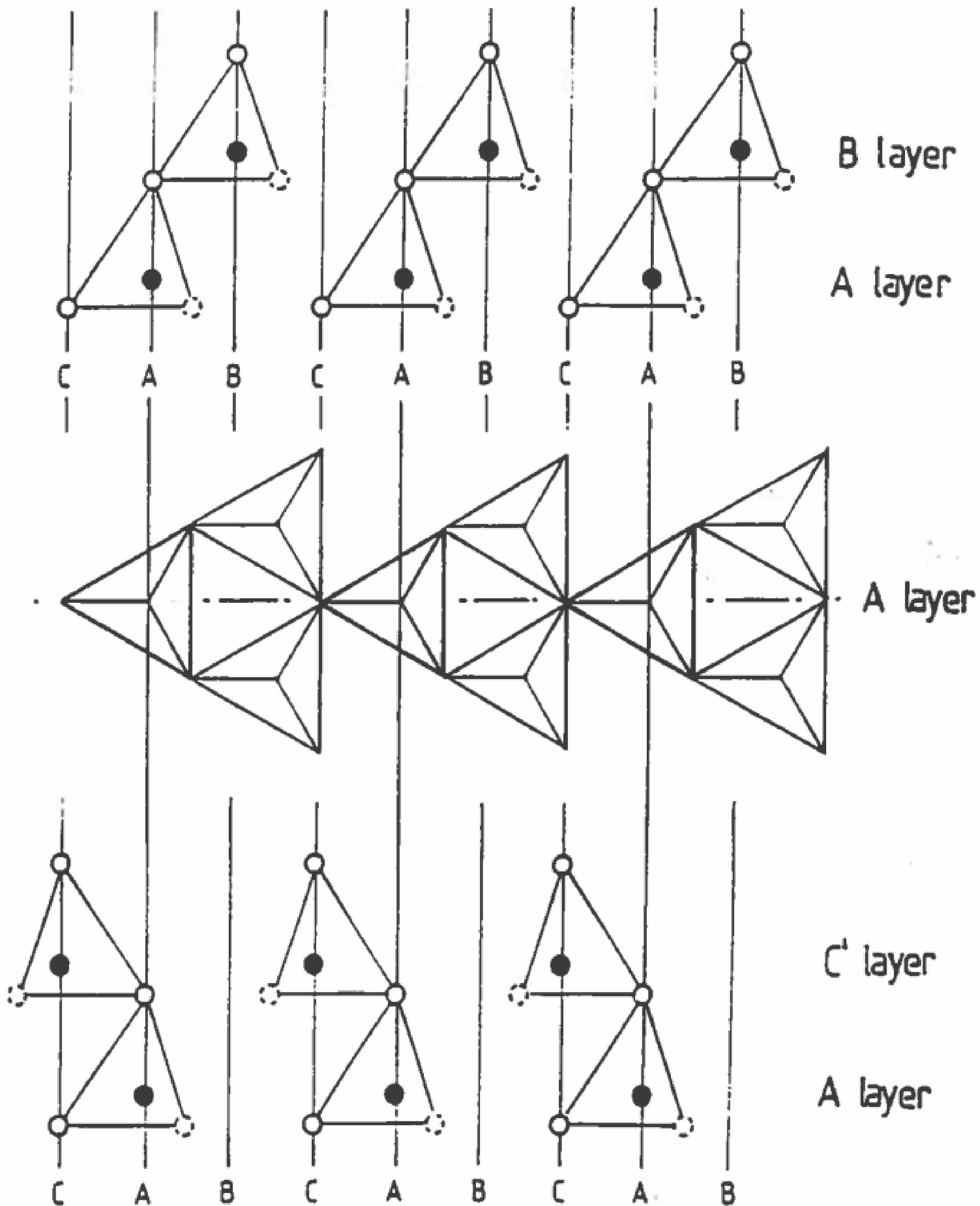

Figure 2. Stacking of tetrahedra in the SiC structures.
Top: Stacking without rotation, may be taken as the two first layers in the cubic stacking ABC…
Middle: The A layer seen from above, showing that every second layer is out of the plane of the paper.
Bottom: Stacking with rotation, may be taken as the repeating AC' unit of the smallest hexagonal structure, 2H. [10] (adapted from [16])

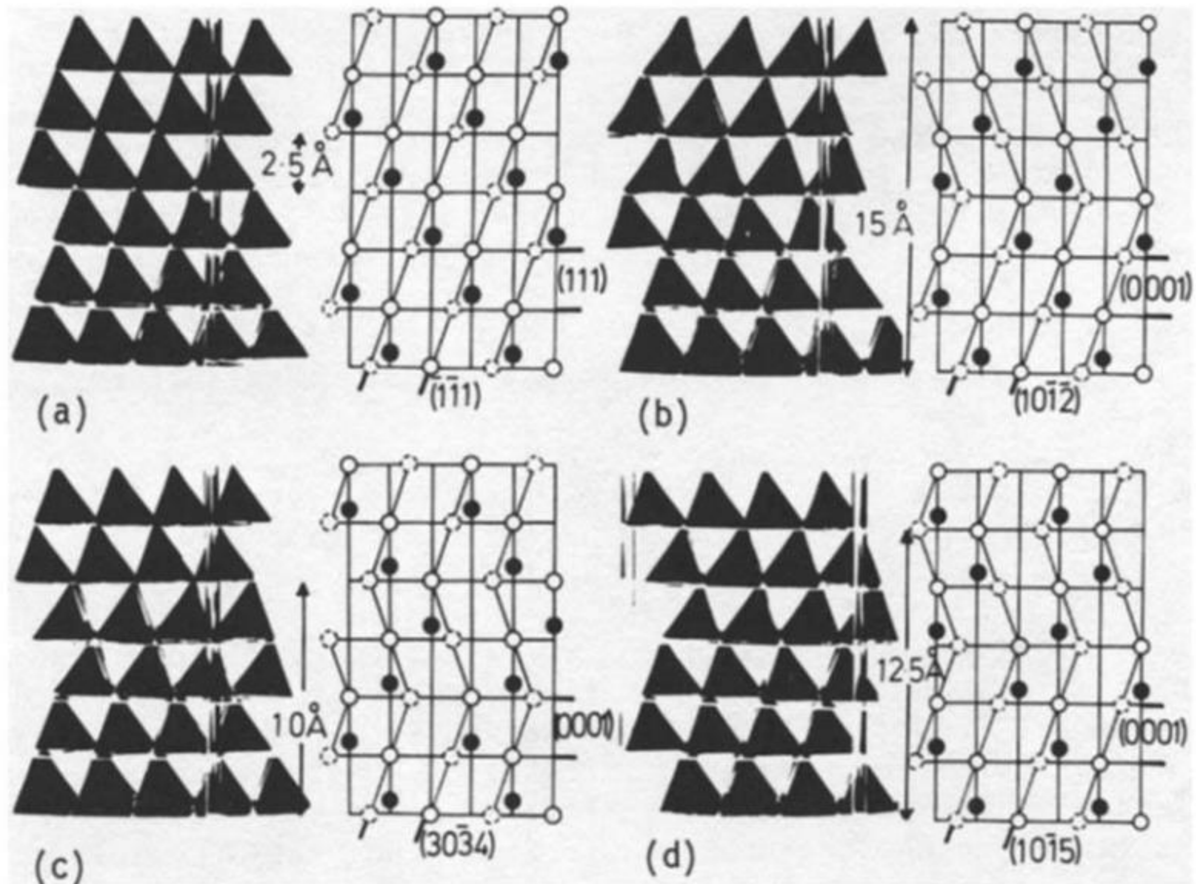

Figure 3. **Solid tetrahedra models for the four most common SiC polytype structures, together with “tramline” structure diagrams. ‘ABC’ and Ramsdell notation shown below [16].**

(a)	**3C**	**ABCABC**
(b)	**6H**	**ABCB’A’C’**
(c)	**4H**	**ABA’C’**
(d)	**15R**	**ABCB’A’BCAC’B’CABA’C’**

2.1.3 Thermodynamic stability and polytype transition

From the general observation that β-SiC is formed at lower temperatures, and transitions to α-SiC at high temperatures, it is easy to believe that they are low and high temperature configurations, respectively. ß-SiC has since been produced at high temperatures, causing the JANAF thermochemical data of 1985 [19] to list ß-SiC as the most stable configuration at all temperatures (albeit with only 2 kJ difference at 2000 °K). Knippenberg [20] had the opposite conclusion in 1963, as the transformation from ß-SiC to α-SiC was determined to be irreversible.

Knippenberg [20] suggested that the growth of different polytypes in SiC was not reliant on temperature, but instead of growth conditions. The growth of ß-SiC is preferred if there is extra Si present, as this gives rapid crystal growth at relatively low temperatures [21]. Impurities can also affect polytype growth, since electron donors like nitrogen increase the growth rate of ß-SiC. Jepps and Page [22] demonstrated a transformation from 6H to 3C by heating silicon carbide in nitrogen pressures ranging between 10 and 30 bar.

Heine, Cheng and Needs [23] have used quantum mechanics calculations to explain the early formation of the 3C-polytype in silicon carbide production. To form a 4H or 6H-structure, every third or fourth layer of tetrahedra must be rotated, as explained in the previous section. The calculations show that although the hexagonal structures have the lowest free energy, addition of 3C-layers require less energy if the tetrahedra are originally parallel to the structure. The formation of ß-SiC is therefore due to a lower barrier of formation; an example of Ostwalds “step-rule” (Stufenregel), which argues that the first phase to form is not necessarily the most stable, but the phase closest in free energy to the original phase [24]. This causes formation of 3C-structure, unless the temperature is high enough, or the growth rate low enough, to allow formation of equilibrium structure.

Kistler-De Coppi and Richarz [25] studied the effect of boron and nitrogen on phase transformations in SiC. Without these additions β-SiC would start to transform into α-SiC at 2000°C and form large hexagonal platelets. After 1 hour at 2150 °C in argon atmosphere, the α-SiC usually comprised of 90% 6H and >10% 4H and 15R. Annealing these samples at 2150 °C with 2 wt% boron addition transformed 6H into 4H, see Fig. 4. Switching to nitrogen atmosphere slowed the transition.

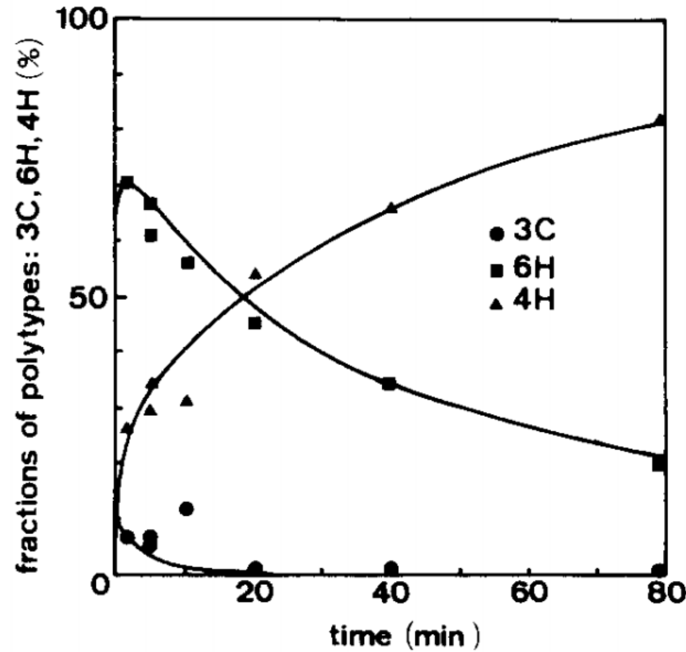

Figure 4. **Amount of polytypes after annealing of 90% 6H α-SiC doped with 2wt% boron (argon atmosphere, 2150°C). [25]**

Grain growth started above 1900°C for the pure samples, but impurities could shift these temperatures. The grain growth required a certain vapor pressure to occur, which indicates the gas phase is involved in the grain growth mechanisms. Switching from argon to nitrogen atmosphere did not slow down grain growth, only polytype transition.

2.1.4 Production of silicon carbide by the Acheson process

The first commercial producer of silicon carbide, The Carborundum Company, was founded by E. G. Acheson in 1891. The furnace design is still the most common silicon carbide production technique, although the design has been scaled up [26, 27]. Sketches of an industrial furnace for the Acheson process is shown before a run in Fig.5, and after in Fig. 6. The main construction is similar to a bed, usually between 3 and 4 meters wide and 10 to 25 meters long. U-shaped beds are also in use, and height depends on the refractory walls used. The charge usually consists of petroleum coke and silica, and sometimes sawdust for increased porosity and salts for removal of impurities [10]. Porosity is important for avoiding local pressure increases, leading to “blow-outs”.

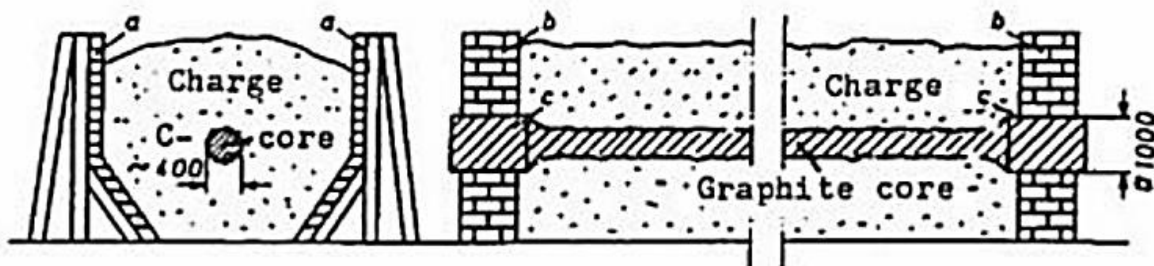

Figure 5. **Schematic of cross and longitudinal sections of a furnace running the Acheson process. (a) are removable side walls made out of refractory bricks, (b) are refractory end walls and (c) are electrodes. [10]**

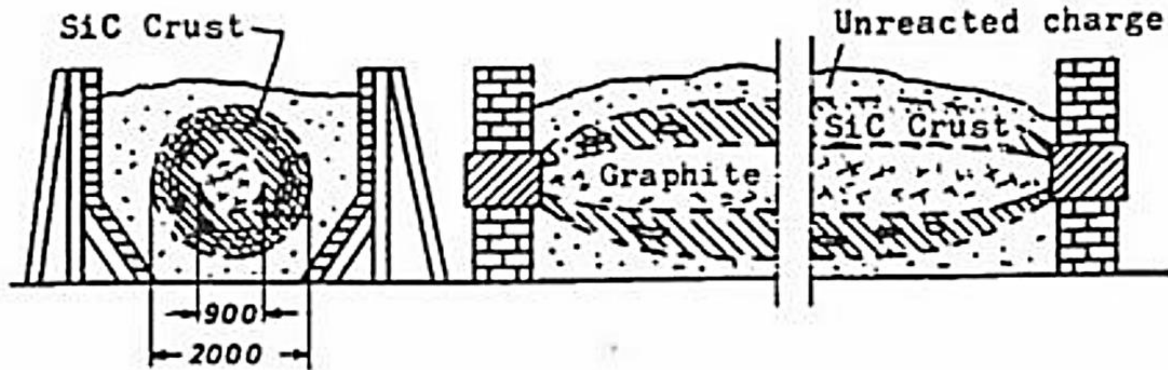

Figure 6. **Sections of the furnace after the Acheson process run. Approximate cross section diameters in mm. [10]**

The furnace bed is filled with a well-mixed charge, and a solid graphite electrode carries current from end to end, through the center of the furnace. The furnace is filled with charge up to a height roughly equal to its width [10]. The oven is then heated by resistive heating of the graphite electrode, typically between 2 and 5 MW. This power is usually applied for 24 to 48 hours, although at a decreasing rate, as the increased core temperature results in higher conductivity in the graphite, and possibly some silicon carbide conduction [10]. The furnace is then left to cool for a couple of days, before the bed is emptied. Although the process is conducted in air, oxygen does not influence the production of silicon carbide [10].

The outmost layer of used charge will be un- and partially reacted, which can be used in a new charge. Re-used charge will affect the final product, and the industry often uses separate furnaces for new charges, called “green furnaces”, and mixed charges, called “black furnaces”. Beneath the unreacted charge are fine and impure carbides, then a cylindrical layer of coarse α-SiC. The core temperature can reach sublimation temperatures for silicon carbide (~2500-2700°C, [20]), leaving graphite residue behind.

Chemistry of the Acheson furnace

The chemistry of the Acheson process can be described by the overall equation

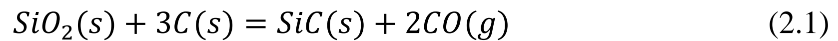

$$SiO_2(s) + 3C(s) = SiC(s) + 2CO(g) \tag{2.1}$$

This reaction has several intermediate steps, where most authors [11] agree on two reaction steps

$$SiO_2(s) + C(s) = SiO(g) + CO(g) \tag{2.2}$$

and

$$SiO(g) + 2C(s) = SiC(s) + CO(g) \tag{2.3}$$

where the sum of reaction (2.2) and (2.3) equal (2.1). This represents a system with three solid phases and one gas phase. Gibbs phase rule then yields one defined equilibrium point at a given temperature. Thermodynamical data [19] then gives 1 bar equilibrium pressure at 1510°C, with a gas phase containing 99% CO and 1% SiO gas. Thermodynamically, it should therefore be possible to produce silicon carbide at 1510°C.

With kinetics, the picture changes. Reaction (2.2) is written as a solid state reaction, but may not be a likely assumption. Miller, Lee and Cutler [28] have suggested a CO/CO_2-mechanism

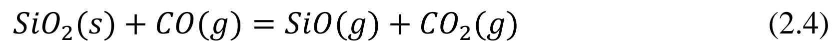

$$SiO_2(s) + CO(g) = SiO(g) + CO_2(g) \tag{2.4}$$

followed by reaction (2.3) and the Boudouard reaction

$$CO_2(g) + C(s) = 2CO(g) \tag{2.5}$$

The mechanism is the same as reduction of iron oxide, except the monoxide in reaction (2.4) is a gas. The partial pressure of CO_2 at equilibrium and P_{CO} = 1 bar can therefore not be determined at a given temperature, without an additional constraint. In Fig. 7, the authors have suggested the limitation $P_{CO2} = P_{SiO}$, given by stoichiometry in reaction (2.4). From the figure, this constraint gives a P_{SiO} too low for the production of SiC below 1900°C. However, the CO_2 partial pressure will be reduced by reaction (2.5), which means P_{SiO} will be somewhat higher than (2.4) alone would suggest. It is therefore difficult to define a definite temperature for the formation of SiC, yet it must be higher than 1510°C at 1 bar CO. The reaction rates are influenced by the diffusion of SiO and CO_2 in the charge. The mechanisms outlined here have been compared to elaborate experimental work of silica-carbon reactions in atmospheres with varying P_{CO} [29, 30].

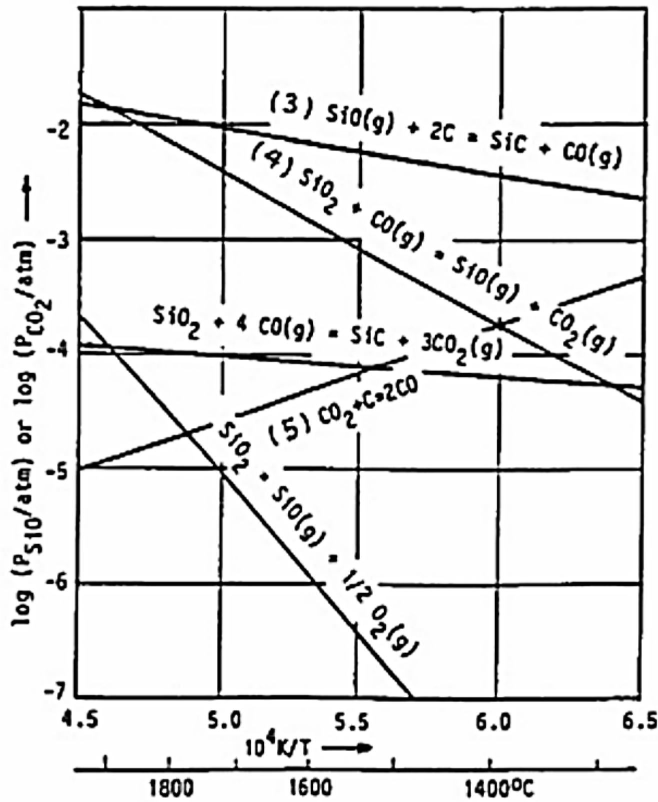

Figure 7. **Equilibrium pressures of SiO and/or CO_2 for reactions between carbon and silica. Pressures for reaction (3), (4) and (5) are calculated for P_{CO} = 1bar, and (4) with $P_{SiO} = P_{CO2}$. Thermal dissociation of silica for comparison, with the assumption $P_{O2} = ½ P_{SiO}$. [10]**

According to the outlined mechanism, silicon carbide should form onto carbon particles in the furnace. This exact phenomenon has been observed in several instances. Tone [31] refers to an interesting example in the early days of the industry: A pine board ended up in a furnace by a mistake, and after the run, the entire board had been converted into SiC; parts of it an exact copy of the tree structure. Motzfeldt [10] report similar results with charcoal in the charge.

2.2 Hexagonal boron nitride

Hexagonal boron nitride is often called “white graphite” due to its hexagonal, layered structure, see Fig. 8. Within each layer, boron and nitrogen are bound by strong, covalent bonds, while the layers are only held together by weak van der Waals forces. Graphite and h-BN have the same “plate-like” structure as molybdenum disulfide (“moly”), where layers easily glide over each other. This causes a solid lubrication effect, much similar to a deck of cards spread out on a table. Unlike graphite, h-BN does not require water or trapped gas molecules to achieve this lubrication effect, and can therefore be used in vacuum (for space applications) and high-temperature applications [32].

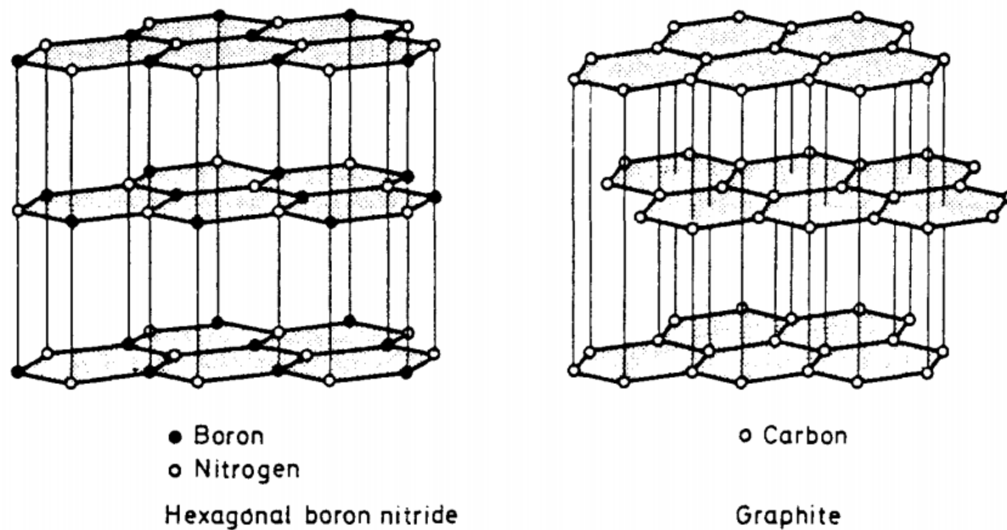

Figure 8. Crystal structure of hexagonal boron nitride (h-BN) compared to graphite. [32]

Hexagonal boron nitride has not been observed in nature, but was synthesized by Balmain in the 1840s [33]. Today, three different production routes have found practical application on an industrial scale:

1. Reacting boric oxide with ammonia

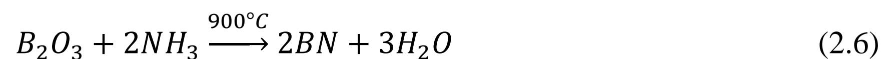

$$B_2O_3 + 2NH_3 \xrightarrow{900°C} 2BN + 3H_2O \tag{2.6}$$

2. Reaction of boric oxide with organic nitrogen compounds (i.e. urea)

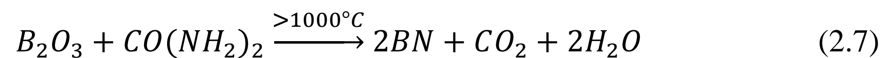

$$B_2O_3 + CO(NH_2)_2 \xrightarrow{>1000°C} 2BN + CO_2 + 2H_2O \tag{2.7}$$

3. Nitridation of calcium hexaboride in the presence of boric oxide

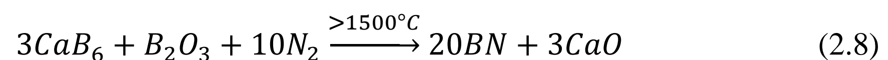

$$3CaB_6 + B_2O_3 + 10N_2 \xrightarrow{>1500°C} 20BN + 3CaO \tag{2.8}$$

Equation (2.6) and (2.8) usually produce crystalline h-BN platelets about 0.1-0.5µm thick and 1-10µm wide, while (2.7) can result in “turbostratic” boron nitride, which has completely disordered structure in the z-direction.

The most interesting properties of boron nitride include low density (2.27 g/cm^3), high temperature stability (1000°C in air, 2200°C in argon, 2400°C in N_2 and theoretical melting point near 2600°C), chemical inertness, electric insulating and very high thermal conductivity. Its lubricating properties are retained until 900°C [32]. BN also has non-wetting properties, making it relatively resistant to molten glass, silicon and boron, as well as reactive metal melts. The low self-sinterability of BN means dense shapes are obtained almost exclusively by hot-pressing. A wide range of applications for h-BN powder and are listed in Table 2, while literature on BN in sintering of SiC will be presented in 2.4.3, and Si-(B-)C-N ceramics in 2.5.

Table 2. Uses for h-BN powder. [32]

Use	Property desired				
	R	*T*	*E*	*I*	*L*
Solid lubricant for high-temperature bearing	+				+
Mould release for die casting of glass and metals	+			+	+
Active filler for rubber, resin and plastics	+	+	+	+	+
Additive to oils and high-temperature grease				+	+
Ultrahigh-pressure transmitting agent	+			+	+
Coatings for evaporation plants, as parting agent for deposited metal films	+			+	
Coating for graphite hot-pressing moulds	+			+	+
Embedding medium for heating wires	+		+	+	
Boron source for preparation of other boron compounds	+				

R, high-temperature refractoriness; T, thermal conductivity; E, electrical insulator; I, chemical inertness and non-wetting; L, lubricity.

2.3 Theory of sintering

When comparing a ceramic green body to its sintered equivalent, two things become apparent: The sintered body has a higher strength, and takes up a smaller volume. These are macroscopic differences, yet have to be explained at particle level. Or, to be more specific, at the inter-particle level.

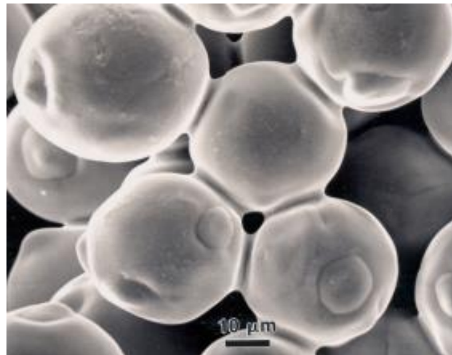

Figure 9. Scanning electron micrograph of neck growth between 32 µm nickel spheres during sintering at 1050ºC for 30 min in vacuum. Prior to sintering the particles were loosely packed into a crucible.[34]

Figure 9 shows a scanning electron microscopy (SEM) image of sintered nickel spheres. The formation of "necks" around the area of inter-particle contact is the reason sintered bodies have higher strength than green body equivalents; most materials have higher strength than organic binders in their respective green bodies. Mass is transported from the existing particles toward the necks, which result in denser packing, volume reduction and pore removal. Formation of these necks is due to global and local driving forces, which will be described in the following sections.

2.3.1 Global driving forces for sintering

Sintering is a result of the system trying to lower its free energy. Therefore, any reason for reducing the free energy is considered a driving force for sintering. The three most commonly recognized global driving forces are: Reducing surface free energy, relieving externally applied pressure and chemical reactions [35]. Chemical reaction is rarely used, as a reaction makes the microstructure very difficult to control. Chemical reaction is therefore not outlined here.

Surface free energy

All irreversible processes are accompanied by a reduction in free energy, and a reduction in surface free energy can be achieved in two ways for solids: Reduction of total surface area or transformation of solid/vapor interfaces to solid/solid interfaces (since solid/solid interfaces generally have lower free energies). The first process is called coarsening, where large particles and pores grow at the expense of small ones. This leads to a reduction in total surface area, but will not increase the density, as pores also grow.

The second process transport material from grain boundaries toward particle interfaces. This leads to growth of necks, as shown in Figure 10. This reduces the total amount of solid/pore interfaces, reducing the surface free energy. As matter is transported toward the necks, average particle distance decreases, and the reduction in volume increases the density. The local driving force for sintering is detailed in 2.3.2.

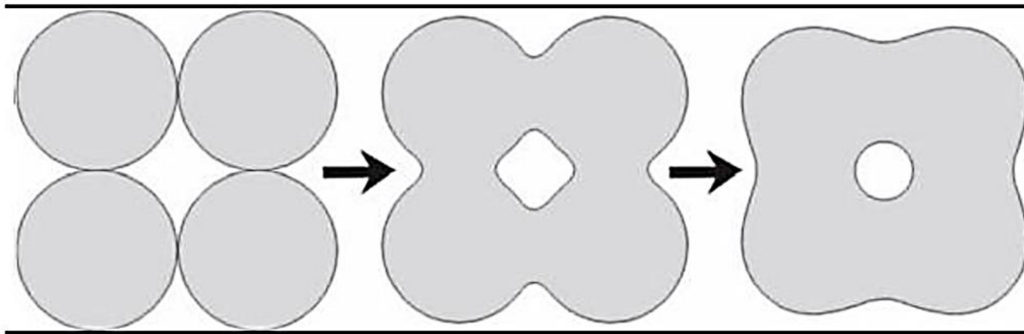

Figure 10. Schematic of particle changes during sintering. Shrinkage is noticeable. [36]

Process one and two are in competition, and sintering additives and temperature program should be carefully designed to maximize sintering mechanisms at the expense of coarsening. A high heating rate and additives that reduce grain boundary diffusion at lower temperatures are often used. The transport mechanisms for coarsening and sintering are different, and are examined in section 2.3.3.

Externally applied pressure

Externally applied pressure increases the driving force for a system to lower its free energy [35, 37]. In addition, the force can introduce two new mechanisms: Particle rearrangement and grain boundary sliding. The former is also found in pressureless sintering, of course, as powders are often pressed into green bodies before this type of sintering. However, with particle rearrangement happening *in situ* at high temperatures, hot-pressing allows better molding and better final packaging [35]. Additionally, the uniaxial pressure forces grain boundaries to slide against each other to relieve pressure. The fixed diameter of the die ensures most of this densification happens in the same direction as the applied load, see Fig. 11. This causes grains to flatten in the direction of the applied pressure, and when matter transport occurs by diffusion, grain boundary sliding is necessary to accommodate this change in grain shape.

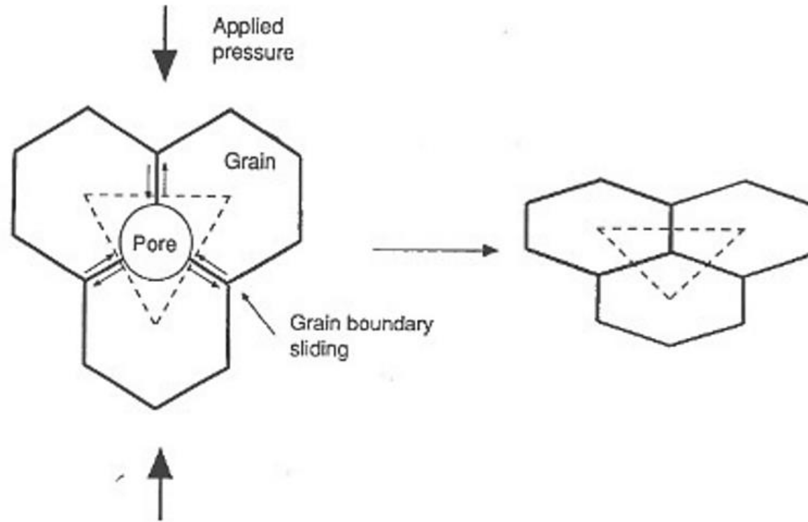

Figure 11. **Sketch illustrating the change in grain shape that occurs during hot-pressing. Grains are flattened in the direction of the applied pressure. If matter transport occurs by diffusion, grain boundary sliding is necessary to accommodate the change in grain shape. [37]**

Relative sizes of surface free energy and externally applied pressure in silicon carbide

To investigate the relative sizes of the previously detailed forces for sintering, equations from Rahaman *et al.* [35] will be presented with literature data for SiC [38, 39]. Consider one mole of spherical particles with radius a. The number of particles, N, is given by (2.9), where ρ is the density of the particles, assumed to contain no internal porosity, M is the molecular weight and V_m is the molar volume.

$$N = \frac{3M}{4\pi a^3 \rho} = \frac{3V_m}{4\pi a^3} \tag{2.9}$$

The total surface area of the particles is then given by

$$S_A = 4\pi a^2 N = \frac{3V_m}{a} \tag{2.10}$$

If we combine these equations with γ_{sv}, the surface energy per unit area for the particles, the surface free energy E_S for the particles is:

$$E_S = \frac{3\gamma_{SV} V_m}{a} \tag{2.11}$$

In (2.11), E_S represents the decrease in surface free energy upon the formation of a fully dense body. Inserting V_{mSiC} = 12.45 cm^3/mol [39], γ_{SVSiC} = 2.5 J/m^2 [38] and a = 1.0 µm into (2.11) yields E_S = 93 J/mol. This is the free energy motivation for sintering, and occurs regardless of external pressure. Note also the exponential increase in E_S as a approaches 0, as sketched in Fig. 12. This shows how free energy driving force increases drastically with finer powders.

This has led to an increasing interest in nano-structured SiC for structural applications. The particle size for such use should be 20-150 nm [40].

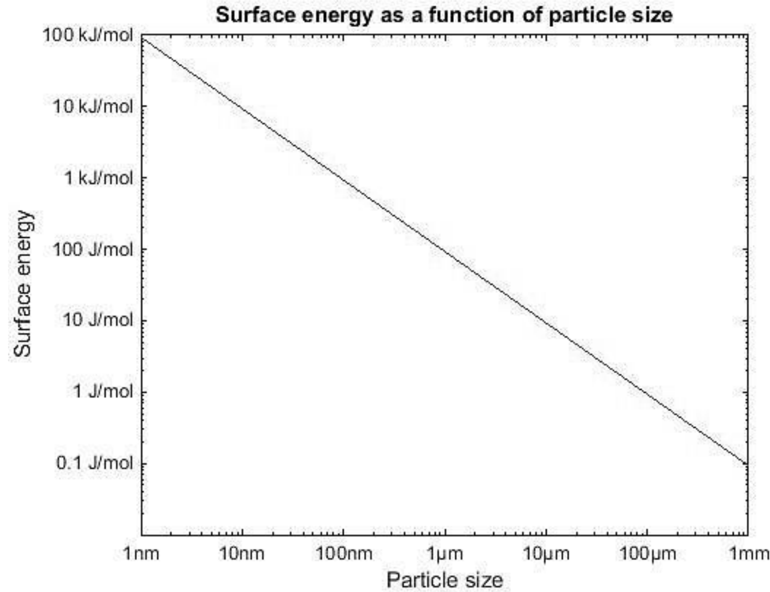

Figure 12. Change in surface energy E_S as a function of average particle size *a*.

Consider now the work done on a system of 1 mole of particles with a pressure P_a. The work performed on the particles can be approximated by

$$W = P_a V_m \tag{2.12}$$

For p_a = 20 MPa, a typical value for external pressure applied in sintering and the pressure used in this work, W becomes 249 J. The external driving force is therefore larger than the free energy driving force (roughly 2.7 times), but the difference is smaller than "typical values" reported by Rahaman et.al [35] (10 times). Still, external pressure is known to massively increase densification in SiC [2, 41]. This would indicate the kinetic effect of external pressure plays a large role in the sintering of SiC, which is reasonable given the high directionality and strength of Si-C bonds [42].

2.3.2 Local driving force for sintering

In subchapter 2.3.1, reduction of surface free energy, the relieving of external pressure and chemical reactions were presented as global driving forces for sintering. On an atomic scale, the reduction of free energy occurs due to chemical potential differences between curved and flat surfaces [37]. This potential difference is described by the Gibbs-Thompson equation

$$\Delta\mu = \mu_{curv} - \mu_{flat} = \gamma_{SV}\Omega_{MX}\kappa \tag{2.13}$$

μ is chemical potential, γ_{SV} is the solid/vapor surface energy, Ω_{MX} is the volume of one unit formula for compound MX, and curvature κ is dependent on the particle geometry, with

negative notation for a concave surface and vice versa. At equilibrium conditions, this translates into a difference in partial pressure P:

$$\Delta\mu = kTln\frac{P_{curv}}{P_{flat}} \tag{2.14}$$

These equations combined with the assumption $P_{curv} \approx P_{flat}$ for spherical particles become:

$$P_{curv} = P_{flat}\left(1 + \frac{2\Omega_{MX}\gamma_{SV}}{\rho kT}\right) \tag{2.15}$$

These equations predict higher partial pressure above a convex surface than above a flat surface, while it is lower above a concave surface. This pressure difference between convex and concave surfaces, coupled with the chemical potential difference, mean vacancies are easier to form below concave surfaces. A higher vacancy concentration will then lead to a vacancy flux, schematically illustrated in Fig. 13.

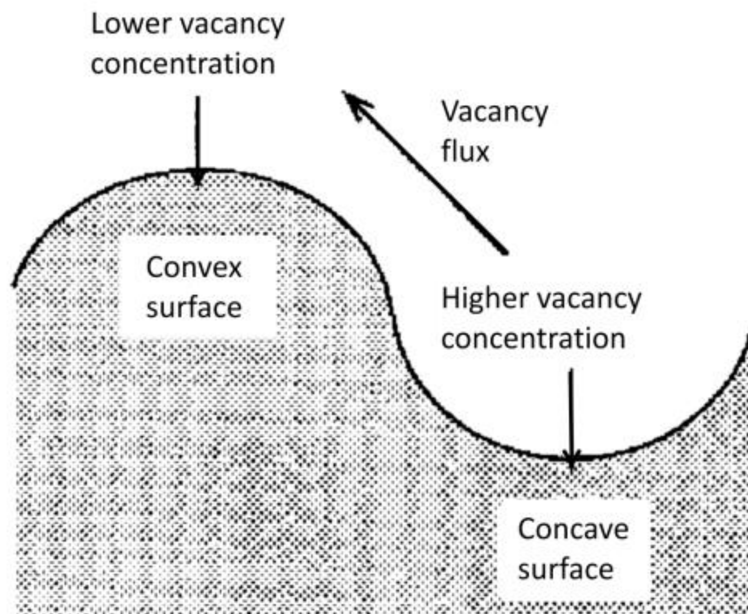

Figure 13. Schematic of vacancy flux on a curved surface. [44]

2.3.3 Mass transport mechanisms

A vacancy flux necessarily means matter has to be transported the opposite way. There are six mechanisms of matter transport that are relevant for sintering, shown in Fig. 14 and Table 3. Surface diffusion, lattice diffusion from surface and vapor transport, labeled 1, 2 and 3 in the figure, are the non-densifying mechanisms which lead to coarsening and grain growth. Grain boundary diffusion and lattice diffusion from the grain boundaries, labeled 4 and 5, are sintering mechanisms which lead to densification. Plastic flow is not a major contributor in the sintering of ceramic materials, but is more common in metals and amorphous materials.

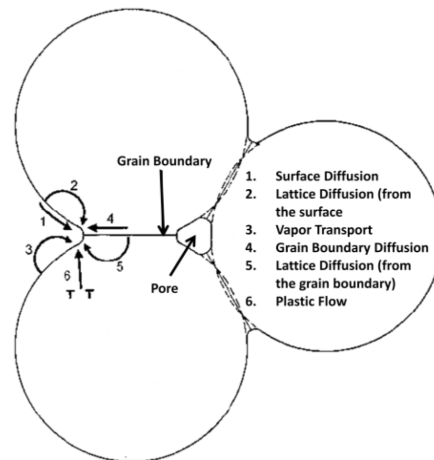

Figure 14. Schematic of mechanisms that contribute to material transport in sintering of a polycrystalline powder. [44]

Table 3. Summary of sintering mechanisms in a polycrystalline material. [37]

Mechanism	Source of matter	Sink of matter	Densifying	Non-densifying
Surface diffusion	Surface	Neck		X
Lattice diffusion	Surface	Neck		X
Vapor transport	Surface	Neck		X
Grain boundary diffusion	Grain boundary	Neck	X	
Lattice diffusion	Grain boundary	Neck	X	
Plastic flow	Dislocations	Neck	X	

2.3.4 Sintering stages

Sintering is often understood as process in three successive stages: An initial stage with particle rearrangement and neck formation at contact points, an intermediate stage with neck growth, and a final stage with pore closure and grain growth. Coble *et al.* [43] was the first to describe sintering in this three-step way, and is still used today. The sintering stages described here only apply to polycrystalline materials, as amorphous materials undergo different stages. Figure 15 illustrates the different stages, as drawn by Barsoum [44].

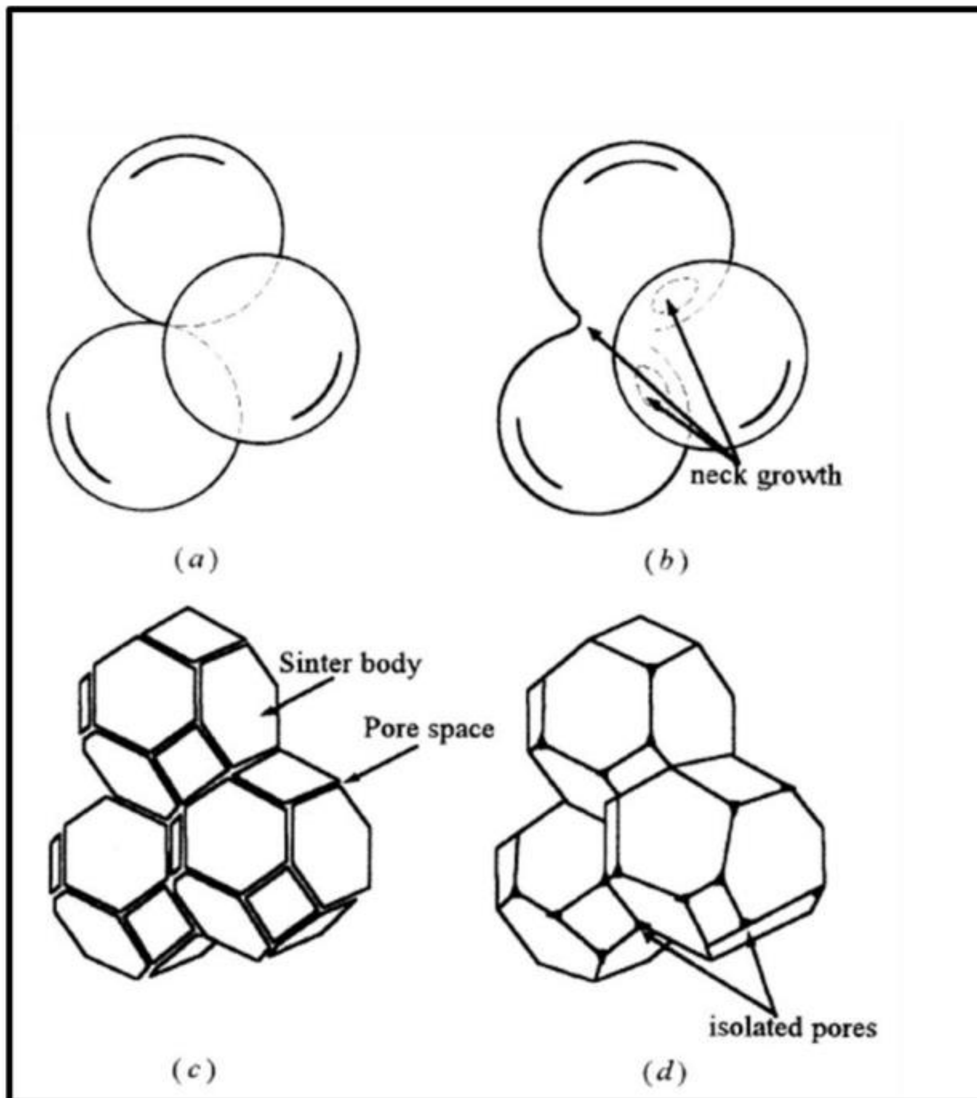

Figure 15. **Schematic of sintering stages during sintering of spherical particles (a) in contact at the onset of sintering, (b) near the end of the initial sintering stage, as noted by neck formation, (c) intermediate stage with neck growth and (d) final stage of sintering. Note how particles are closer to tetradekaidecahedral in shape in (c) and (d). There is continuous porosity along edges in (c), and closed pores at each corner in (d). [44]**

The first stage of sintering spherical particles starts with particle contact and ends when necks have been formed and start to grow. The density in the initial stage is typically 60-65 percent of theoretical maximum, with continuous porosity through the sample. The change from (a) to (b) in the figure above represents the first stage.

The intermediate sintering stage begins with uniform neck growth, and ends when continuous porosity ends. This stage of sintering often brings the density from ~65% to ~90%. When sintering nears the final stage, particles have shapes closer to tetradekaidecahedrons in shape, assuming spherical starting particles. There are continuous pore channels along edges, which will close off when the intermediate stage ends. The maximum neck size that can be achieved in the intermediate stage of sintering is determined by the dihedral angle from

$$\gamma_{GB} = 2\gamma_{SV} \cos\frac{\theta}{2} \tag{2.16}$$

where γ_{GB} is the grain boundary free energy, γ_{SV} is the solid/vapor interface free energy and θ is the dihedral angle shown in Fig. 16. It is seen from (2.16) that γ_{GB} must be less than half of γ_{SV} for the dihedral angle to be less than 180°.

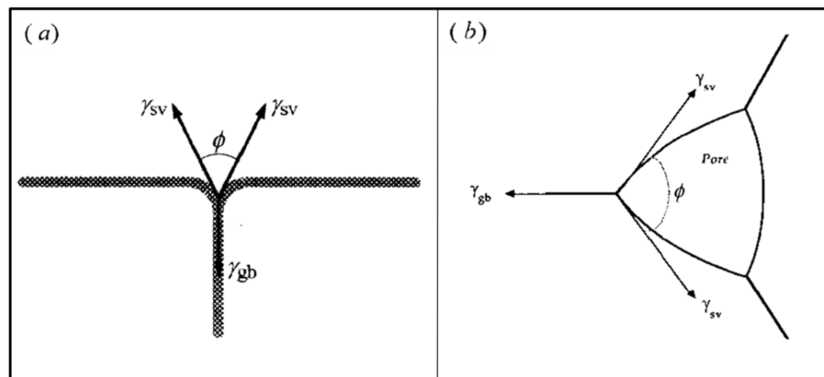

Figure 16. Equilibrium dihedral angle (a) between two grains and (b) inside a pore. [37]

At the final stage of sintering, the porosity channels along tetradekaidecahedral edges are closed off, and only closed pores remain. The pores are now only located at tetradekaidecahedrons corners and inside grains. The pores are lenticular at the corners and round if they are inside a grain. Density is now >90% of theoretical. Further densification is possible through grain growth if the intermediate stage gave good enough densification; cf. (2.16) above.

2.4 Sintering silicon carbide

The strong, covalent bonds that provide the great properties of silicon carbide, also make SiC notoriously hard to consolidate into dense bodies [1]. The self-diffusion coefficients in silicon carbide are extremely low [45] and the surface free energy difference between solid/vapor and solid/solid is miniscule [46]. Surface free energy is therefore a weak driving force for sintering silicon carbide, cf. section 2.3.1 and 2.3.4.

With external pressure, Nadeau [41] was one of the first to sinter pure SiC to high densities in 1973, hot-pressing at 2500°C with 50 MPa. Prochazka and Scanlan [2] were the first to report high density SiC with pressureless sintering in 1975, using small additions of boron and carbon as additives. Boron and carbon, as elements or compounds like B_4C, are now widely used in pressureless sintering of SiC to achieve densities above 95% [47].

Prochazka and Scanlan [2] suggested the amorphous boron separated mismatched grains, increasing grain boundary free energy, while carbon removed silica and free silicon on SiC surfaces, lowering the surface free energy. Combined, the effect was believed to increase the free energy driving force enough to achieve high densities, cf. 2.3.4. Greskovich and Rosolowski [48] later studied neck size in sintered silicon carbide with and without boron and carbide, and found little variation between specimens. This disagreed with Prochazka and Scanlan's proposal, as a higher free energy driving force should result in larger necks, as according to Eq. (2.16). Instead, boron appeared to reduce coarsening during heating, maintaining short diffusion distances until the onset of sintering.

Lange and Gupta [49] observed small pockets of boron-rich phases in SiC sintered with boron and carbon. This led them to conclude that sintering occurred by liquid-phase sintering, creating strong capillary forces to densify the silicon carbide. High-resolution transmission electron microscopy has consistently failed to show a continuous secondary phase in SiC grain boundaries [50, 51], and the possibility of liquid-phase sintering was later discounted by Ogbuji [51]. The most recent explanation for boron and carbon as sintering aids in silicon carbide will be presented in the following sections.

2.4.1 The effect of boron addition

Hamminger *et al.* [52] have concluded that most of the boron additions in sintered SiC can be found in solid solution in the silicon carbide structure. Silicon carbide sintered with B and C additions tend to exhibit clean grain boundaries, with carbon-rich inclusions also containing boron compounds with excessive additions. Tajima and Kingery [53] found that boron can substitute both silicon and carbon atoms in the lattice. The C site is favored when strain energy is considered, as there is a smaller difference in covalent radii ($r_{cov(B)}$=0.088 nm, $r_{cov(C)}$=0.077 nm and $r_{cov(Si)}$=0.107 nm [53]). The Si site is favored when stability of bonding is considered, as the binary compound B_4C is much more stable than SiB_4. The result is that B substitute both Si and C in the SiC matrix, and lattice parameter changes (as measured by X-ray diffraction) are much smaller than can be expected if B substituted only one, as illustrated in Fig. 17.

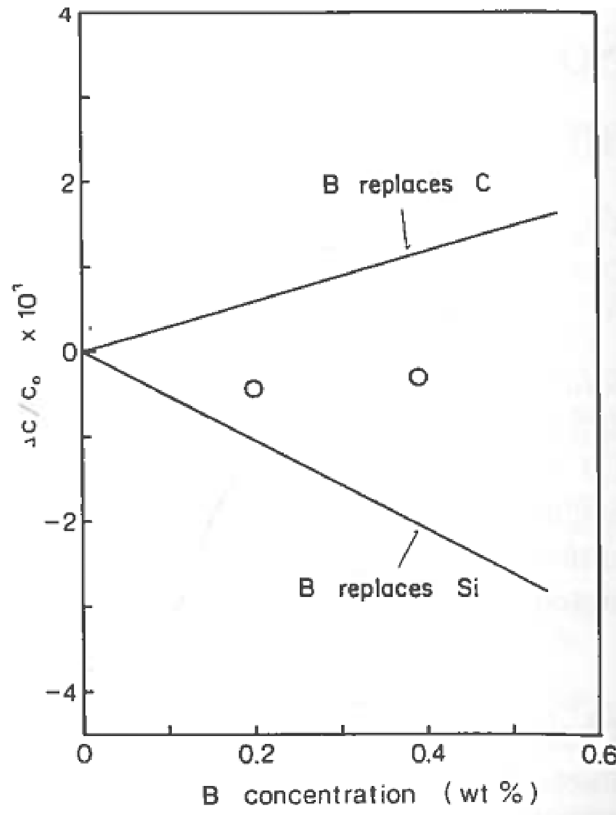

Figure 17. **Fractional change in lattice parameter *c* of 6H-SiC as a function of B concentration. Open circles are experimental values, while solid lines show calculated values if boron replaced only Si or C lattice points. [53]**

To investigate how boron affects the sintering of SiC, Murata and Smoak [54] measured sintered densities of SiC as a function of carbon additions at a constant boron amount, and vice versa. Their findings are sketched in Figure 18:

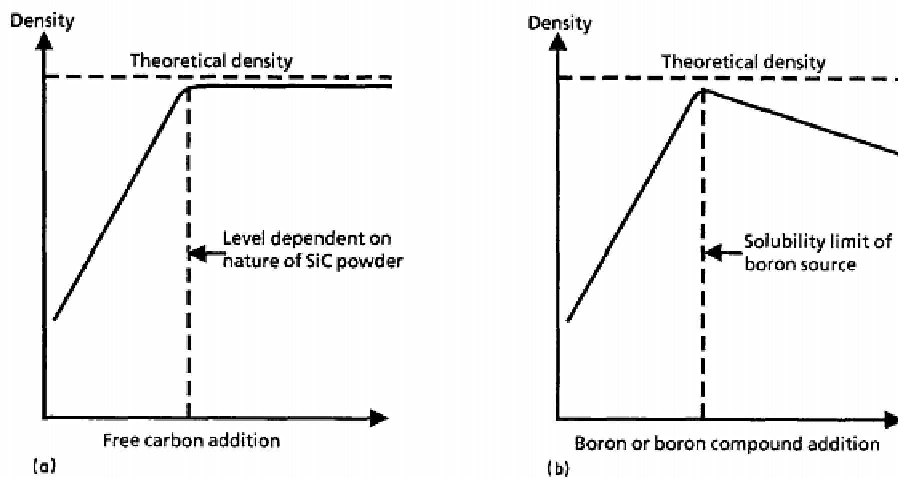

Figure 18. **Schematic representation of sintered density of silicon carbide with changes in (a) carbon and (b) boron additions. There was a constant boron additions (a), and constant carbon additions (b). [47] (adapted from [54])**

At constant boron content, increasing amounts of carbon increased sintered density until a threshold value. The threshold was reached between 2 and 4wt% carbon, depending on SiC

powder characteristics. There was little change in density beyond this point, but a reduction in grain size was observed. At a constant level of carbon, boron additions rapidly increased sintered density up to a point, and then the density slowly declined. The threshold coincided closely with the solubility of the boron source (BN, BP and B_4C) in SiC. Maddrell [47] suggested that boron entered and disrupted the rigid silicon carbide structure, enhancing solid state diffusion. The increased diffusion rates could be caused by an increase in total vacancy concentration, or more flexible binding orientations. Excess boron segregated to grain boundaries, and increased diffusion paths. Mizrah *et al.* [55] reproduced Murata and Smoak's [54] experiment, adding boron at constant carbon additions for SiC-powders, but with different particle sizes. The results are sketched in Fig.19:

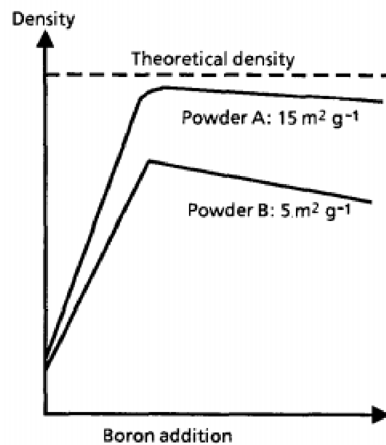

Figure 19. Schematic representation of sintered density variation with increasing boron additions for SiC powders with different particle sizes. [47] (adapted from [55])

The slower drop-off agrees with Maddrell's suggestion; smaller particles lead to more surface area and more grain boundaries to distribute excess boron, so the density drop-off is lower.

To summarize: Boron is believed to diffuse into and disrupt the SiC crystal structure at high temperatures, enhancing SiC self-diffusion. Boron also reduces the effect of coarsening during heating. Boron additions beyond the solubility limit of the particular boron source will segregate SiC-grains, which increase diffusion paths and lower sintered densities.

2.4.2 The effect of carbon additions

It has long been assumed that carbon removed silica and other oxygen impurities on the surface of silicon carbide [2, 56, 57]. This would lower surface free energy and improve mass transport. This assumption finds no confirmation in thermodynamic calculations [58-61] or experimental results [48, 62-64], yet carbon additions are vital for sintering SiC to high densities. Stobierski and Gubernat [65] recently conducted a series of sintering experiments with varying amounts of carbon in the range 1200-2200°C. Two of the resulting graphs are presented in Figure 20 and Figure 21.

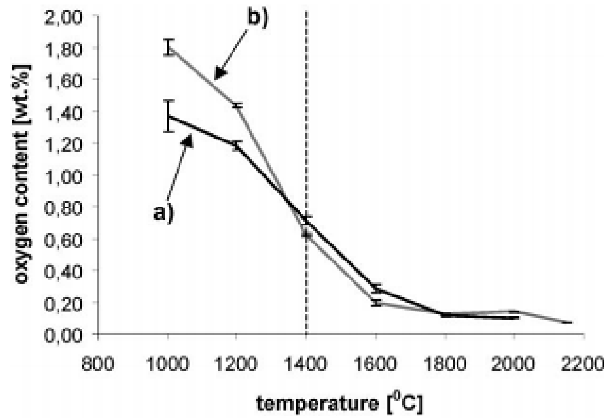

Figure 20. **Oxygen content as a function of temperature for a) SiC containing 3wt% carbon b) pure SiC. [65]**

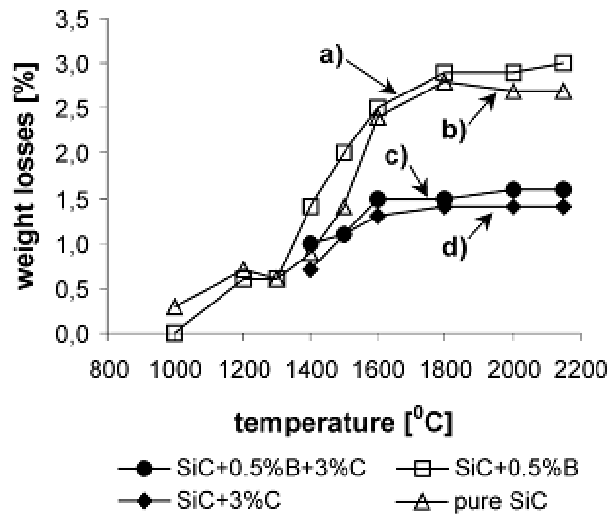

Figure 21. **Weight losses during sintering for the following systems: a) pure SiC b) SiC containing 0.5wt% B c) SiC containing 3wt% C d) SiC containing 3wt% C and 0.5wt% B. [65]**

Figure 20 shows that carbon does in fact reduce oxygen content at lower temperatures. Above 1400°C, the oxygen content has been reduced for both samples, proving that silicon carbide itself can remove silica and oxygen impurities at higher temperatures. Figure 21 suggests that carbon additions prevent mass losses in the temperature range 1400-1800°C. Stobierski and Gubernat [65] proposed that free carbon changes the reaction route for the silica, from

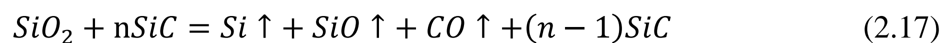

$$SiO_2 + \mathrm{n}SiC = Si \uparrow + SiO \uparrow + CO \uparrow + (n-1)SiC \tag{2.17}$$

to

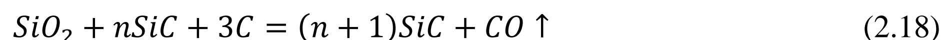

$$SiO_2 + nSiC + 3C = (n+1)SiC + CO \uparrow \tag{2.18}$$

Silicon vapor inside the SiC matrix can be detrimental to sintering, as it activates surface diffusion [65]. This mass transport mechanism increases grain growth, but does not lead to pore elimination and densification, as described in section 2.3.3. Carbon will start graphitize at high temperatures, and has been confirmed for the standard powder used in this work by T.

Bergh [66]. In summary, carbon limits ineffective mass transport mechanisms, and maintains small SiC grains until solid solution boron makes solid state diffusion possible.

2.4.3 The effect of boron nitride additions

As mentioned earlier, boron compounds like boron nitride act as sintering additives in silicon carbide [2]. The positive effect is limited by additions up to the solubility limit of the boron source [54], which is very limited for BN, and can only be measured indirectly [67]. Li et al. [3] conducted a series of experiments of pressureless sintering of silicon carbide with 0.25-8wt% added boron nitride. They observed a reduction in grain growth, a decrease in thermal conductivity and an increase in resistivity with increasing BN additions. Dissolved B and N at the SiC/BN interface, as well as increased grain boundary resistance from BN were thought to be responsible. The strong covalent bonds of both SiC and BN gave too low rate of interdiffusion to form solid solutions even at temperatures of 2150°C, and BN has very low solubility in SiC at room temperature [67]. Samples with BN additions above 6wt% had lower densities due to poor self-sinterability of BN and segregation of grain boundaries, which increases diffusion distances. Boron nitride often require external pressure to achieve high densities [4], and external pressure is believed to increase density of SiC containing high amounts of BN.

Li *et al.* [3] also measured the average weight-loss ratio of pure BN after sintering at 2150°C in argon, and was found to be ~4.61wt%. The theoretical density of sintered SiC-BN can therefore be well approximated by the rule of mixtures. Annealing after sintering at 1950°C for 6 hours reduced crystal defects, but lowered the final density. Higher BN content restrained grain growth, and SiC grains became more equiaxed.

2.5 Si-(B-)C-N ceramics and phase equilibriums

Si-(B-)C-N ceramics derived from preceramic polymers is a growing field of study, and the findings here may be of interest in SiC-BN composites. Schmidt [68] reports that Si-(B-)C-N ceramics show some differences to their SiC and Si_3N_4 counterparts: (1) amorphous phases does not crystallize until higher temperatures, (2) creep resistance is increased, (3) oxygen incorporation is enhanced in the amorphous phase. Annealing at temperatures above 1450°C leads to precipitation of nano-crystalline SiC and/or Si_3N_4. Quaternary regions of Si-B-C-N also show some stability up to 2000°C, which can be seen from Figure 22 below.

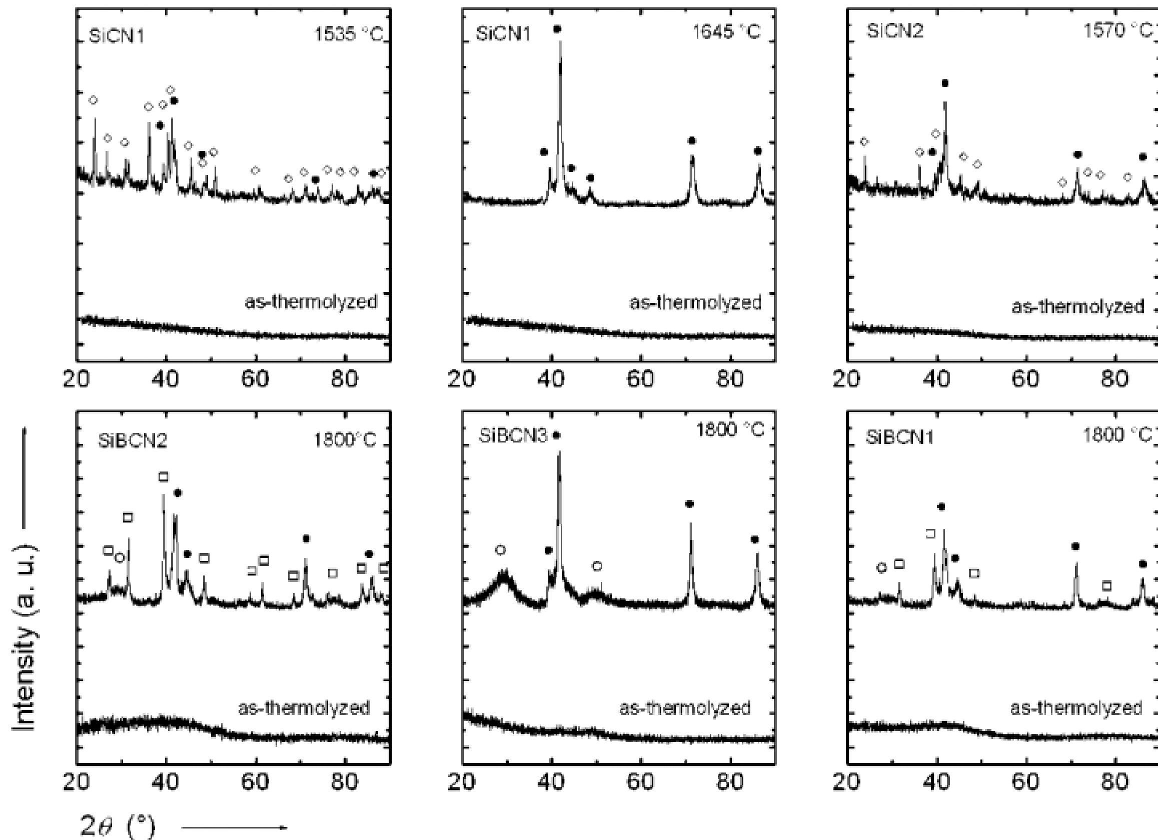

Figure 22. **X-ray diffractograms of various Si-(B-)C-N ceramics in the as-thermolyzed (produced from polymers) state and after annealing at elevated temperatures for 4H (temperature shown in top-right corner). The Bragg peaks corresponding to the crystallized phase are marked: SiC (●), α-Si_3N_4 (◊) and β-Si_3N_4 (□). The broad structure marked ○ is reminiscent of an amorphous phase. [68]**

Note that SiC and Si_3N_4 coexist in SiCN1 at 1535°C (top-left), but have been completely converted to SiC at 1645°C (top-middle). Schmidt suggests this may be caused by dissociation of Si_3N_4 in presence of C, as according to

$$Si_3N_4 + 3C \rightarrow 3SiC + 2N_2(g) \tag{2.19}$$

where nitrogen gas leaves the sample. According to the Si-C-N phase diagram presented by Seifert *et al*, the equilibrium temperature for this reaction is 1484°C at ambient pressure [69]. At temperatures above 1841°C, Si_3N_4 can dissociate directly according to

$$Si_3N_4 \rightarrow 3Si(l) + 2N_2(g) \quad (2.20)$$

However, Si_3N_4 is still present in SiBCN1 at 1800 degrees (lower-right in Figure 22). How does boron influence the reaction in (2.19) and (2.20)?

Fig. 23 shows phase equilibriums derived from quaternary isothermal sections, as well as concentration sections in Fig. 24. Upon heating from 1673 K to 2273 K, the precipitated Si_3N_4 is no longer stable, and should react according to (2.19) or dissociate according to (2.20). The presence of stable regions of Si_3N_4 at high temperatures has been explained as a kinetic phenomenon, not a thermodynamic one [68, 70, 71].

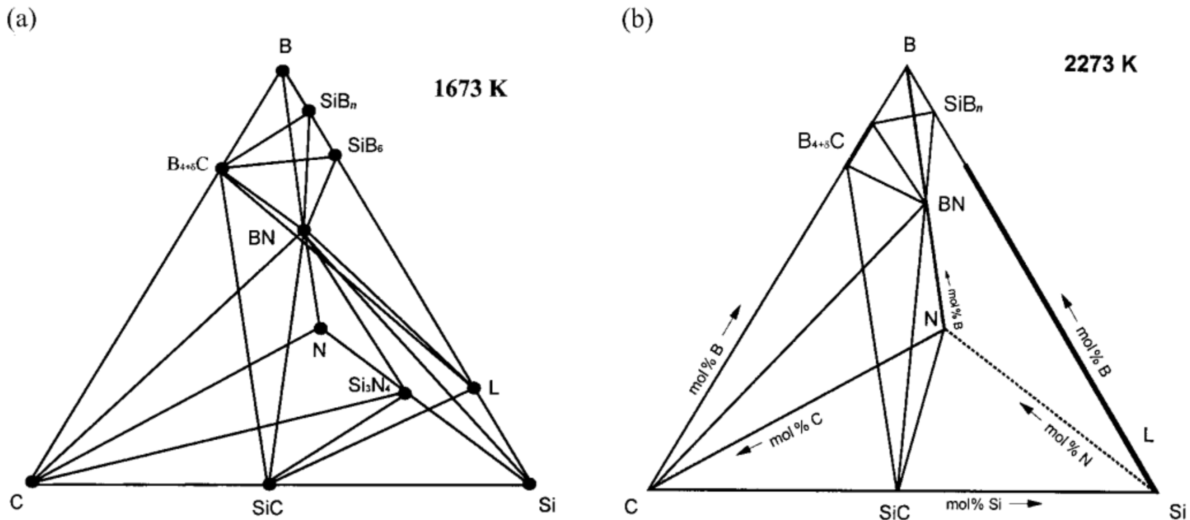

Figure 23. Isothermal sections in the Si-B-C-N system at T = (a) 1673 K and (b) 2273 K. [71]

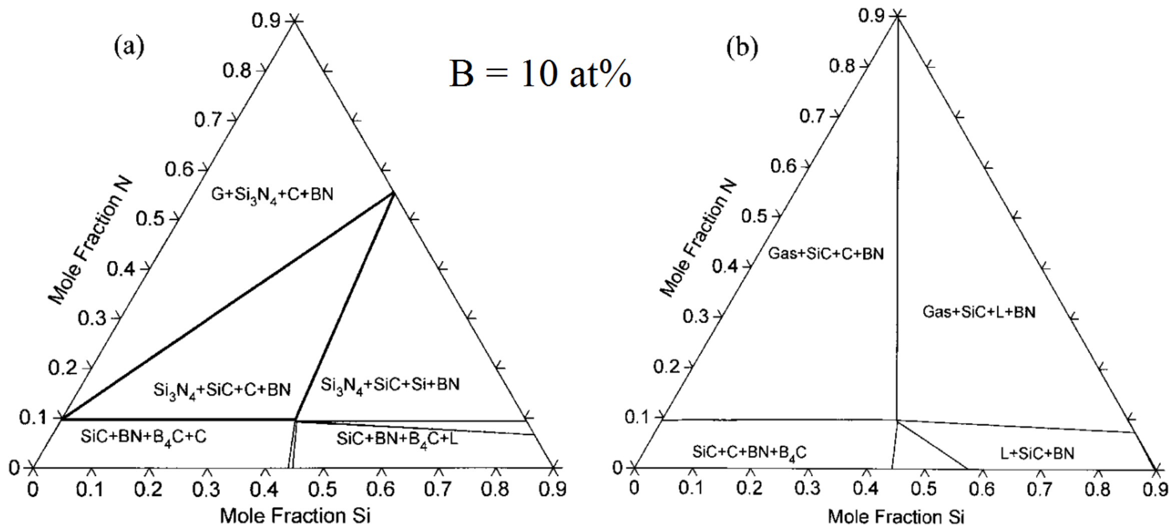

Figure 24. Concentration sections in the Si-B-C-N system at constant boron content (10 at%) and temperatures (a) 1673 K and (b) 2273 K. [71]

High resolution transmission electron microscopy (HRTEM) of Si_3N_4 regions reveal that they are surrounded by turbostratic (out of alignment) B-N-C layers, see Fig. 25 [72]. Electron energy loss spectrum (EELS) show a B:N:C ratio of 1:1:3.3 in the region separating SiC and Si_3N_4, with less carbon close to the Si_3N_4 side.

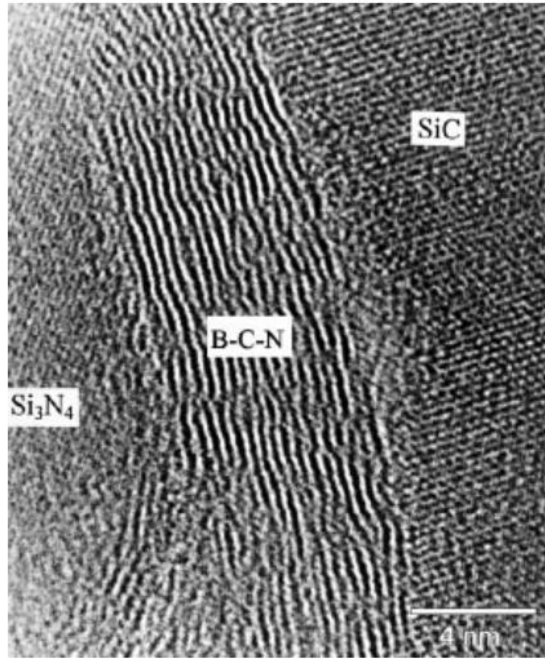

Figure 25. HRTEM image of polymer derived Si-B-C-N ceramic after annealing at 1800°C for 50 h in nitrogen atmosphere. [72]

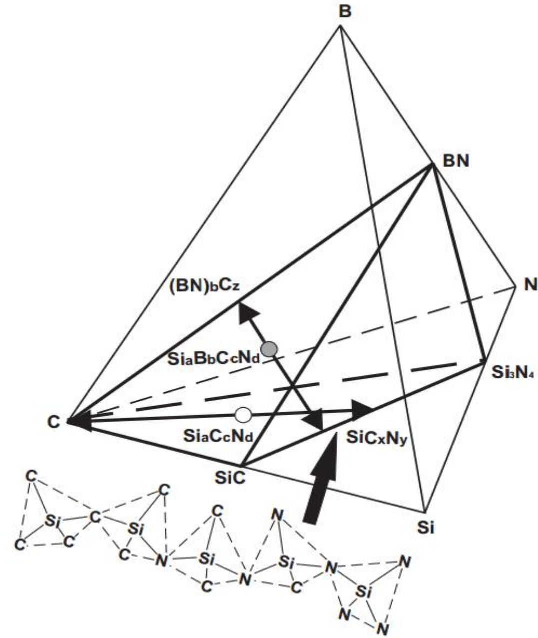

Figure 26. Schematic illustration of phase separation of $Si_aC_cN_d$ and $Si_aB_bC_cN_d$ compositions, falling within the limit of the three-phase region SiC-Si3N4-C and the four-phase region SiC-Si3N4-BN-C of the quaternary Si-B-C-N system, respectively. [70]

BNC regions separate SiC and Si_3N_4 grains when there is a large amount of BNC available, and Fig. 26 shows how short regions of Si-C-N can separate the phases when there is less BNC available. This segregation retards crystal growth [73], and may also cause an increase in local N_2 gas pressure [68]. It is uncertain if BNC regions should be interpreted as homogenous phases or a mechanical mixture of intercalated (layered structure without chemical bonding between layers) BN and graphite layers [71, 74].

The equilibrium condition of (2.19) can be expressed as

$$\frac{p_{N_2}^2 a_{SiC}^3}{a_{Si_3N_4} a_C^3} = exp\left(-\frac{\Delta G^0}{RT_e}\right) \tag{2.21}$$

where ΔG^0 is the standard Gibbs free energy, p_{N_2} is the nitrogen partial pressure and a_i is the activity of compound i. If the activity of solid compounds is assumed to be 1, equilibrium temperature T_e is determined only by nitrogen partial pressure. According to Seifert *et al.* [69], T_e = 1900°C for $p_{N_2} = 30\ bar$. Maintaining such high internal pressure over long annealing times would require that nitrogen cannot diffuse away from the grains. Although

that is unlikely, Friess *et al.* [75] have demonstrated that decomposition of Si_3N_4 in Si-C-N ceramics is sensitive to nitrogen pressure, which indicates that local nitrogen overpressure plays a considerable role in Si_3N_4 stabilization in Si-C-N ceramics.

It has also been suggested that the presence of BN reduces carbon activity due to formation of BNC_x regions. Equation (2.18) shows that a reduction in carbon activity can have the same effect as nitrogen partial pressure increase, and thus increase the reaction temperature. A decrease of activity to at least $a_c = 0.1$ in BNC_x would cause the same shift as 30 bar nitrogen overpressure, and is not unreasonable. A combination of the effects might also be possible. Figure 27 shows temperature-activity (a_c) diagram in the Si-C-N system with lines for 1 and 10 bar nitrogen partial pressure. It is shown here that Si_3N_4 could be thermodynamically stable at given conditions.

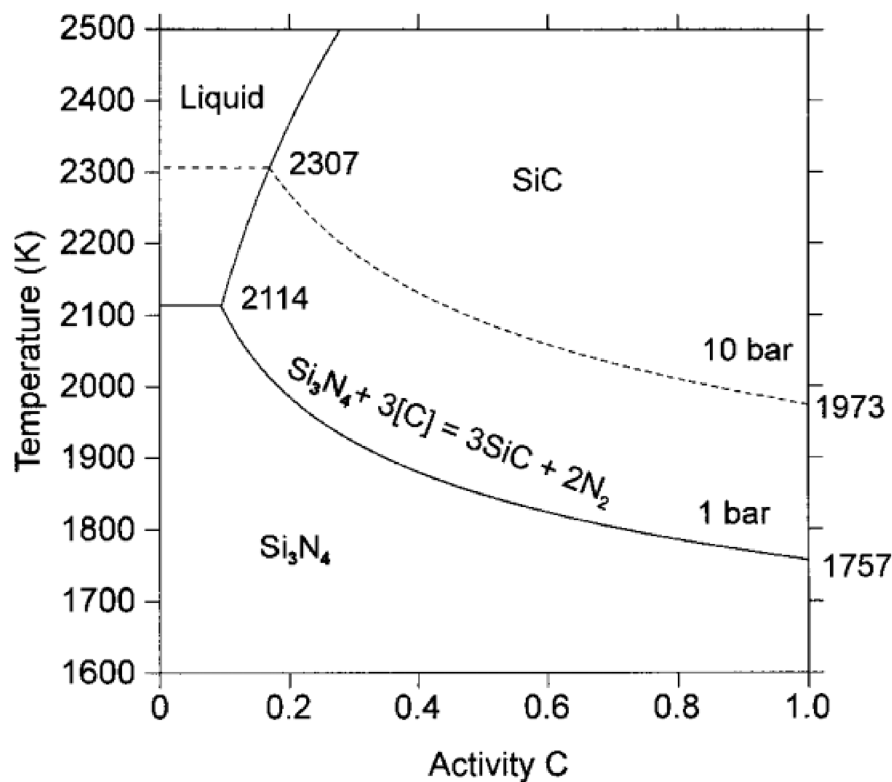

Figure 27. **Temperature-activity (a_c) diagram in the Si-C-N system. Pressures are nitrogen partial pressures. [71]**

2.6 Glow Discharge Optical Emission Spectroscopy (GDOES)

Glow discharge optical emission spectroscopy provides fast, direct bulk analysis and depth profiling of solid materials. The method is in many regards similar to secondary ion mass spectroscopy, but is faster and provides more reliable quantification. Both conducting and non-conducting samples can be investigated.

The GDOES technique is built up of two parts: Glow discharge, which is cathodic ion sputtering of a surface, and optical emission spectroscopy, which is material identification based on photon emission from relaxing electrons. The process is illustrated below in Figure 28.

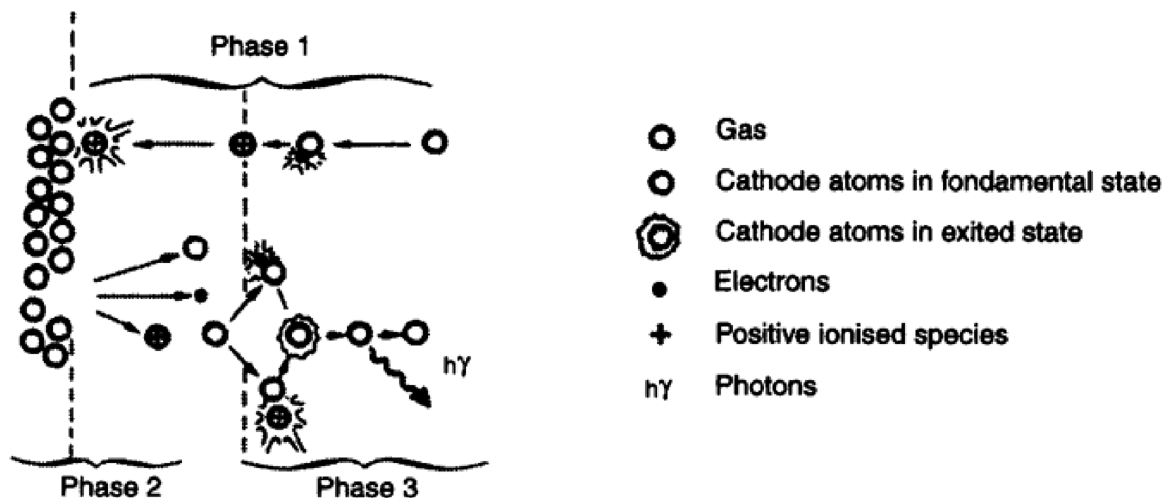

Figure 28. Illustration of the GDOES process. In phase 1, argon atoms are ionized and bombard the cathode surface. In phase 2, sample and argon atoms and ions, as well as electrons, are ejected from the sample surface and join the plasma in the firing chamber. In phase 3, the atoms are excited by electrons and ions in the plasma, and will then eject a photon. This photon will then be analyzed by an optical spectrometer. [76]

The high-energy sputtering will successively knock out atom layers, digging further and further into the sample surface. This makes depth profiling possible. Ejected atoms join the plasma in the firing chamber, and will be excited by collision with electrons and ions. Electron relaxation leads to photon emissions, which are characteristic for each atom. The emissions are recorded by an optical spectrometer, and their intensities are recorded as a function of time. By measuring the end-of-measurement depth, the intensity at each point in time can be linearly approximated to depth. A reference sample can transform the intensities into quantitative results. Without a relevant reference material, intensities can still be investigated relatively for each element, as long as the samples are relatively similar in composition and structure; lower intensity for element A in sample 2 than sample 1 indicate lower composition or stronger element A bonds in sample two. More on this below.

There are three processes in generating the analytical signal [77]:

1. Supply of sputtered atoms
2. Excitation followed by photon emission
3. Detection of photons

Since the spectrometer is looking into the plasma, and not at the sample surface, it is normally assumed that these processes are independent. The recorded signal for a given emission line for element i is given by

$$I_i = k_i e_i q_i \tag{2.22}$$

where q_i is the supply rate of element i into the plasma, e_i represents the emission process and k_i is the instrumental detection efficiency. The supply rate is equal to the sputtering rate. For relative analysis of roughly similar samples, k_i and e_i can be assumed constant for each element i. The intensity differences are therefore only caused by changes in sputtering rates, and sputtering of material from the sample to the plasma is the key to quantitative analysis of the surface.

Smentkowski [78] has published a review of sputtering trends. In it, he summarized both the developments in sputtering theory and the experience of more than a hundred researchers. Listed below are the key trends believed to be most relevant to this work. Sputtering yield is the same as sputtering rate, since instrument parameters are kept constant in relative analysis.

- Sputtering yield is different for different elements. Within a period of the periodic table, the sputtering rate increases from left to right (as the shells fill with electrons).
- Sputtering yield increases reciprocal to binding energy.
- Sputtering yield decreases with increasing surface roughness. Smooth surfaces have higher yields than rough surfaces.
- For multicomponent samples, the light weight component is preferentially sputtered. The sputtering rate of each component increases as the reciprocal of the binding energy and mass of that component.
- SiC is easily amorphized by sputtering.

In addition, binding energy for atoms on grain edges and grain boundaries are lower than within grains. This was believed to cause higher yields for materials with small grains, and was confirmed by Jurac *et al.* [79] using Monte Carlo simulations.

2.7 Electron Backscatter Diffraction

The term "Electron backscatter diffraction" is synonymous with both the scanning electron microscopy (SEM) technique, as well as the accessory attached to an SEM [80]. EBSD provides quantitative information about crystallography in metals, minerals, semi-conductors and ceramics – most inorganic materials. The technique reveals grain sizes, grain boundary properties, grain orientations, texture and phase composition of the sample. Everything from centimeter-sized samples with millimeter-sized grains to metal thin films with nano-sized grains can be analyzed. The nominal angular resolution is limited to ~0.5° and the spatial resolution is limited to the resolution of the SEM. Modern field emission-SEMs (FE-SEM) can analyze 20nm grains with relatively good accuracy [81]. The maximum sample size is limited by the SEM's ability to tilt the sample to 70 degrees with an appropriate working distance, usually 5 to 30nm.

Electron backscatter diffraction operates by arranging a flat, highly polished sample at an angle of 70° (20° relative to electron beam), with a phosphorous screen at 90° (parallel with the electron beam) close to the sample, see Figure 29. With accelerating voltages in the region 10-30 kV, and incident current beams of 1-50 nA, electrons exit the sample with certain diffraction lines that depend on the crystal structure and orientation, see Figure 30. These lines are called Kikuchi lines after Seishi Kikuchi, who was the first to report these lines in 1928 [82]. With the beam stationary, an EBSD pattern emanates spherically from this point, and hits the phosphorous screen. The setup is sketched in Fig. 29.

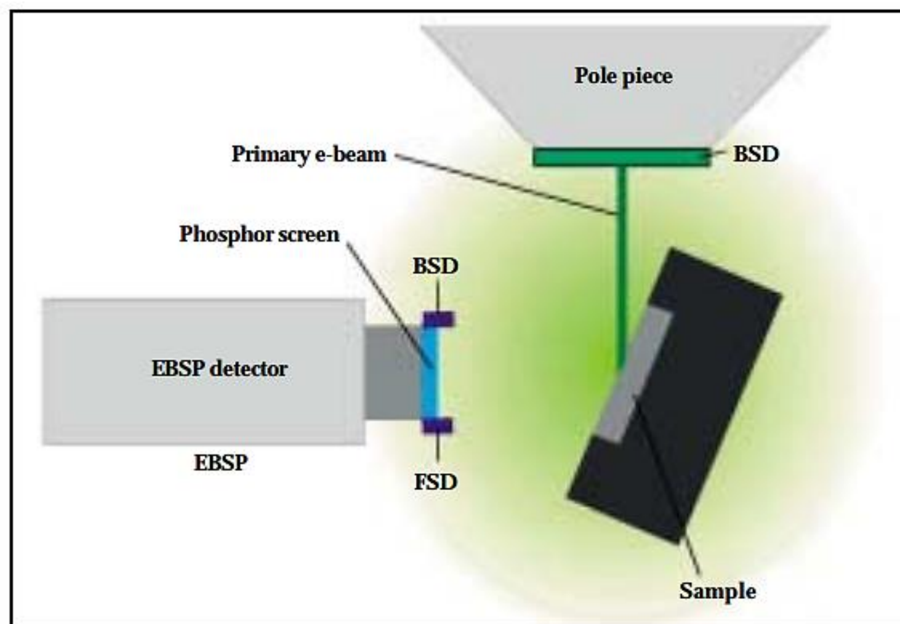

Figure 29. Illustration of sample and EBSD detector placement during EBSD operation. [83]

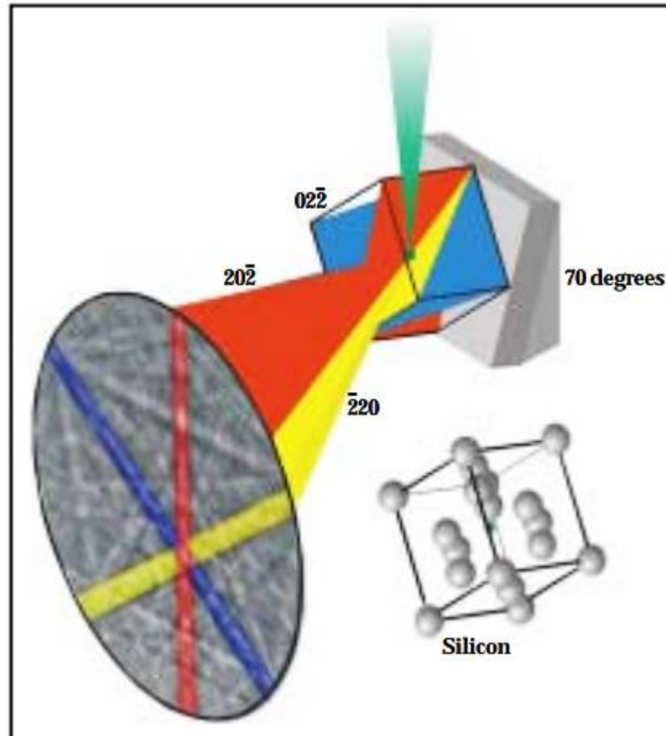

Figure 30. Schematic of electron diffraction in silicon with crystal planes and associated diffraction bands shown. [83]

Behind the phosphorous screen is a digital camera that captures the Kikuchi lines on the screen, as seen in Fig. 30. The sum of these lines result in a Kikuchi pattern, which is uniquely defined by the lattice parameters of the particular crystal; the crystal's orientation; the wavelength of the incident electron beam (which is proportional to the acceleration voltage) and the distance between sample and phosphorous screen. With *a priori* information about possible phases in the sample, specialized software determines Kikuchi patterns for all possible orientations, and returns the best fitting phase and orientation for each pattern recorded.

The SEM's ability to scan the beam over the sample surface enables mapping of structure and orientation of an entire surface region. With increasing processing power and scan speeds, this has become a practical and common method for microstructure investigation. However, the process still consumes large amounts of processing power and storage data. This is due to a 2D image on the phosphorous screen is analyzed for each point on the sample surface. Imagine that a 512 X 512 pixel area on the sample is to be investigated with a 512 X 512 pixel EBSD pattern stored in an 8 bit format. This would equate to 512^2 X 512^2 X 8 bit = 68.7 GB of raw, uncompressed data! This amount of data is rarely stored in practice, as only position, phase, orientation and some data quality is needed for most applications.

3 Experimental

3.1 Powders and Equipment

To investigate the hot-pressing properties of SiC containing high amounts of BN, three powders were produced at Saint-Gobain Ceramic Materials AS Lillesand. The first is a standard ready-to-press (RTP, spray dried with organic binder and additives) powder used for comparison, the others contain 5 and 10wt% h-BN respectively. The powders are listed in Table 4.

Table 4. SiC and SiC-BN powders hot-pressed in this report

Powder name	Description	Notation
Densitec 15H	This is a standard RTP powder sold by Saint-Gobain	SiC-0BN
D15H with 5wt% BN	This powder is identical to Densitec 15H, but 5wt% solid, hexagonal boron nitride has been added to the slurry before spray draying	SiC-5BN
D15H with 10wt% BN	Same as SiC-B5BN, but with 10wt% boron nitride	SiC-10BN

The RTP powders were all based on the same sub-micron SiC powder, Sintex 15C (see Appendix A), spray-dried with binders and sintering additives. Spray drying has been performed to maximize die filling. The composition for Sintex 15 is shown in Fig. 31.

Particle Size Distribution

Ds90% µm	Ds50% µm	Ds10% µm
1.5 max	0.40-0.60	0.15 - 0.28

Measured by SediGraph

Specific surface area: 14.0-16.0 m^2/g

Chemistry:

Free C % max.	Free Si % max.	Total oxygen % max.	Fe % max.
0.25	0.15	0,85	0,02

Measured according to ANSI B74. 15   Based on Leco   Based on XRF

Figure 31. **Particle size distribution, specific surface energy and chemistry of the silicon carbide starting powder before spray drying.**

The standard powder has been spray-dried with polyvinyl alcohol, carbon black and boron carbide. Table 5 lists approximate additions. For SiC 5BN and SiC 10BN, 5 and 10wt% solid, hexagonal boron nitride was also added to the slurry before spray drying. The equipment used in this work are listed in Table 6.

Table 5. Composition of SiC 0BN powder

Product name	Carbon black	Boron carbide	Binder content	Binder type	Moisture content
Densitec 15H	2-3wt%	1.2wt%	Approx. 2wt%	PVA	Approx. 0.6wt%

Table 6. List of equipment used in this work

Equipment	Manufacturer and type	Application
Hot-press	Thermal Technology Inc. HP-7010G	Sintering with external pressure
GDOES	Horiba Scientific GD-profiler 2	Relative composition measurements
Scanning electron microscope	Zeiss Ultra V55 Field Emission SEM (FE-SEM) with EBSD detector	Study phase composition and grain orientation
Polishing	Struers SiC and diamond disks 200-1200µm Diamond suspensions 9, 3 and 1µm particles	Surface preparation for SEM
Ion milling	Hitachi IM-3000 flat milling system	High-quality surface preparation for SEM
XRD	D8 DaVinci	Study of crystal structures
Archimedes’	Mettler Toledo	Measure sintered density

3.2 Procedures

3.2.1 Powder preparation

The powders were received ready for hot-pressing, spray-dried with organic binders and sintering additives. No powder modifications or preconsolidation has been made after receiving them. Table 4 and 5 show the technical data for SiC 0BN, and technical documentation can be found in appendix A and B.

3.2.2 Hot-press description

The hot-press used in this project is a resistively heated graphite furnace, photographed in Fig. 32 and sketched schematically in Fig. 34. Powder is poured into a mold with two punches (Fig. 33), and inserted in the hot-zone (orange area in Fig. 34). The apparatus is connected to a hydraulic pump which applies pressure to the lower graphite column, pushing it upwards and into the hot-zone. The oven is connected to a rotary pump for evacuation to 3 millibar, and a gas bottle system for gas flow. Argon 5.0 (99.999% pure) has been used at 1atm for hot-pressing. Temperature is measured with a thermocouple at low temperatures, and a pyrometer at high temperatures.

Figure 32. Picture of the hot-press.

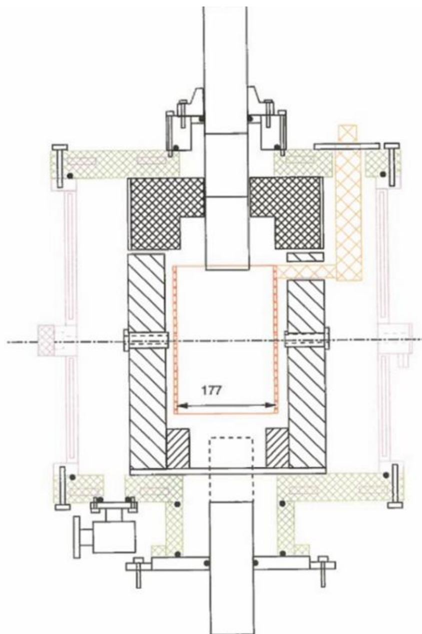

Figure 34. Schematic drawing of the hot-press used in this work.

Figure 33. Picture of graphite molds used for hot-pressing.

3.2.3 Sintering procedure

6 grams of powder was poured into a graphite cylinder with diameter 25 mm, with graphite punches (see Fig. 33) on each end. Care was taken to get an even powder level, to not induce pressure gradients. The hot-pressing furnace was evacuated to 3 millibar using a rotary pump, and backfilled three times with argon 5.0 gas (99.999% pure), the last time until 1 bar. An outlet was then opened to create a slow argon flow through the furnace. The pressing ram would then apply uniaxial pressure on the mold at the lowest setting, 4.3 MPa

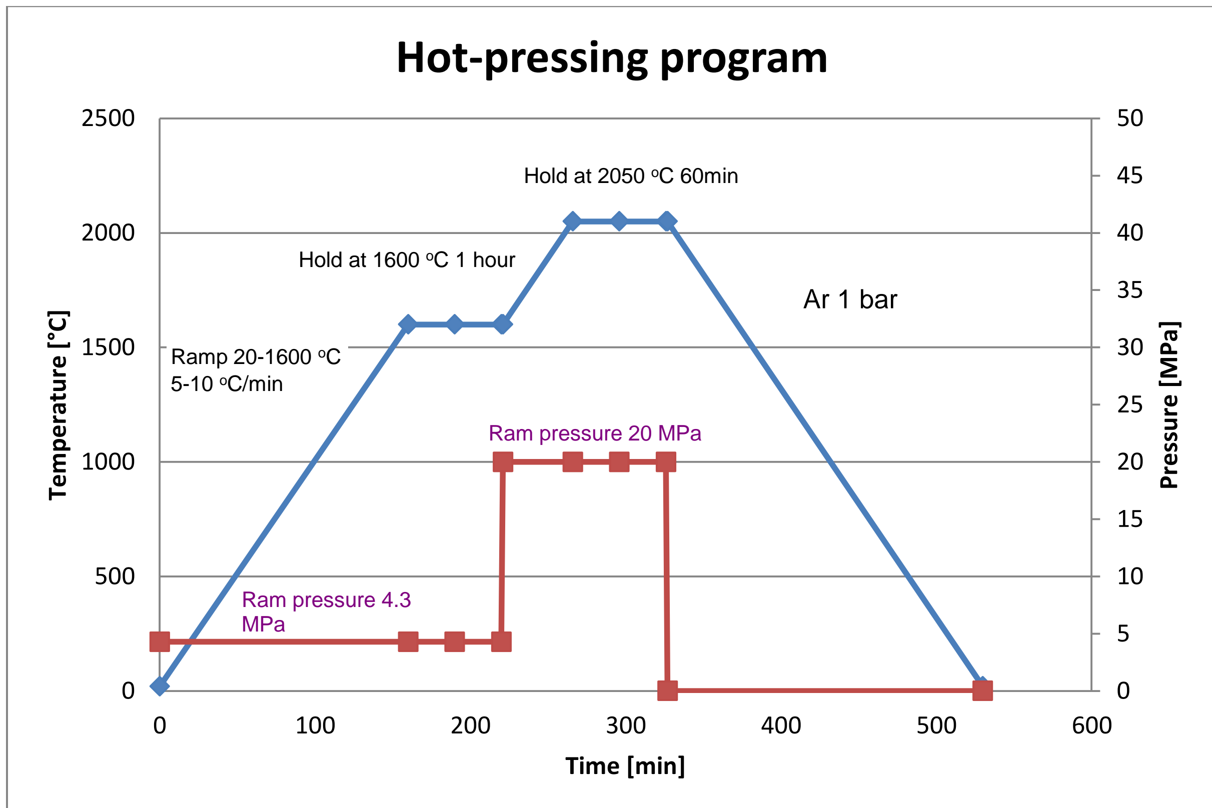

Figure 35. Standard hot-pressing program for sintering SiC-0BN.

The standard hot-pressing program for SiC 0BN is shown in Fig. 35. The temperature was increased to 1600°C at a rate of 10°C/min, and kept at this temperature for 1 hour. This is to stabilize the system (gas pressure, higher mechanical pressure, etc.). The mechanical pressure was then increased to 20 MPa and the temperature increased to 2050°C at 10°C/min, and held at this temperature for 1 hour. At the end of the dwell time, the pressure was removed, and the apparatus cooled at 10°C/min. Faster cooling rates may have been possible, but would increase equipment wear. The gas flow and water cooling was turned off around 90°C and left to cool overnight. Graphite felt and graphite disks were used to reduce punch wear. The resulting sintered body was removed using a uniaxial press, and graphite residue was removed with an abrasive disk.

Following the standard procedure, hot-pressing was stopped upon reaching either of the holding times, halfway into holding times, and after holding. The naming pattern used in this work is shown in Table 7, with n being 0, 5 or 10.

Table 7. **Sample naming pattern related to hot-pressing program. X means the mentioned temperature has not been reached, while 0 means hot-pressing was stopped upon reaching said temperature. a has the value 0, 5 or 10.**

Name	Time at 1600°C [min]	Time at 2050°C [min]	Total hot-pressing time [min]	Highest pressure [MPa]
SiC-nBN Powder	X	X	0	X
SiC-nBN 1600 0min	0	X	160	4.3
SiC-nBN 1600 30min	30	X	190	4.3
SiC-nBN 1600 60min	60	X	220	4.3
SiC-nBN 0min	60	0	266	20
SiC-nBN 30min	60	30	296	20
SiC-nBN 60min	60	60	326	20

3.2.4 X-ray diffraction

All samples, powder, heat-treated and sintered, were scanned in a D8 Advance Da-Vinci working in Bragg-Brentano geometry (2θ-θ). The diffractometer scanned from 2θ=20-80° for 1 hour using varying slit (V6). Cu K_α X-rays with wavelength 1.54060 nm was used. Rietveld refinement in *Topas* software version 5 was used for post-scanning analysis.

3.2.5 Glow Discharge Optical Emission Spectroscopy (GDOES)

The GDOES used was a GD-profiler 2 from Horiba Scientific with an argon plasma source. The apparatus had a window of 4 mm in diameter aimed at the flat sample surface, with a vacuum of 400 Pa holding the sample in place. The surface was first cleaned with light plasma cleaning, before 20 W of 4 V of energy was applied at 3000 Hz for 120 seconds. All relevant emissions were recorded, and the resulting penetration depth was estimated from SEM images of the craters at an angle. The GDOES program was provided by the supplier, but originally designed for SiC coatings. No program variations were tested.

3.2.6 Electron Backscatter Diffraction

Sintered samples were broken into two or more pieces and cast in an epoxy mold, with one fracture surface and one flat surface pointing down. The samples were then grinded in an automatic Struers grinding machine with MD-Piano diamond discs, which contains diamond particles in an organic matrix. The samples were then polished in another automatic Struers machine with diamond suspensions containing 9 µm, 3 µm and 1 µm, successively.

The samples were then plasma ion milled to remove polishing lines. This was performed at an 80° angle using argon gas with 6, 4 and 2 kV acceleration voltage successively, with 5 minutes at each step and a rotating stage. The polishing lines were removed at high kV, but this also amorphized the SiC structure. Lower energies would then remove the amorphized layer. The samples were left in chloroform overnight to dissolve the epoxy, and cleaned with acetone in an ultrasound bath.

The polished samples were mounted on conducting sample holders using carbon tape for flat surfaces, while the polished fracture surfaces were fastened in a conducting screw sample holder. The SEM used was a Zeiss Ultra 55 FE-SEM, and all images were taken at 1k magnification, with 20 keV acceleration voltage, 300 µm aperture and 70° tilt angle. The region scanned was 50 µm times 50 µm. The Nordiff UF-1100 software was used for EBSD pattern acquisition, while EDAX-TSL OIM 7.3 software was used for analysis. Silicon carbide patterns already in the software were used for calibration.

4 Results

4.1 Powder description

The powders hot-pressed in this work have been studied in the author's specialization project [84]. The size distribution is shown in Fig. 36 and 37, and was measured by dry laser diffraction. Fig. 38-40 show SEM images of the powder.

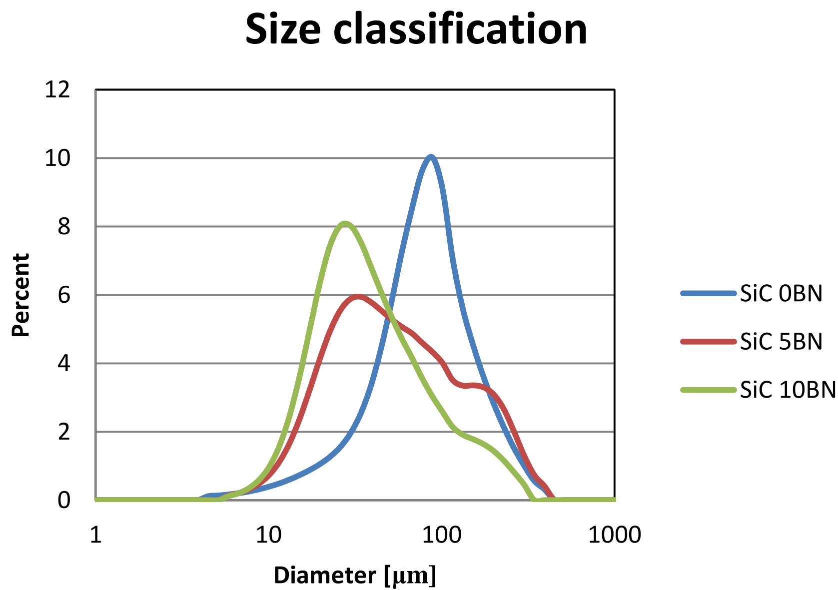

Figure 36. **Agglomerate size distribution measured by dry laser diffraction for the author's specialization project. [81]**

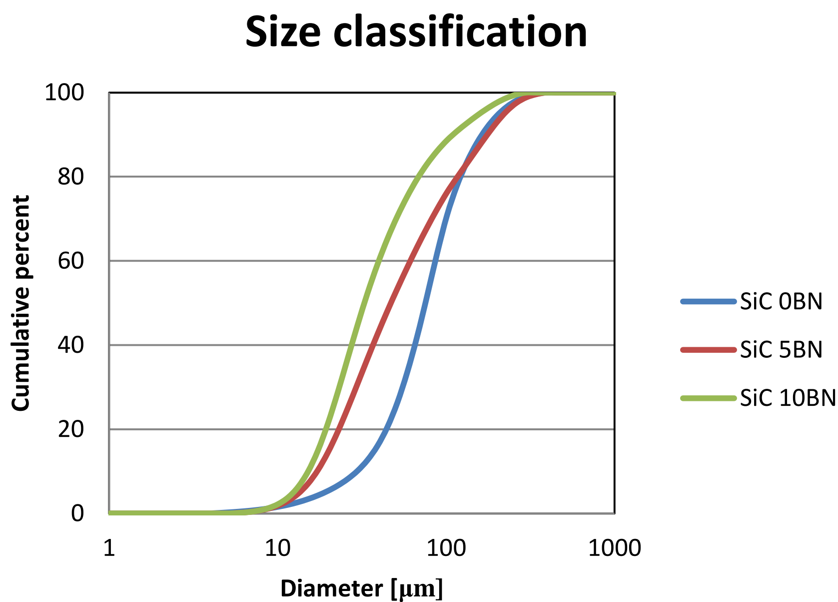

Figure 37. **Cumulative agglomerate size distribution measured by dry laser diffraction for the author's specialization project. [81]**

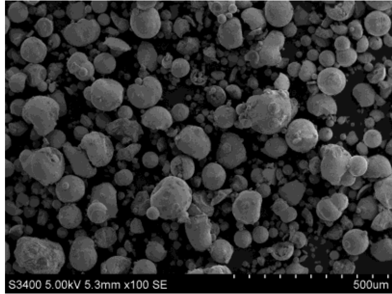

Figure 39. Secondary electron image of SiC 0BN powder for the author's specialization project. [81]

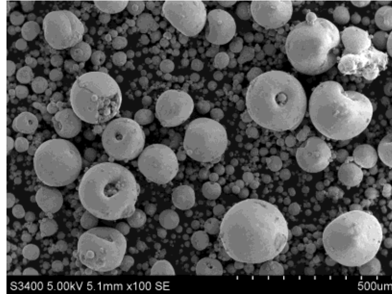

Figure 38. Secondary electron image of SiC 5BN powder for the author's specialization project. [81]

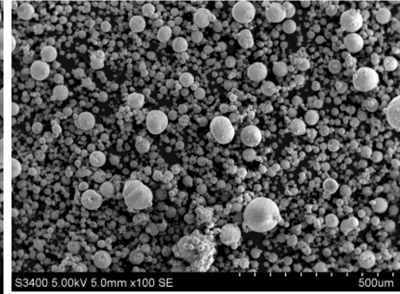

Figure 40. Secondary electron image of SiC 10BN powder for the author's specialization project. [81]

The spray-drying has created soft agglomerates with a much larger size than the SiC particles (10-140 µm vs 0.5-0.6 µm). Both size classifications in Fig. 36-37 and SEM images in Fig. 38-40 show differences in agglomerate sizes. SiC 0BN has a narrower distribution and higher average agglomerate size, while both powders with BN have more agglomerates of smaller sizes. SiC 5BN has the largest agglomerates. It is not expected that this will affect sintering properties in hot-pressing, as the uniaxial pressure will crush the soft agglomerates and fill the die regardless. Grain boundaries are also expected to slide against each other as the temperature is increased, cf. section 2.3.1.

4.2 Densities

The densities of all samples were measured using Archimedes' principle in water. The results are presented in Fig. 41 and 42. Theoretical densities were calculated using rule of mixture between SiC (3.21 g/cm^3) and BN (2.1 g/cm^3). Carbon and boron carbide content have not been included in the calculations.

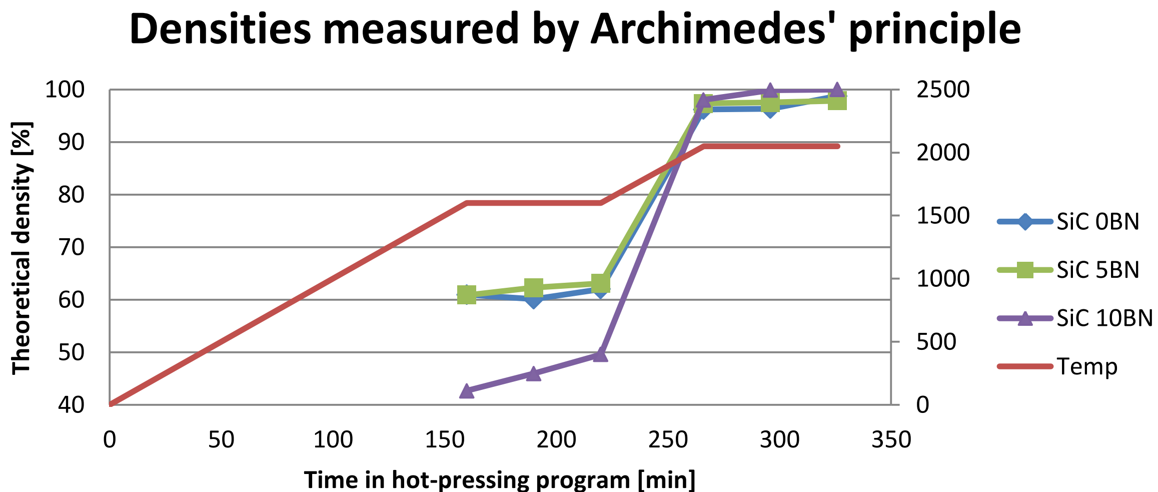

Figure 41. Densities of hot-pressed samples, as measured by Archimedes' principle. The red line corresponds to the temperature reached in the hot-pressing program.

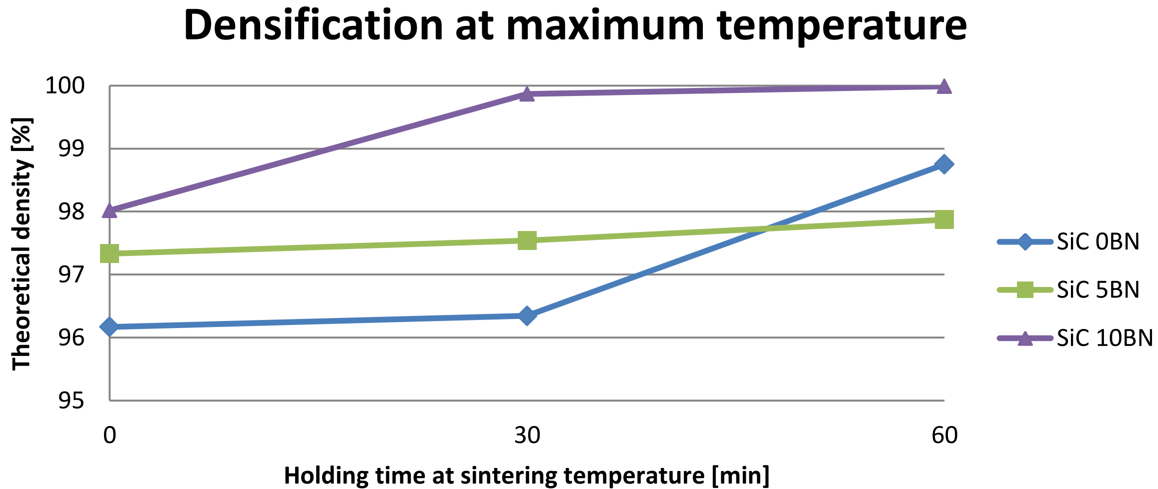

Figure 42. Densities of samples held at 2050°C for different times.

Fig. 41 shows that SiC 0BN and SiC 5BN has plateaued right above 60% of theoretical density at 1600 °C, SiC 10BN is not as dense, and is still densifying in this range. Upon heating to 2050 °C and increase in pressure to 20 MPa, all samples achieved densities above 95% of theoretical density.

4.3 X-ray diffraction

Fig. 43 shows stacked XRD scans for SiC 10BN. The scans are stacked with powder at the bottom and fully sintered samples at the top. No new peaks appeared over the sintering program, except a graphite peak (noted (●)) near the boron peak (noted (■)) appearing upon reaching 2050 °C. Graphitization of the excess graphite is not unexpected, but comparing Fig. 43, which is SiC 0BN, and Fig. 44, which is SiC 10BN, show a lower intensity for graphite for SiC 0BN in this range, with no graphite peak at 60 minute holding time. Graphite particles have been confirmed by T. Bergh [66] in SiC 0BN, but are not seen in the same range as the graphite in SiC 10BN. The graphite may be masked by SiC peaks.

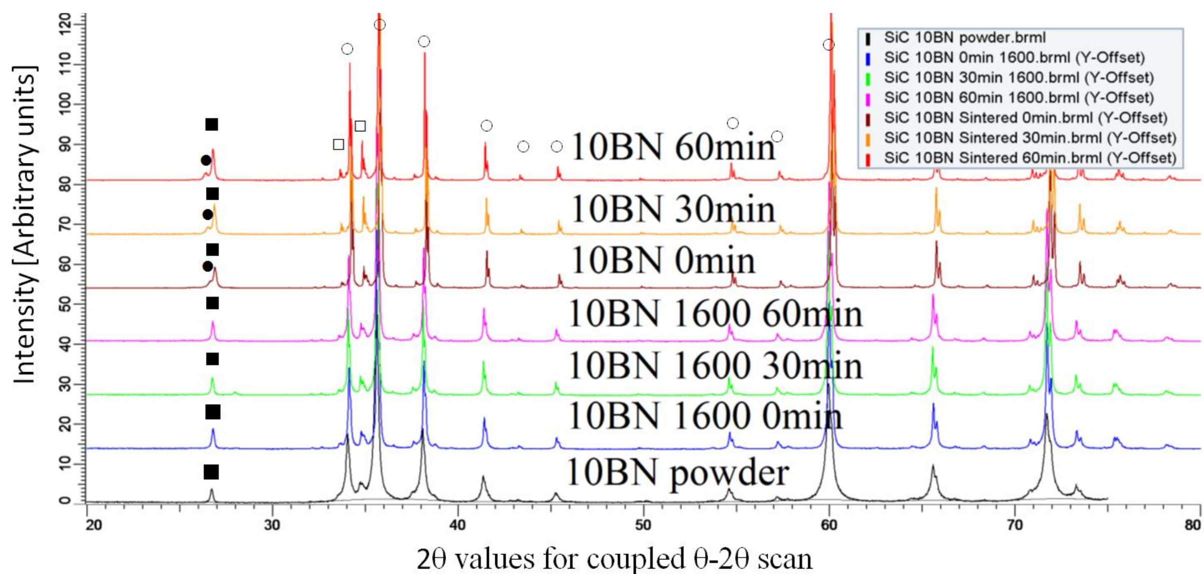

Figure 43. **Stacked XRD scans for SiC 10BN samples. (□) signifies SiC 4H from *Topas* structure fitting, (○) SiC 6H from COD #9010158, (■) BN from COD #9008997, (●) graphite from COD #9008569. Note that the scans are stacked in ascending order of hot-pressing, while the legend is in descending order. The**

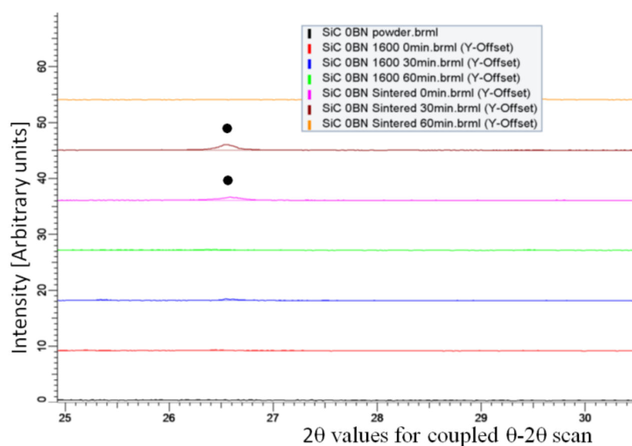

Figure 44. **XRD-scans of SiC 0BN zoomed at the BN-C peaks in the range 25-30°. The graphite peaks are marked with (●).**

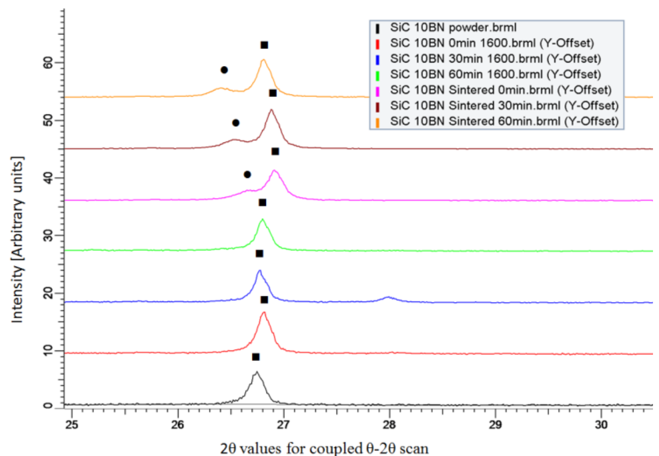

Figure 45. **XRD-scans of SiC 10BN zoomed at the BN-C peaks in the range 25-30°. (■) signifies BN-peak, (●) graphite peak.**

The peaks for SiC and BN do not shift much left or right, indicating small changes in lattice parameter (see zoomed region in Fig. 46). The lattice parameter changes are shown in Fig. 47 for SiC, and the d-spacing in Fig. 48 for BN and graphite.

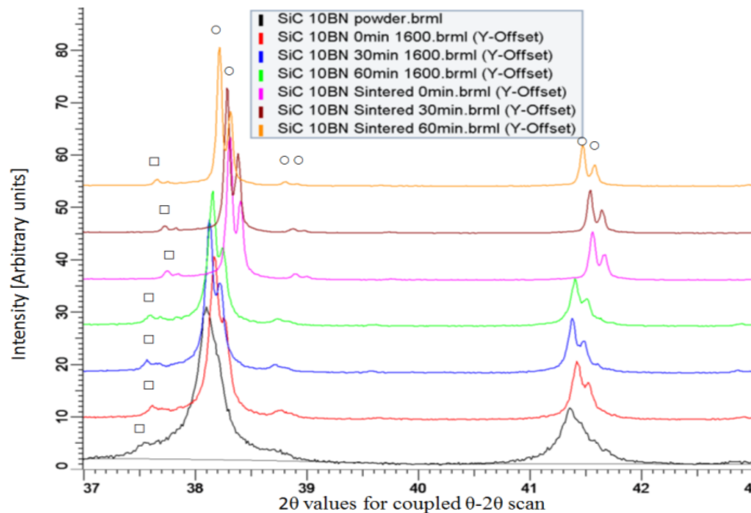

Figure 46. XRD scans for SiC 10BN showing small changes in lattice parameter for SiC with sintering. (□) signifies SiC 4H, (○) SiC 6H.

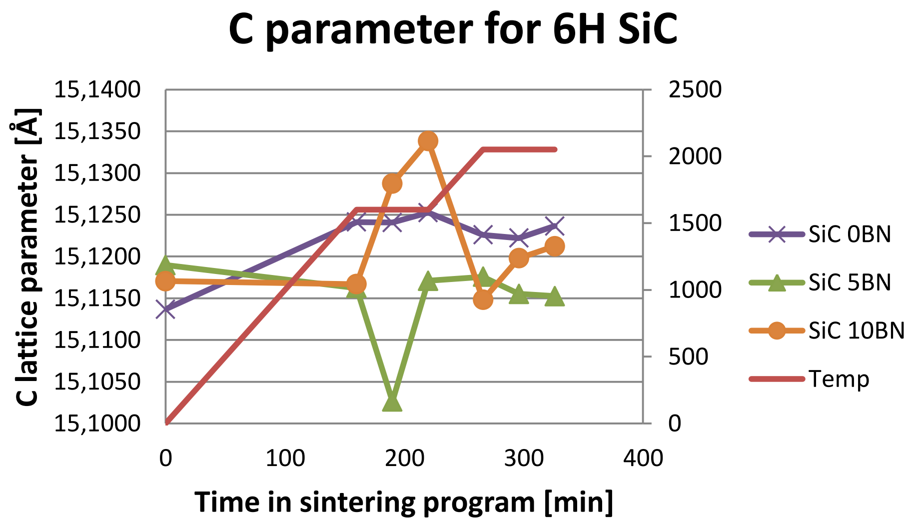

Figure 47. Changes in c-parameter for 6H SiC as measured by *Topas* software. The lines are a guide to the eye.

BN and graphite structures were created in the *Topas* software to measure weight percent and lattice parameters. The turbostratic nature of the overlapping structures gave poor Rietveld fit, and d-spacing, measured manually, was performed instead.

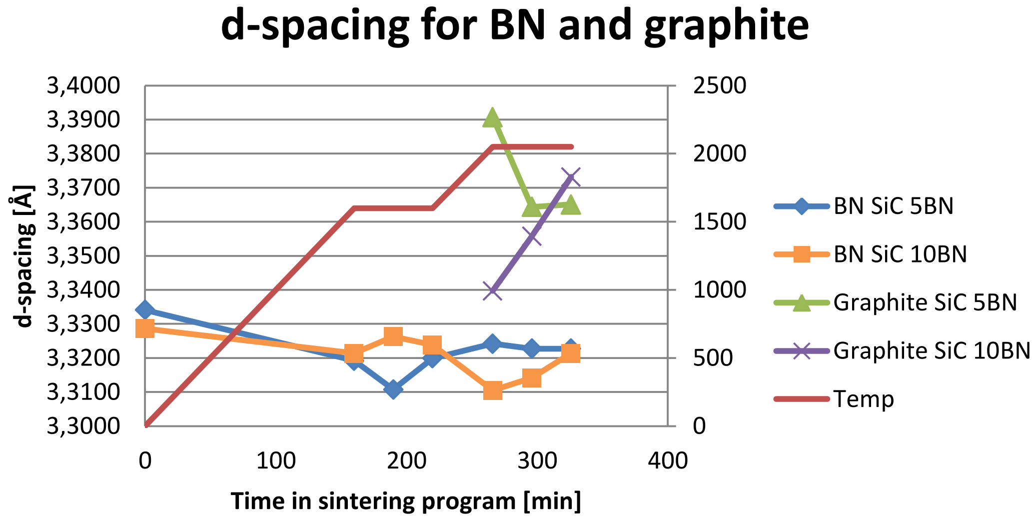

Figure 48. **d-spacing for BN and graphite peaks, as measured manually in *EVA* software. The lines are a guide to the eye.**

Fig. 49 shows the 4H to 6H ratio measured by *Topas*.

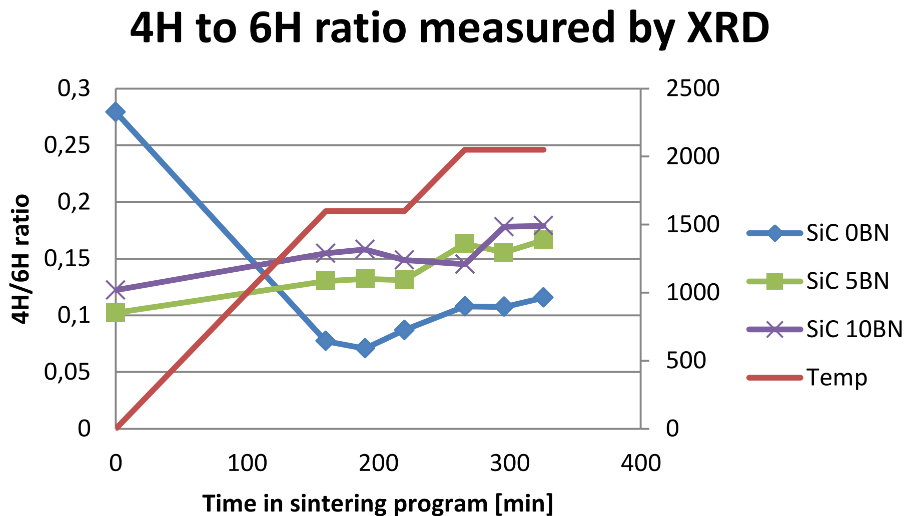

Figure 49. **4H to 6H ratio as measured by Rietveld fitting in *Topas*. The lines are a guide to the eye.**

4.4 Electron backscatter diffraction

The results from the EBSD scans can be displayed as three images: Secondary electron image for topography (Fig. 51.), phase map for composition (Fig. .) and inverse pole figure (IPF) (Fig. 49) for orientation. The phase map is coded green for SiC 6H and red for 4H. Analysis with 2H, 3C and Si_3N_4 was also performed, but resulted in <0.1 wt% of the SiC polytypes and >20 wt% Si_3N_4 for most samples, where none of the above were seen in XRD scans. These phases were therefore disregarded. Boron nitride and graphite were not observed in the EBSD scans.

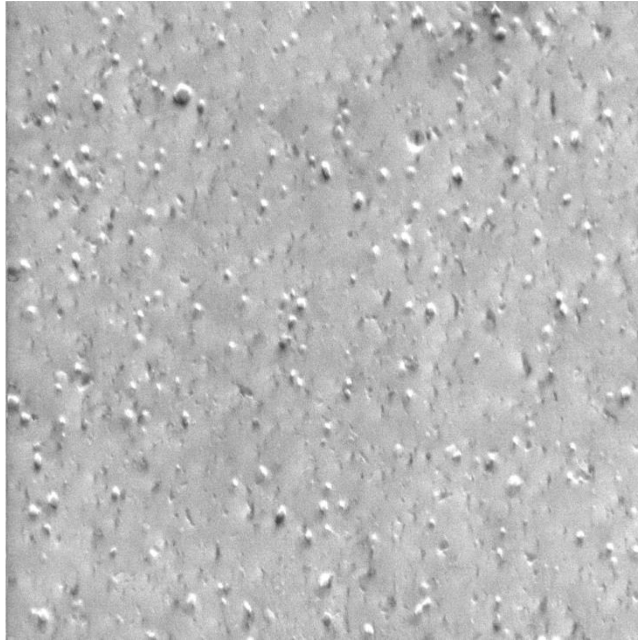

Figure 51. Secondary electron image of the area scanned for ESBD analysis of SiC 0BN 60min.

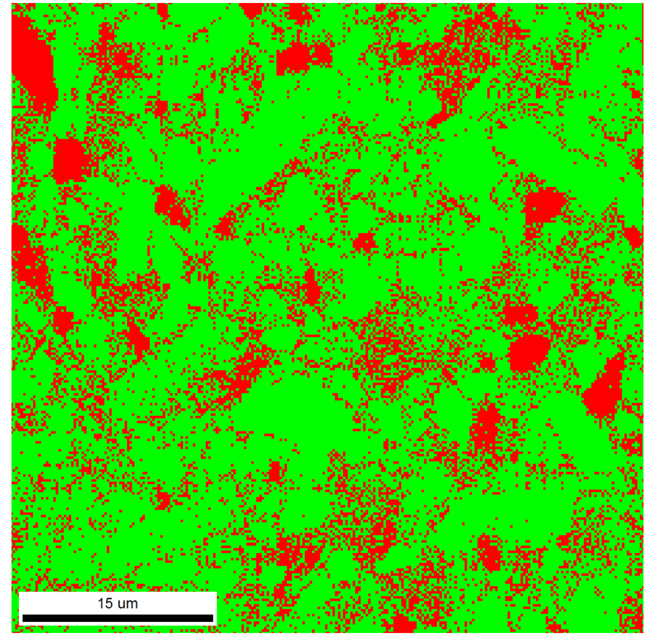

Figure 50. Phase map for the area scanned in Fig. 50, SiC 0BN 60 min

The IPF image is the easiest way to view the SiC grains. The colored triangle on the right in Fig. 52 shows how the color changes with orientation; red is oriented with [0001] direction pointed out-of-plane, while blue and green are oriented in-plane. Crystal defects are seen within most of the grains, and randomly oriented areas are also seen in the image. The defects can be annealed away at 1950 °C for 6 hours [3].

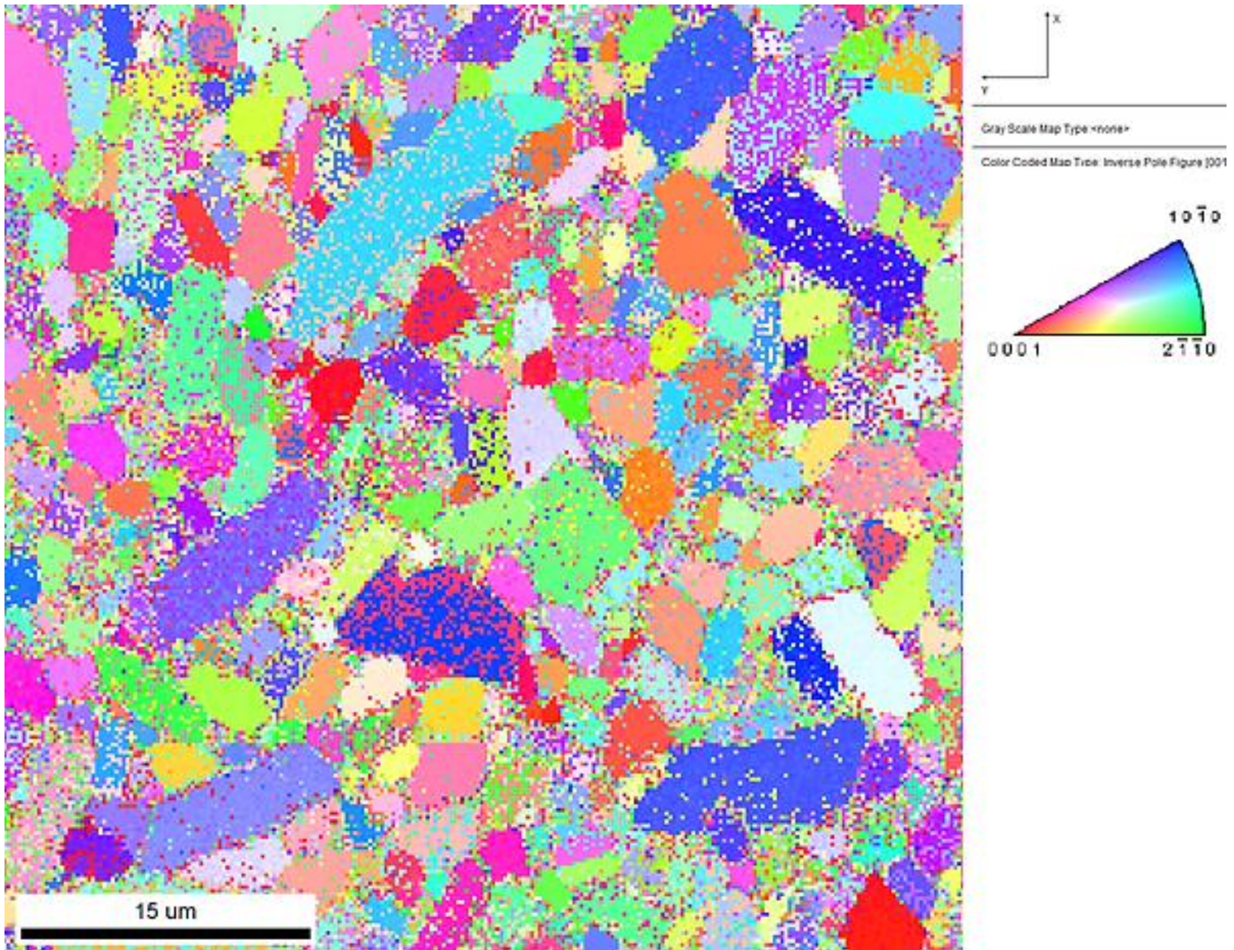

Figure 52. Inverse pole figure for the area scanned in Fig. 50, SiC 0BN 60min.

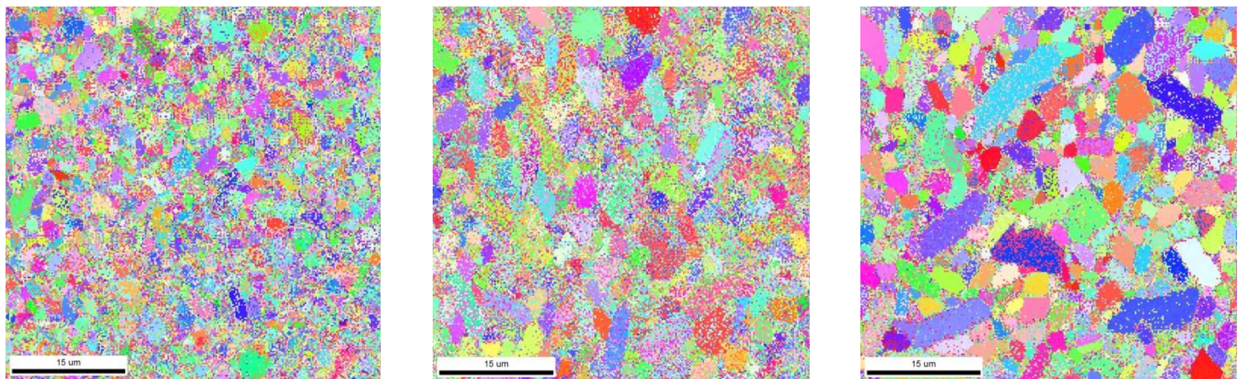

Figure 53. Inverse pole figures of sintered SiC 0BN with 0 (left), 30 (middle) and 60 min (right) holding time. The scale bar is 15 µm.

Fig. 53 shows IPF images for SiC 0BN with increasing holding time. The grain size increased with holding time. There is also some elongation of grains, especially in grains oriented in-plane (blue and green colors). Fig. 54 and 55 show the microstructure evolution for SiC 5BN and SiC 10BN respectively. The grains are smaller and more equiaxed. At 0 minutes, the SiC 10BN grains are large, and seem to recrystallize into smaller grains.

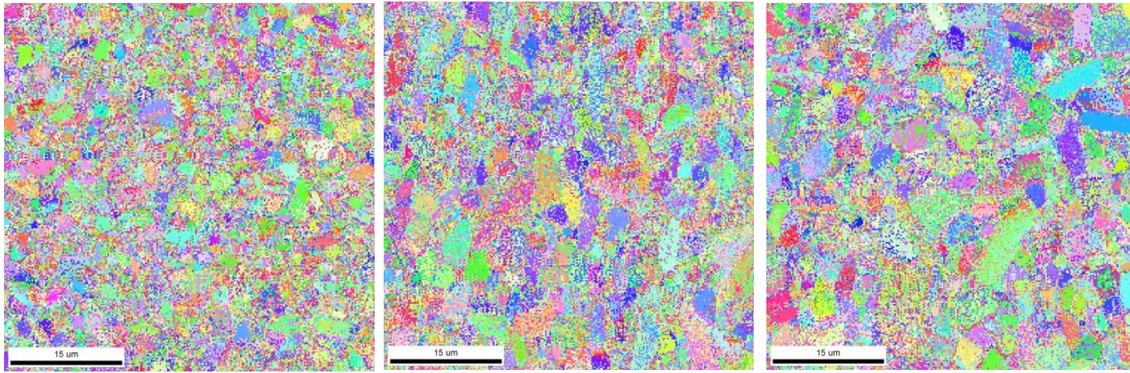

Figure 55. **IPF images of sintered SiC 10BN with 0 (left), 30 (middle) and 60 min (right) holding time. The scale bar is 15 µm.**

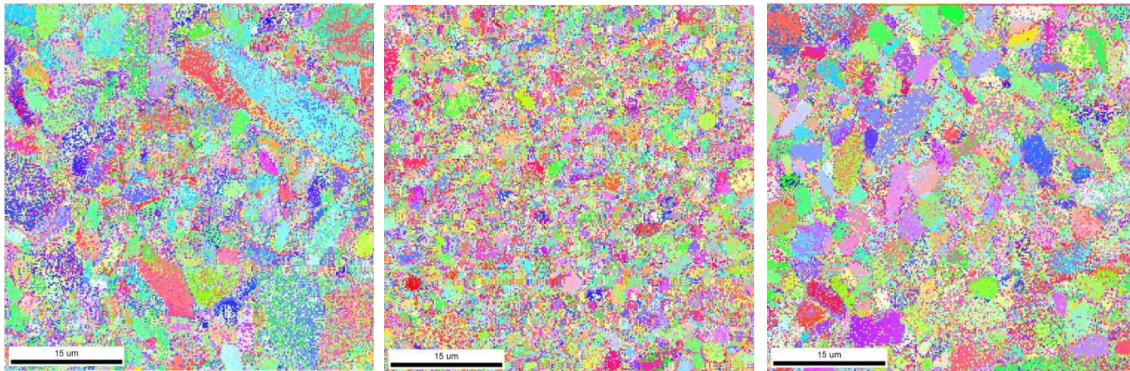

Figure 54. **IPF images of sintered SiC 5BN with 0 (left), 30 (middle) and 60 min (right) holding time. The scale bar is 15 µm.**

Due to the external pressure, the microstructure develops differently normal and parallel to pressing directions. Fig. 56 shows IPF images of SiC 0BN 60min with viewing angle parallel (left) and normal to (right) pressing direction. Even though these images are from the same hot-pressed sample and have undergone the same sample preparation, scanning and indexing parameters, the image viewed parallel to pressing angle (left) has higher quality and more clearly defined grains. There is also less out-of-plane orientations in the right image, seen from less red color.

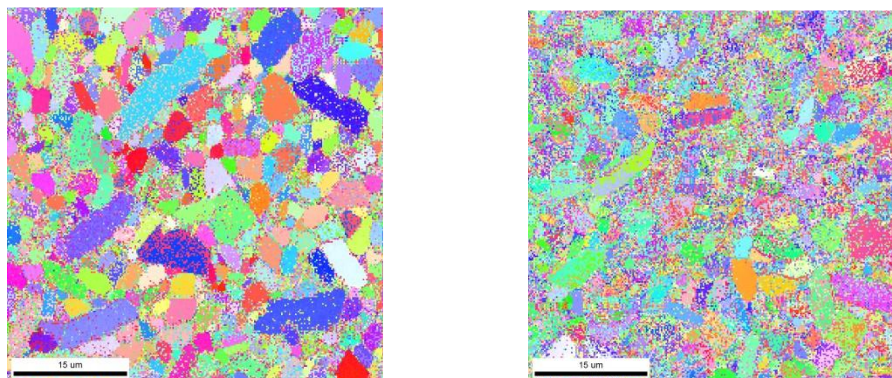

Figure 56. **Inverse pole figures for SiC 0BN sintered at 60 min. Viewing angle is parallel (left) and normal (right) to pressure direction. The scale bar is 15 µm.**

Fig. 57 and 58 show smaller quality differences for BN-samples with changing viewing angles. These images also show more similar color distribution between viewing angles.

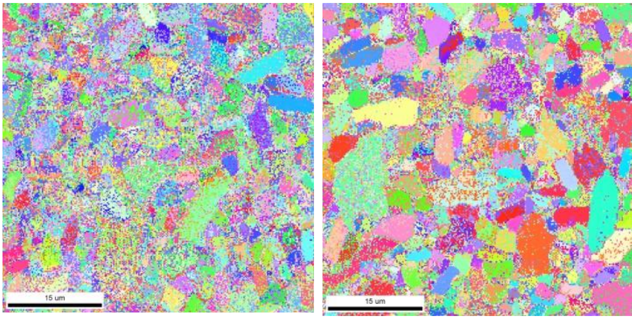

Figure 57. IPF images for SiC 5BN 60 min with viewing angle parallel to (left) and normal to (right) pressing direction. The scale bar is 15 µm.

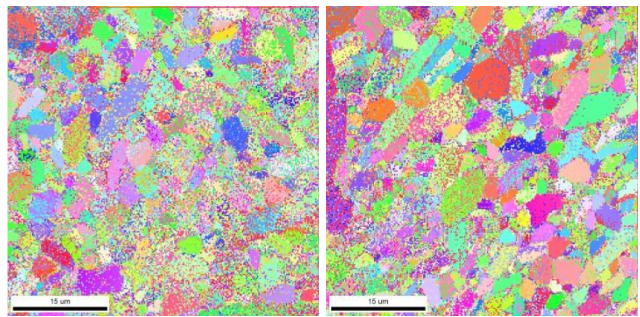

Figure 58. IPF images for SiC 10BN 60 min with viewing angle parallel to (left) and normal to (right) pressing direction. The scale bar is 15 µm.

The 4H/6H ratios for the EBSD scans are shown in Figure 59.

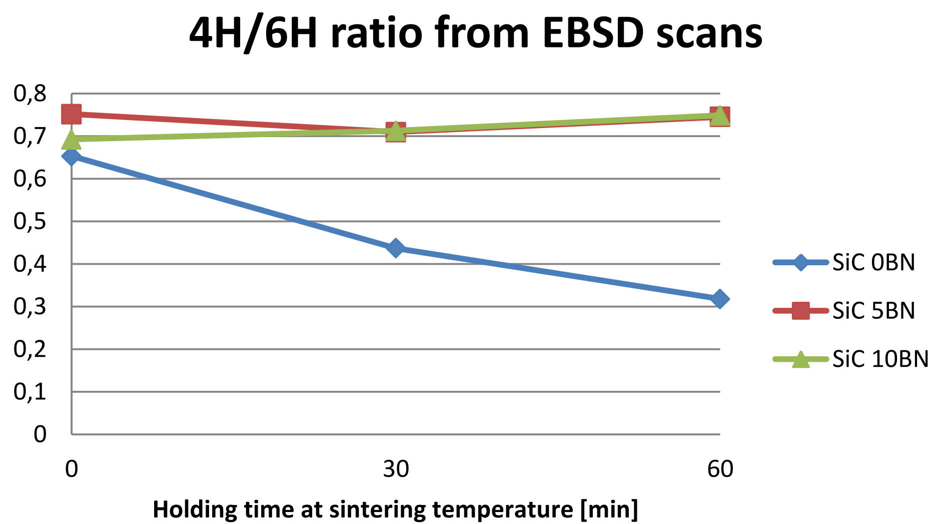

Figure 59. 4H to 6H ratio measured in the EBSD scans. The lines are a guide for the eye.

4.5 Glow discharge optical emission spectroscopy

The GDOES delivers fast depth profile analysis for dense samples. Fig. 60 shows the analysis for SiC 0-10BN sintered for 60 minutes. After an initial surface layer containing oxygen and nitrogen, the detected voltages remain constant until analysis completion. Since the GDOES removes atoms layer by layer, the end-of-measurement depth is of interest, as the time scale in Fig. 60 could be approximated to depth. A profilometer would be used for this, but it was abroad for maintenance. The depth was instead measured in SEM to approximately 30-40 µm for all samples. Due to the uncertainty of these measurements, depth profiling was not used on the graphs.

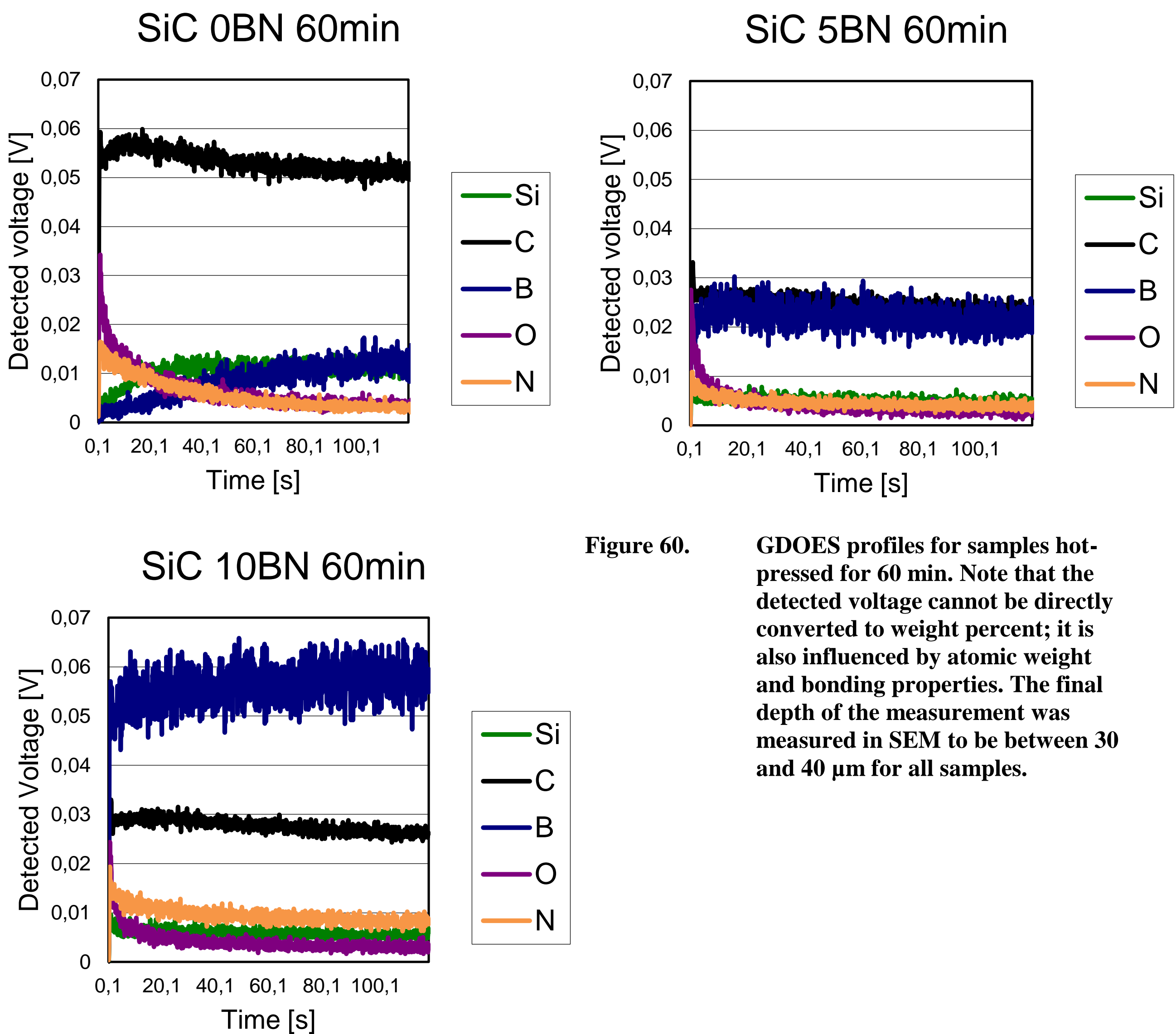

Figure 60. **GDOES profiles for samples hot-pressed for 60 min. Note that the detected voltage cannot be directly converted to weight percent; it is also influenced by atomic weight and bonding properties. The final depth of the measurement was measured in SEM to be between 30 and 40 µm for all samples.**

For ease of comparison, averages for the last 10 seconds of measurement are shown in Fig. 61. For SiC 0BN, longer sintering times slightly reduced the intensity for all elements. The same trend is seen for some of the other samples, but not all. This will be discussed further in section 5.2.

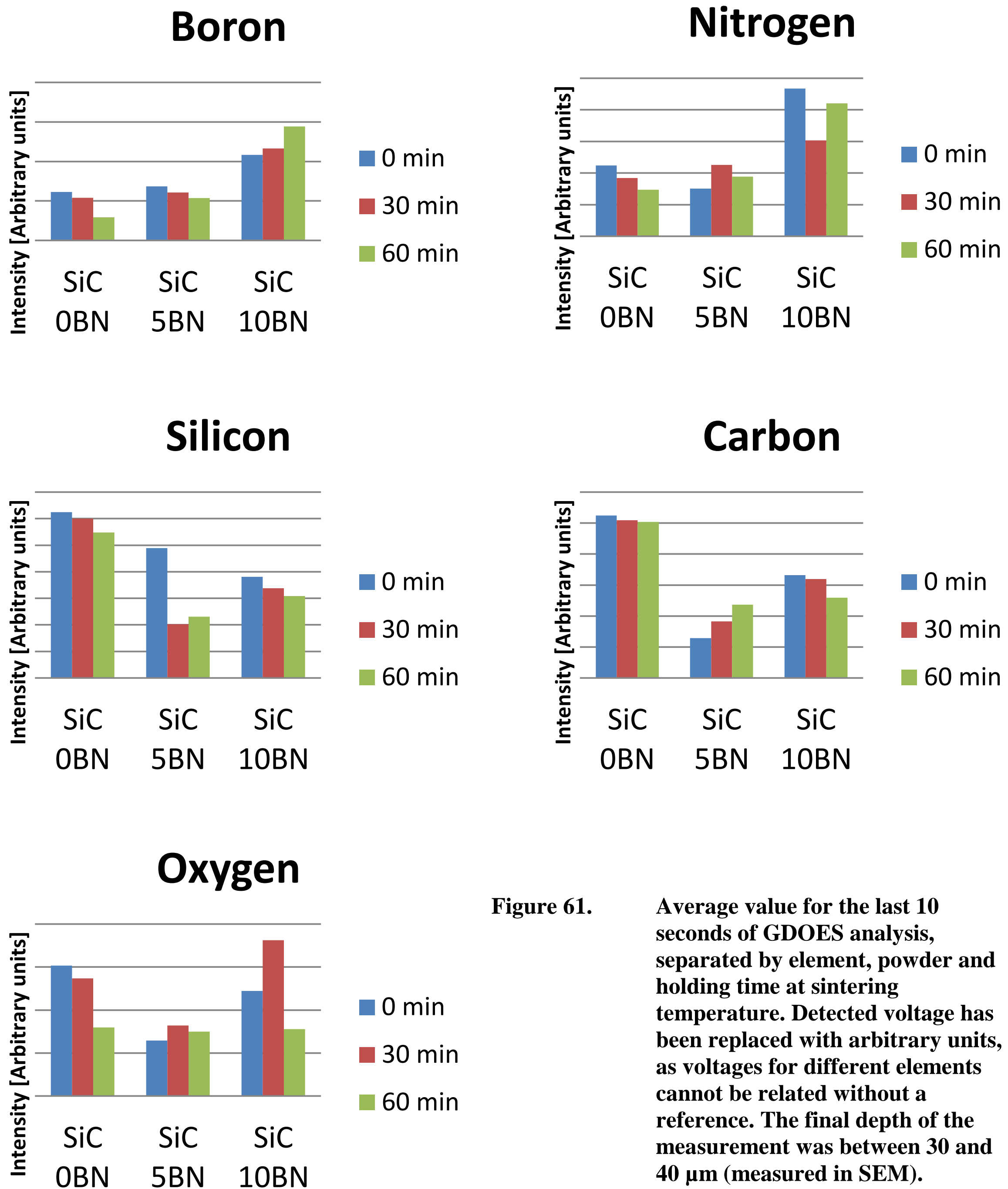

Figure 61. **Average value for the last 10 seconds of GDOES analysis, separated by element, powder and holding time at sintering temperature. Detected voltage has been replaced with arbitrary units, as voltages for different elements cannot be related without a reference. The final depth of the measurement was between 30 and 40 µm (measured in SEM).**

Since the GDOES requires vacuum to function properly, a sample holder was created for use with the porous samples heat-treated at 1600 °C. Vacuum was achieved, but the results from those scans were unreliable and showed elements believed not to exist in the sample or sample holder. This may have been caused by sputtering of the GDOES equipment instead of the sample. The problems were likely caused by the open porosity, which could have resulted in sputtering spread and low sputtering rates. This data has been rejected, and only data from the sintered samples are presented.

5 Discussion

5.1 Densification

SiC 10BN was sintered to >99.9% of theoretical density. Hot-pressing mitigates the low self-sinterability of h-BN, and SiC-BN composites can therefore be sintered to high densities. SiC grains densified until BN and graphite fill the pores. SiC 5BN and 0BN was sintered to 98 and 99% of theoretical density, respectively. The low pressure and temperature at 1600°C was enough to finish the first stage of sintering, particle rearrangement, for SiC 0 and 5BN. The second stage of sintering, neck growth, can therefore occur during heating. SiC 10BN did not finish the initial sintering step before the temperature and pressure increase, but would still densify. Upon reaching the sintering temperature, all powders had >95% density, which indicates that the intermediate sintering stage is completed. The pores have been closed, and only grain growth occurs at 2050°C. This provides the final increase in density. No correlation was found between powder agglomerate size and densification, as expected.

5.2 Composition

The phase diagrams reported by Seifert *et al.* [71] in Figure 23 do not support any reaction between SiC, BN, B4C and C at the given conditions. From the XRD scans in Figure 43, only small changes are seen in peak position and density, and the high stability of SiC and BN result in no appearance of new phases or decomposition. The SiC peaks move only slightly upon boron incorporation, as boron substitutes both Si and C in the matrix. This causes lattice parameters to change less than if it only replaced one of them, see Figure 17 and Figure 46, as well as Appendix H.

The disordered and turbostratic nature of the BN structure, as well as its partial overlapping with graphite, made it difficult for the Topas software to calculate how much of the peak is BN and how much is graphite. Weight percent calculations have therefore been foregone and visual inspection of the XRD scans was deemed sufficient to confirm minimal change in composition. The d-spacing of their peaks were measured instead, and are shown in Figure 48.

Heating to 1600 °C, the d-spacing for BN goes down for both SiC 5BN and 10BN. Ordering of the turbostratic layers due to the applied pressure and heat seem probable. During the holding time at 1600 °C, d-spacing continues to decrease for 5BN, while remains constant for 10BN. Upon reaching 2050 °C, the d-spacing for 5BN has stabilized around the same value upon reaching 1600°C. For 10BN, the transition from 1600 to 2050 °C has decreased the d-spacing by a significant amount; a tighter packing. This could be caused by stacking of graphite and BN layers, due to their plate-like structure (see Figure 8). The BNC_x regions described for Si-B-C-N polymers in section 2.5 seem probable, as the graphite peaks also increase in d-spacing for SiC 10BN, until they have the same spacing as graphite in 5BN. A dense BNC_x-structure is formed for SiC 10BN in the region 1600-2050 °C, and subsequently expands with holding at 2050 °C.

The formation of dense BNCx regions should affect the GDOES measurements. Carbon measurements from Figure 61 are reprinted in Figure 62.

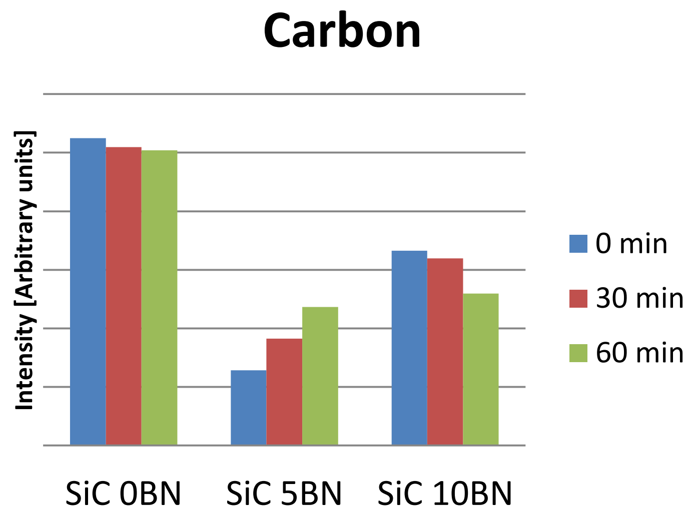

Figure 62. **GDOES measurements for carbon, reprinted from Figure 61. The intensities are average values for the last 10 seconds of each measurement.**

GDOES intensities are not only affected by composition, but also bonding strength, as mentioned in section 2.6. SiC and BN have very strong, covalent bonds. Elements from these compounds are therefore not expected to contribute much for GDOES intensities, as can be seen in the minimal differences in intensity for boron and nitrogen between SiC 0BN and 5BN in Figure 61. The added carbon black in SiC 0BN graphitize [66], and therefore contribute more to carbon intensity than the carbon bound in SiC. For SiC 5BN, the carbon black can be incorporated in a BNC_x structure, which presumably is more resistant to sputtering than graphite, as every other layer consists of h-BN with strong, covalent bonds. This is a reasonable explanation for the lower carbon intensities for SiC 5 and 10BN, even though the total carbon content is roughly the same.

SiC 5 and 10BN have different GDOES trends during holding at sintering temperature; SiC 5BN shows increasing intensity with holding time, while SiC 10BN shows declining intensity. Bill *et al.* [73] calculated and measured that the optimal ratio of B:N:C in BNC_x structures are 1:1:3.3. Since carbon black additions is of a much smaller amount than BN in SiC-5 and 10BN, a boron-carbon exchange mechanism is suggested for the SiC-BN interface:

Boron can substitute both Si and C in SiC [53]. Free Si in the structure is not stable at high temperatures, and will react with boron and carbon to form SiB_4 and SiC, where the latter is much more stable. Substituted Si is therefore presumed to return to a silicon carbide structure. Substituted carbon, on the other hand, also has a stable configuration in the BNC_x structure. Since boron will substitute both, it is therefore possible that high amounts of BN additions result in carbon depletion of the SiC matrix, as the BNC_x regions act as carbon sinks. Some of the C-sites in SiC will therefore contain boron, yet the low solubility of boron in SiC may cause a high amount of C-site vacancies. Vacancies are highly beneficial in sintering, as they increase the diffusivity of the material (see section 2.3.2).

The increase in carbon intensity with sintering time for SiC 5BN may therefore occur due to an increase in total carbon in the BNC_x regions. The driving force for such a mechanism will be much higher with higher BN additions, and may have already reached equilibrium for SiC 10BN at 0 min holding time. As the sintering time increases, grains grow and stabilize, causing the same decline in intensity as seen for SiC 0BN with increasing holding time. This is supported by the increase in d-spacing for BN in SiC 10BN in Figure 48.

The GDOES profiles in Figure 60 show high stability after an initial surface layer. This indicates a high degree of homogeneity for all samples.

5.3 Microstructure

For the powders containing BN, grains are less defined, and have smaller grains than the powder without. Boron inhibits grain growth in SiC, and since the BN additions are in excess of the solubility limit, BN and BNC_x regions separate SiC grains. These increased diffusion distances slowed down grain growth, and is in agreement with the theory presented in 2.4.1.

Growth of SiC grains are preferred in the [0001] directions [10]. This causes elongation of SiC grains with increasing grain growth. In hot-pressing, grain growth is preferred in directions normal to the pressing directions, due to the grain flattening effect presented in 2.3.1. Combined, grains oriented with [0001] directions normal to the pressing direction have a much higher driving force for grain growth than other orientations. This is seen in Figure 56, where blue grains, which have this orientation, have become elongated. This leads to a higher volume fraction of (0001) planes analyzed by the EBSD for the surface viewed normal to the pressing direction. It is particularly difficult for the EBSD software to discern between 6H and 4H structures in this direction, as they are identical in the two first layers (ABCB'A'C' vs. ABA'C'). This causes the much lower quality of the image viewed normal to the pressing direction.

The powders containing BN not only showed less grain growth, but also less elongation; the preferential growth of grains oriented with [0001] directions normal to the applied pressure is restricted. The IPF images with different viewing angles (Figure 58 and Figure 57) are therefore more similar in quality and color distribution for SiC 5 and 10BN. This will lead to different structural properties for the SiC powders sintered with and without BN:

With more equiaxed grains, the fracture toughness will decrease, but the properties will be more isotropic (similar in all directions). Smaller grains will also result in increased toughness. Although the BNCx regions may have higher strength than graphite regions in SiC 0BN, the large amounts of addition will probably reduce the strength of the ceramic as a whole; the BNC_x pockets can be viewed as "defects" in the matrix, with crack-inducing properties. The mechanical properties of SiC-5BN and SiC-10BN should therefore be investigated.

The microstructure of SiC 10BN 0min (left in Figure 55) is interesting. Although the pressure is relieved immediately upon reaching sintering temperature, there are signs of exaggerated

grain growth. These grains do not seem to be stable at the sintering temperature, as SiC 10BN 30min, and even SiC 10BN 60min, show much smaller grains. There is also no evidence of a reaction in the XRD scans. The presence of large amounts of BN could initiate densification at lower temperatures, but BN usually separates grains and lower grain growth. One possible explanation is the previously presented boron-carbon exchange mechanism, where boron substitutions cause carbon to move from the SiC structure to BNC_x regions. The preferred B:N:C ratio in this layer has been calculated and experimentally measured to be 1:1:3.3 by Bill *et al.* [73]. With 10 wt% added BN, there is therefore a large carbon deficiency in the BNC_x regions, and consequently a high driving force for boron-carbon exchange with the SiC structure. If this facilitates a dissolution-precipitation mechanism for Si and C, similar to the vapor transport mechanism presented in 2.3.3, coarsening and exaggerated grain growth is not unlikely. The consequent breakdown of the large grains with longer holding times at 2050°C can be caused by the high driving force for sintering at this temperature and pressure. Since the densification is not complete, recrystallization occurs to achieve the final density. It is suggested that the microstructural development of SiC 10BN should be further studied in the region 1600-2050°C.

The secondary electron images of EBSD surfaces in Appendix F show a dense structure, with some particles sticking out. Although the EBSD scans report this structure as SiC, it may be boron carbide particles. Since B_4C is harder than SiC, it will not be preferentially sputtered like h-BN and graphite. T. Bergh [66] reported B_4C particles in the μm-range for hot-pressed SiC 0BN, and it is therefore unlikely that the B_4C particles were small enough for the SiC diffraction pattern to be visible through B_4C particles. All points in the EBSD samples were still indexed as either 4H or 6H SiC, so the B_4C particles may have been removed by the sample preparation after all. The resulting topography can also be due to different sputtering rates for different SiC orientations.

Entering Si_3N_4 as a possible structure results in over 20 wt% of it in EBSD scans, an amount clearly not seen in XRD scans. Entering it does not increase the average certainty of the EBSD analysis (confidence index), and small changes to indexing parameters result in different grains being identified as Si_3N_4. The possibility of large Si_3N_4 amounts has therefore been ruled out. 2H and 3C polytypes were also searched for in EBSD, but less than 1 wt% was found. There are however, large discrepancies between the relative amounts of 4H and 6H reported from XRD (Fig. 49) and EBSD (Fig. 59). As mentioned above, this could be caused by the difficulty EBSD has discerning between the [0001] directions for 6H and 4H (ABCB'A'C' vs. ABA'C'). The Rietveld analysis from XRD in Fig. 49 is therefore a much more reliable resource, and matches better with results reported by i.e. Kistler-De Coppi [25]. The relative increase in 4H is also expected for all powders, since boron additions promote 4H formation. The transformation is slower than reported for pressureless annealing at 2150°C [25].

6 Conclusions and further work

Commercial SiC-powders with 5 and 10 wt% added boron nitride were hot-pressed to high densities (>99.9%). Although other authors have reported poor sinterability for this type of composite, external pressure is able to mitigate the low self-sinterability of boron nitride. Density, microstructural and compositional development have been presented *ex situ*. Grain growth was restrained, and x-ray diffraction showed no other phases or compounds than BN and graphite with the additions. The samples should be subjected to mechanical testing, where pockets of boron nitride are believed to lubricate and reduce friction, even under demanding conditions. A pin-on-disk test simulating possible operating conditions is recommended (SiC on SiC-BN, SiC-BN on SiC-BN and steel on SiC-BN).The BN-pockets might lower structural strength, and bending tests should also be performed.

The microstructure of the sample containing the highest amount of boron nitride showed signs of exaggerated grain growth upon reaching the sintering temperature, with consequent recrystallization. A boron-carbon exchange mechanism between SiC and BN is proposed. This mechanism is believed to assist in vacancy formation, increasing sinterability. GDOES measurements and XRD scans support the existence of BNC_x regions in SiC 5 and 10BN samples at sintering temperatures.

References

1. Böcker, W.D.G., et al., *Covalent High-Performance Ceramics.* Advanced Materials, 1992. **4**(3): p. 169-178.
2. Prochazka, S. and R.M. Scanlan, *Effect of boron and carbon on sintering of SiC.* Journal of the American Ceramic Society, 1975. **58**(1-2): p. 72.
3. Li, Y., et al., *Microstructure, Thermal Conductivity, and Electrical Properties of In Situ Pressureless Densified SiC–BN Composites.* Journal of the American Ceramic Society, 2015. **98**(3): p. 879-887.
4. Duan, X., et al., *Effect of sintering pressure on the texture of hot-press sintered hexagonal boron nitride composite ceramics.* Scripta Materialia, 2013. **68**(2): p. 104-107.
5. Tong, X.C., *Thermally Conductive Ceramic Matrix Composites*, in *Advanced Materials for Thermal Management of Electronic Packaging*. 2011, Springer New York: New York, NY. p. 277-304.
6. Berzelius, J.J., *Untersuchungen über die Flussspathsäure und deren merkwürdigsten Verbindungen.* Annalen der Physik, 1824. **77**(6): p. 169-230.
7. Cowles, E.H., *Electric smelting-furnace*. 1885, Google Patents.
8. Acheson, E.G., *Production of artificial crystalline carbonaceous materials, carborundum.*, E.P. 17911, Editor. 1892.
9. WashingtonMills. *Carborex Silicon Carbide*. 2016 08. May. 2016]; Available from: http://www.washingtonmills.no/products.
10. Motzfeldt, K., *Silicon carbide : synthesis, structure and sintering*. SINTEF rapport (SINTEF. Avdeling for metallurgi : trykt utg.). Vol. STF34 S93001. 1993, Trondheim: SINTEF, Metallurgy.
11. Moissan, H., *Nouvelles recherches sur la meteorite de Canon Diablo.* Comptes Rendus Hebdomadaires des Seances de l'Academie des Sciences, 1904: p. 773-780.
12. *Properties of Silicon Carbide*. 1995: Institution of Engineering and Technology.
13. *Properties of Silicon Carbide*. 2006 08. May 2016]; Available from: http://www.ioffe.ru/SVA/NSM/Semicond/SiC/basic.html.
14. Abderrazak, H. and E.S.B.H. Hmida, *Silicon Carbide: Synthesis and Properties*, in *Properties and Applications of Silicon Carbide*, R. Gerhardt, Editor. 2011, InTech.
15. Tairov, Y.M. and V.F. Tsvetkov, *Progress in controlling the growth of polytypic crystals.* Progress In Crystal Growth And Characterization, 1983. **7**(1): p. 111-162.
16. Jepps, N.W. and T.F. Page, *Polytypic transformations in silicon carbide.* Progress In Crystal Growth And Characterization, 1983. **7**(1): p. 259-307.
17. Page, T. and T. Page, *Silicon carbide: structure and polytypic transformations.* NATO ASI Series, Series E: Applied Sciences, 185pp, 1990. **197-214**.
18. Ravikumar, Y.S. and K.S. Gurumurthy, *Silicon Carbide Material with Power Electronic Control Devices.* International Journal of Computer Science and Network Security, 2012. **11**(12): p. 142-150.
19. Chase, M.W., C.A. Davies, and J.R. Downey, *JANAF thermochemical tables.* Journal of Physical and Chemical Reference Data, 1985. **14**: p. 1856.
20. Knippenberg, W.F. and L. Rijksuniversiteit Te, *Growth phenomena in silicon carbide*. 1963, Echt, Valkenburg: Echt.
21. Shaffer, P.T.B., *BETA SILICON CARBIDE*. 1969: Elsevier Inc. S97-S105.
22. Jepps, N., T. Page, and N. Jepps, *THE 6H-3C 'REVERSE' TRANSFORMATION IN SILICON CARBIDE COMPACTS.* J.AM.CERAM.SOC. J. Am. Ceram. Soc, 1981. **64**(12): p. C-177.
23. Heine, V., C. Cheng, and R.J. Needs, *The Preference of Silicon Carbide for Growth in the Metastable Cubic Form.* Journal of the American Ceramic Society, 1991. **74**(10): p. 2630-2633.
24. Ostwald, W., *Studien über die Bildung und Umwandlung fester Körper: 1 Abhandlung Übersättigung and Überkaltung.* Zeitschrift für Physikalische Chemie, 1897. **22**: p. 289-330.
25. Kistler-De Coppi, P.A. and W. Richarz, *Phase transformation and grain growth in silicon carbide powders.* International Journal of High Technology Ceramics, 1986. **2**(2): p. 99-113.

26. Wecht, E.H.P., *Feuerfest-Siliciumcarbid*. Applied mineralogy. Vol. 11. 1977, Wien und N.Y: Springer.
27. Mehrwald, E.H., *Entwicklung und wirtschaftliche Aspekte der technischen SiC-Herstellung.* German Ceramic Society Report, 1992. **69**: p. 72-81.
28. Miller, P.D., J.G. Lee, and I.B. Cutler, *The Reduction of Silica with Carbon and Silicon Carbide.* Journal of the American Ceramic Society, 1979. **62**(3-4): p. 147-149.
29. Motzfeldt, K., *Oxides plus carbon*. 1988, Trondheim: Norges tekniske høgskole, Division of Metallurgy.
30. Wiik, K., *Kinetics of reactions between silica and carbon*. 1990, Institutt for uorganisk kjemi, Norges tekniske høgskole: Trondheim.
31. Tone, F.J., *High Temperature Products of Silicon.* Industrial & Engineering Chemistry, 1931. **23**(11): p. 1312-1316.
32. Lipp, A., K. Schwetz, and K. Hunold, *Hexagonal boron nitride: fabrication, properties and applications.* Journal of the European Ceramic Society, 1989. **5**: p. 3-9.
33. Balmain, W.H., *Bemerkungen über die Bildung von Verbindungen des Bors und Siliciums mit Stickstoff und gewissen Metallen.* Journal für Praktische Chemie, 1842. **27**(1): p. 422-430.
34. German, R.M., *Chapter Four - Measurement Tools and Experimental Observation*, in *Sintering: from Empirical Observations to Scientific Principles*. 2014, Butterworth-Heinemann.
35. Rahaman, M.N., *Ceramic processing and sintering*. Materials engineering. Vol. 10. 1995, New York: Marcel Dekker.
36. Dorozhkin, S., *Calcium Orthophosphate-Based Bioceramics.* Materials, 2013. **6**(9): p. 3840.
37. Barsoum, M.W., *Fundamentals of ceramics [electronic resource].* [Rev. ed.]. ed, ed. I. NetLibrary. 2003: Bristol, UK.
38. Abavare, E.K.K., et al., *Surface energy of Si(110)- and 3C-SiC(111)-terminated surfaces.* physica status solidi (b), 2014. **251**(7): p. 1408-1415.
39. Margiotta, J.C., *Study of silicon carbide formation by liquid silicon infiltration of porous carbon structures*. 2009, The Johns Hopkins University: ProQuest Dissertation and Theses. p. 166.
40. Yamamoto, T., et al., *Consolidation of Nanostructured β-SiC by Spark Plasma Sintering.* Journal of the American Ceramic Society, 2004. **87**(8): p. 1436-1441.
41. Nadeau, J.S., *Very high pressure hot pressing of silicon carbide.* Journal of the American Ceramic Society, 1973. **52**: p. 170-174.
42. Maddrell, E. and E. Maddrell, *Pressureless sintering of silicon carbide.* Journal of Materials Science Letters, 1987. **6**: p. 486-488.
43. Coble, R.L., *Sintering Crystalline Solids. I. Intermediate and Final State Diffusion Models.* Journal of Applied Physics, 1961. **32**(5): p. 787-792.
44. Barsoum, M.W., *Fundamentals of ceramics*. McGraw-Hill series in materials science and engineering. 1997, New York: McGraw-Hill.
45. Ghoshtagore, R.N. and R.L. Coble, *Self-Diffusion in Silicon Carbide.* Physical Review, 1966. **143**(2): p. 623-626.
46. Uemura, Y., Y. Inomata, and Z. Inoue, *A grain boundary of α-SiC bicrystals.* Journal of the Ceramic Society of Japan, 1982. **90**(9): p. 527-531.
47. Maddrell, E., *Pressureless sintering of silicon carbide.* Journal of Materials Science Letters, 1987. **6**(4): p. 486-488.
48. Greskovich, C. and J.H. Rosolowski, *Sintering of Covalent Solids.* Journal of the American Ceramic Society, 1976. **59**(7-8): p. 336-343.
49. Lange, F.F. and T.K. Gupta, *Sintering of SiC with Boron Compounds.* Journal of the American Ceramic Society, 1976. **59**: p. 537-538.
50. Rühle, M. and G. Petzow, *Microstructure and Chemical Composition of Grain Boundaries in Ceramics*, in *Surfaces and Interfaces in Ceramic and Ceramic — Metal Systems*, J. Pask and A. Evans, Editors. 1981, Springer US. p. 167-175.
51. Ogbuji, L.U., *Grain Boundaries in Carbon- and Boron-Densified SiC: Examination by High Resolution Transmission Electron Microscopy*, in *Surfaces and Interfaces in Ceramic and Ceramic — Metal Systems*, J. Pask and A. Evans, Editors. 1981, Springer US. p. 713-723.

52. Hamminger, R., G. Grathwohl, and F. Thümmler, *Microanalytical investigation of sintered SiC.* Journal of Materials Science, 1983. **18**(10): p. 3154-3160.
53. Tajima, Y. and W.D. Kingery, *Solid Solubility of Aluminium and Boron in Silicon Carbide.* Journal of the American Ceramic Society, 1982. **65**: p. C-27-C-29.
54. Murata, Y. and H. Smoak, *Densification of Silicon Carbide by the Addition of BN, BP and B4C, and Correlation to their Solid Solubilities*, in *Proceedings of the International Symposium of Factors in Densification and Sintering of Oxide and non-Oxide Ceramics*, S. Somiya and S. Saito, Editors. 1978, Association of Science Document Information: Hakone, Japan. p. 382-399.
55. Mizrah, T., M. Hoffman, and L.J. Gauckler, *Pressureless sintering of silicon carbide*, in *Ceramic Materials and Components for Engines*, H. Hausner, Editor. 1986, Deutsche Keramische Gesellschaft. p. 347-352.
56. Clegg, W.J., *Role of carbon in the sintering of boron-doped silicon carbide.* Journal of the American Ceramic Society, 2000. **83**(5): p. 1039-1043.
57. Rijswijk, W. and D. Shanefield, *Effect of carbon as a sintering aid in silicon carbide.* Journal of the American Ceramic Society, 1990. **73**(1): p. 148-149.
58. Lilov, S.K., *Thermodynamic analysis of phase transformations at the dissociative evaporation of silicon carbide polytypes.* Diamond and Related Materials, 1995. **4**: p. 1331-1334.
59. Pultz, W.W. and W. Hertl, *SiO_2+SiC reaction at elevated temperatures.* Transactions of the Faraday Society, 1966. **62**(9): p. 2499-2504.
60. Miller, P.D., J.G. Lee, and I.B. Cutler, *The reduction of silica with carbon and silicon carbide.* Journal of the American Ceramic Society, 1979. **62**(3-4): p. 147-149.
61. Drowart, J. and G. De Maria, *Thermodynamic study of the binary system carbon-silicon using a mass spectrometer*, in *Silicon Carbide a High Temperature Semiconductor*, J.R. O'Connor and J. Smiltens, Editors. 1960, Pergamon Press: London. p. 16-23.
62. Gubernat, A., *The Role of Boron and Carbon in Sintering of Silicon Carbide*, in *University of Mining and Metallurgy*. 2001: Cracow.
63. Stobierski, L. and A. Gubernat, *Sintering aids in silicon carbide densifications.* Bulletin of the Polish Academy of Sciences, 1999. **47**(4): p. 411-421.
64. Suzuki, H. and T. Hase, *Boron transport and charge of lattice parameter during sintering of ß-SiC.* Journal of the American Ceramic Society, 1980. **63**(5-6): p. 349-350.
65. Stobierski, L. and A. Gubernat, *Sintering of silicon carbide. Effect of carbon.* Ceramics International, 2003. **29**(3).
66. Bergh, T., *TEM Characterization of Hot-Pressed Silicon Carbide with Carbon and Boron Additives.* SCANDEM poster, 2015.
67. Zangvil, A. and R. Ruh, *Solid Solutions and Composites in the SiC-AlN and SiC-BN Systems.* Materials Science and Engineering, 1985. **71**(0): p. 159-164.
68. Schmidt, H., *Si-(B-)C-N Ceramics Derived from Preceramic Polymers: Stability and Nano-Composite Formation.* Soft Materials, 2007. **4**(2-4): p. 143-164.
69. Seifert, H., H.L. Lukas, and F. Aldinger, *Development of Si-B-C-N ceramics supported by phase diagrams and thermochemistry.* Ber. Bunsen-Ges. Phys. Chem. Chem. Phys., 1998. **102**(9): p. 1309-1313.
70. Tavakoli, A.H., et al., *Effect of boron on the thermodynamic stability of amorphous polymer-derived Si(B)CN ceramics.* Acta Materialia, 2012. **60**(11): p. 4514-4522.
71. Seifert, H.J., et al., *Phase equilibria of precursor-derived Si–(B–)C–N ceramics.* Applied Organometallic Chemistry, 2001. **15**(10): p. 794-808.
72. Jalowiecki, A., et al., *Interface characterization of nanosized B-doped Si3N4/SiC ceramics.* Composites Part A, 1996. **27**(9): p. 717-721.
73. Bill, J., et al., *Precursor-derived Si–(B–)C–N ceramics: thermolysis, amorphous state and crystallization.* Applied Organometallic Chemistry, 2001. **15**(10): p. 777-793.
74. Golczewski, J.A. and F. Aldinger, *Phase separation in Si–(B)–C–N polymer-derived ceramics.* Zeitschrift für Metallkunde, 2006. **97**(2): p. 114-118.
75. Friess, M., et al., *Crystallization of Polymer-Derived Silicon Carbonitride at 1873 K under Nitrogen Overpressure.* Journal of the American Ceramic Society, 2002. **85**(10): p. 2587-2589.

76. *Theory*, in *Glow Discharge Optical Emission Spectroscopy: A Practical Guide*, T. Nelis, R. Payling, and N.W. Barneet, Editors. 2003, The Royal Society of Chemistry. p. 147-177.
77. *Calibration for compositional depth profiling*, in *Glow Discharge Optical Emission Spectroscopy: A Practical Guide*, T. Nelis, R. Payling, and N.W. Barneet, Editors. 2003, The Royal Society of Chemistry. p. 82-102.
78. Smentkowski, V.S., *Trends in sputtering.* Progress in Surface Science, 2000. **64**(1): p. 1-58.
79. Jurac, S., R.E. Johnson, and B. Donn, *Monte carlo calculations of the sputtering of grains: enhanced sputtering of small grains.* The Astrophysical Journal, 1998. **503**(1): p. 247-252.
80. Maitland, T. and S. Sitzman, *Backscattering Detector and EBSD in Nanomaterials Characterization*, in *Scanning Microscopy for Nanotechnology: Techniques and Applications*, W. Zhou and Z.L. Wang, Editors. 2007, Springer New York: New York, NY. p. 41-75.
81. Maitland, T., *EBSD - Current Achievements in Speed and Resolution.* Microscopy and Microanalysis, 2004. **08**(10): p. 936-937.
82. G.F.S, *Diffraction of cathode rays by mica.* Journal of the Franklin Institute, 1929. **207**(6): p. 871-872.
83. Maitland, T., *Electron Backscattered Diffraction.* Advanced Materials & Processes, 2004(May): p. 34-36.
84. Mogstad, K., *Investigation of the sintering properties of commercial SiC-powders*, K. Wiik, Editor. 2015, NTNU: Trondheim.
85. Aylward, G. and T. Findlay, *SI Chemical Data*. 6 ed. 2008, Milton: John Wiley & Sons Australia, Ltd.

Appendix contents

Appendix A – Product specification for the SiC powder before spray drying

Appendix B – Datasheet for spray dried SiC

Appendix C – Density measurements

Appendix D – Stacked XRD scans

Appendix E – All EBSD figures

Appendix F – Secondary electron images of EBSD surfaces with scanned area highlighted

Appendix G – Weight percent to atomic percent calculations

Appendix H – Lattice parameter and d-spacing measurements

7 Appendix A – Product specification for the SiC powder before spray drying

PRODUCT SPECIFICATION

TECHNICAL PRODUCTS	
STANDARD SPECIFICATION	TQS No. 8
Product: SIKA Sintex15C	Item Code 876801240620

Particle Size Distribution

Ds90% µm	Ds50% µm	Ds10% µm
1.5 max	0.40-0.60	0.15 - 0.28

Measured by SediGraph

Specific surface area: 14.0-16.0 m^2/g

Chemistry:

Free C % max.	Free Si % max.	Total oxygen % max.	Fe % max.	Al % max.	Ti %max
0.25	0.15	0,85	0,02	Reported	Reported

Measured according to ANSI B74. 15 Based on Leco Based on XRF

Packaging: 25 kg cardboard boxes with tied plastic liner.

Marking: Product designation and batch No on each box.

Reporting: Certificate of Analysis on physical and chemical data with every batch

Prepared sales Øystein Syrdal	Prepared production REB	Approved quality Sverre Eikenes	Date: 19.04.2013 Version: 1

Figure 63. Product specification for SiC powder used before spray drying. Delivered by Development Engineer Benoit Watremetz at Saint-Gobain Ceramic Materials AS Lillesand.

8 Appendix B – Datasheet for spray dried SiC

This is the datasheet for Sika Densitec 13H, a ready-to-press (RTP) powder delivered by Saint-Gobain that is similar to SiC-0BN, the only difference is a lower specific surface area (13 instead of 15m^2/g).

SIKA® DENSITEC 13H

Silicon Carbide Ready-To-Press granules for solid-state (SSiC) hot-pressed technical ceramics.

DENSITEC 13H granules are spray dried granules, bases on our standard black SINTEX 13C. The premix is doped with sintering additives, low content of temporary binder and pressing aids and is ready to be pressed.
DENSITEC 13 is suitable for dry pressing, uniaxial and isostatic.

Composition

	Sintering additives		Binder content (total organic)	Moisture content	SiC type
	Carbon	Boron	%	%	balance
DENSITEC 13H	Carbon black	Boron Carbide	approx. 2,0	approx. 0,6	SINTEX 13 C

Typical physical properties of green material

	Size		Bulk Density	Flow. Hall	Appearance
	max	Average		Sec / 25g	
Densitec 13H	250	100	0.88	60	Dark color

Typical Properties of sintered parts

	Density	Microhardness HV 1000	Indentation fracture toughness, Kic	Linear shrinkage	Bending strength
	g/cm³	GPa	MPa m$^{1/2}$	%	4 point MPa
DENSITEC 13H	3,19	25	3,5	approx. ~18	550

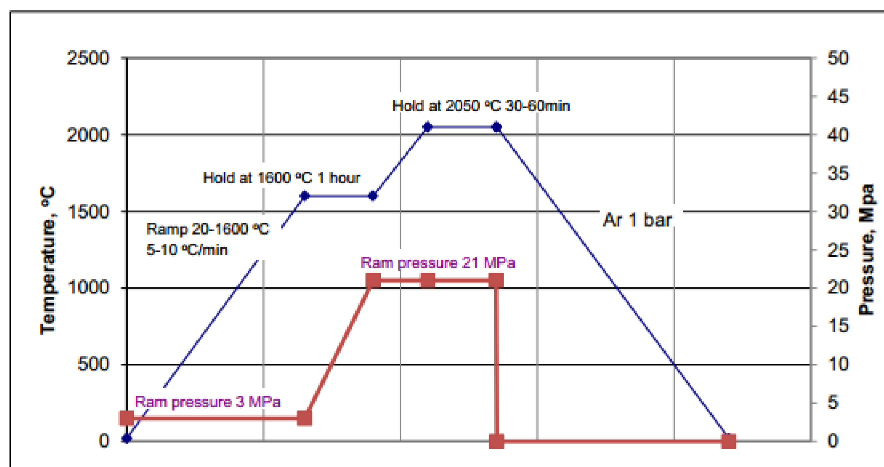

Figure 64. Datasheet for Densitec 13H, a ready-to-press (RTP) powder produced by Saint-Gobain. Delivered by Development Engineer Benoit Watremetz at Saint-Gobain Ceramic Materials AS Lillesand.

9 Appendix C – Density measurements

Table 8. Densities of samples heat-treated at 1600°C with different holding times, measured using Archimedes' principle in water.

Powder	Pressure [MPa]	Holding time at 1600°C [min]	Measured density [g/cm^3]	Theoretical density [g/cm^3]	Percent theoretical density [%]
SiC-0BN	4.3	0	1.956	3.21	61.1
	4.3	30	1.929	3.21	60.1
	4.3	60	1.990	3.21	62.0
SiC-5BN	4.3	0	1.917	3.15	61.0
	4.3	30	1.962	3.15	62.2
	4.3	60	1.988	3.15	63.2
SiC-10BN	4.3	0	1.318	3.09	42.7
	4.3	30	1.420	3.09	46.0
	4.3	60	1.532	3.09	49.6

Table 9. Densities of samples sintered with different holding times, measured using Archimedes' principle in water

Powder	Pressure [MPa]	Holding time at 2050°C [min]	Measured density [g/cm^3]	Theoretical density [g/cm^3]	Percent theoretical density [%]
SiC-0BN	20	0	3.087	3.21	96.2
	20	30	3.093	3.21	96.3
	20	60	3.170	3.21	98.7
SiC-5BN	20	0	3.066	3.15	97.3
	20	30	3.072	3.15	97.5
	20	60	3.083	3.15	97.9
SiC-10BN	20	0	3.029	3.09	98.0
	20	30	3.086	3.09	99.9
	20	60	3.090	3.09	100.0

10 Appendix D – Stacked XRD scans

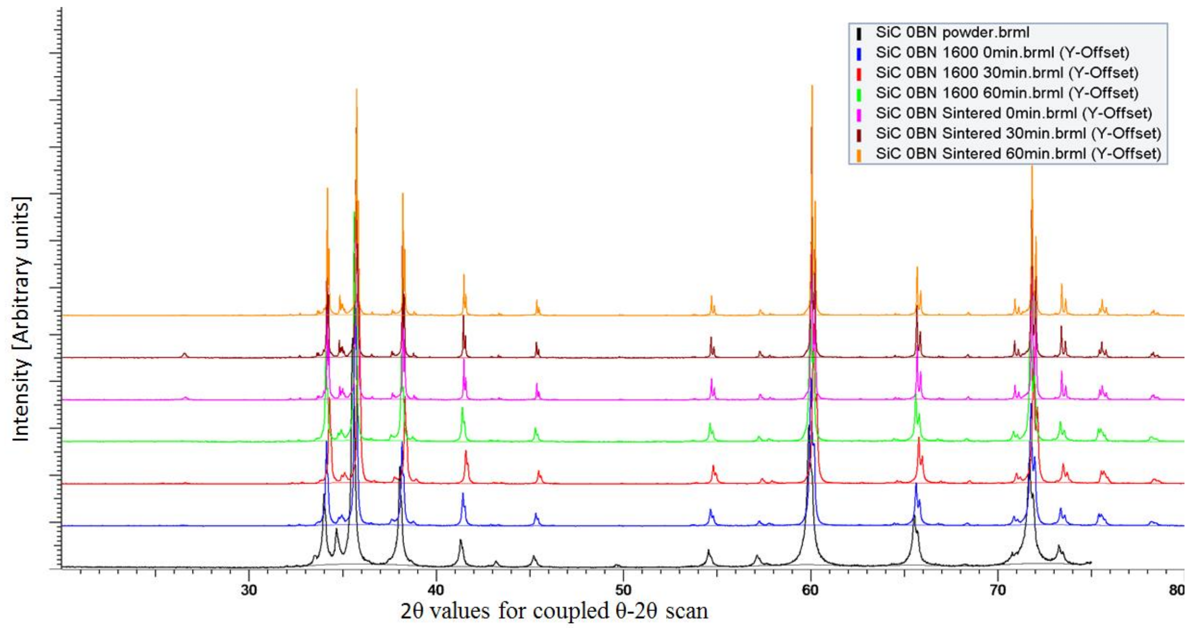

Figure 65. Stacked XRD scans for SiC 0BN.

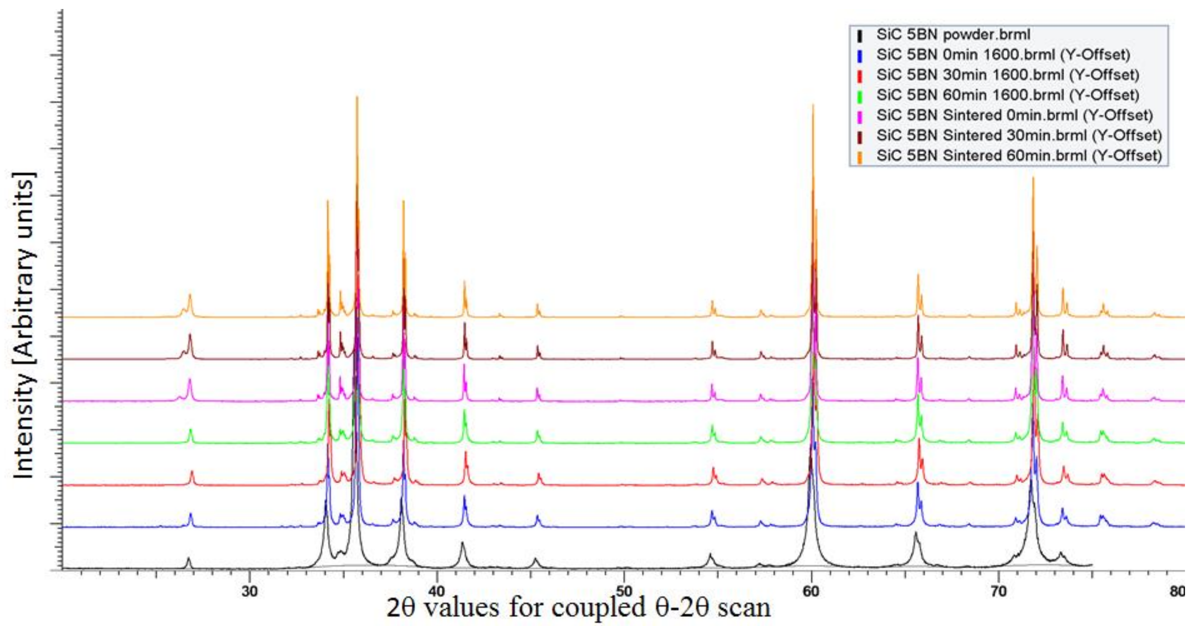

Figure 66. Stacked XRD scans for SiC 5BN.

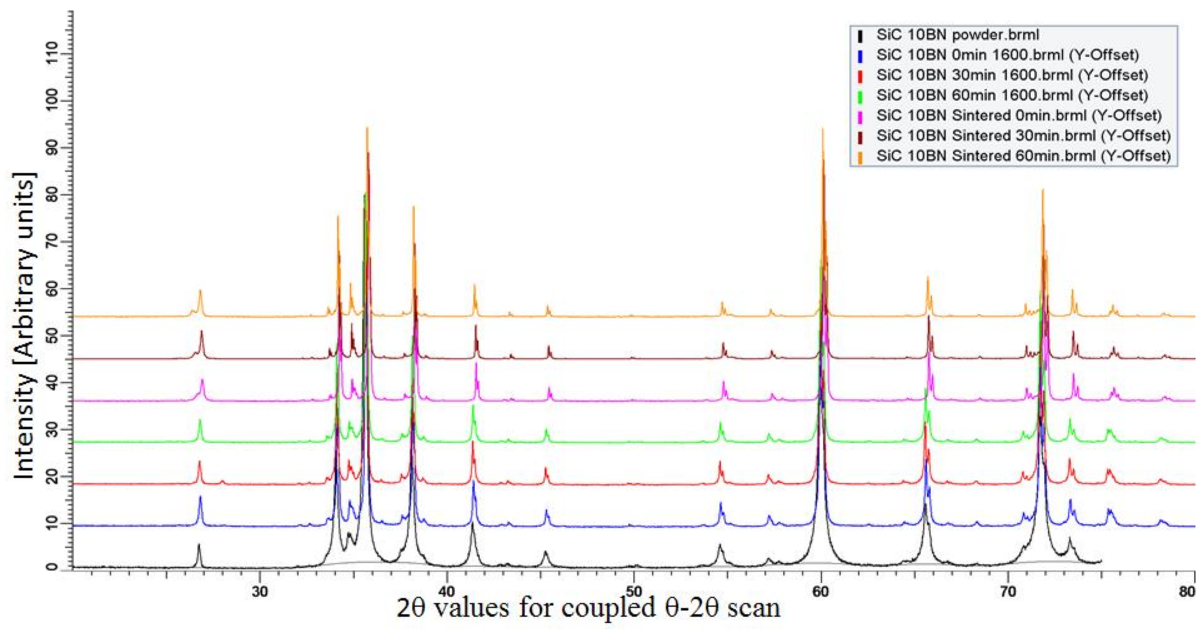

Figure 67. Stacked XRD scans for SiC 10BN.

11 Appendix E – All EBSD figures

All scale bars are 15 µm.

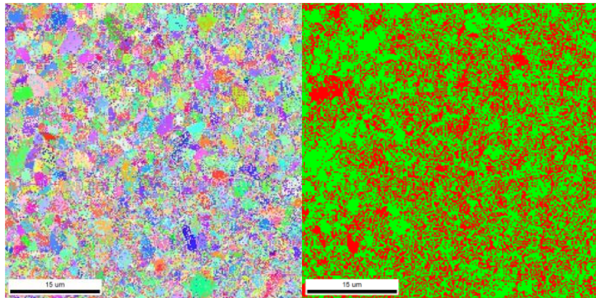

Figure 68. **IPF and phase map for SiC 0BN 0min.**

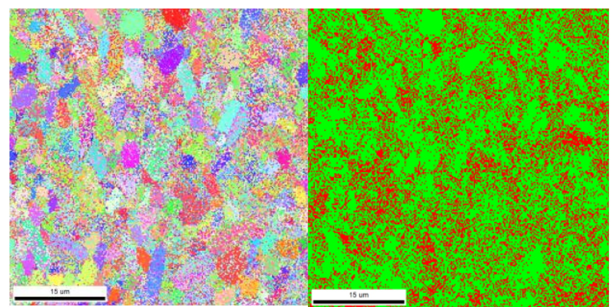

Figure 69. **IPF and phase map for SiC 0BN 30min.**

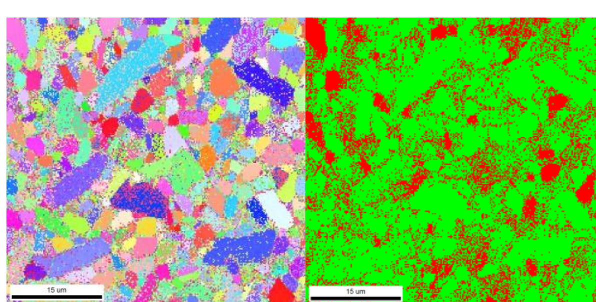

Figure 71. **IPF and phase map for SiC 0BN 60min.**

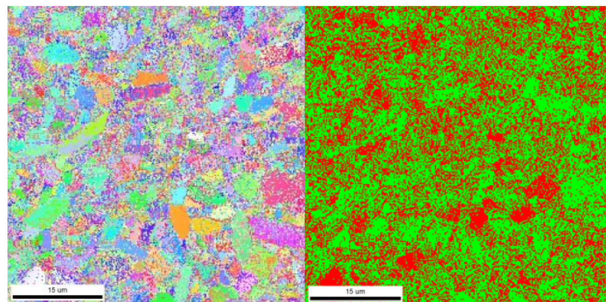

Figure 70. **IPF and phase map for SiC 0BN 60min with viewing angle normal to pressing direction.**

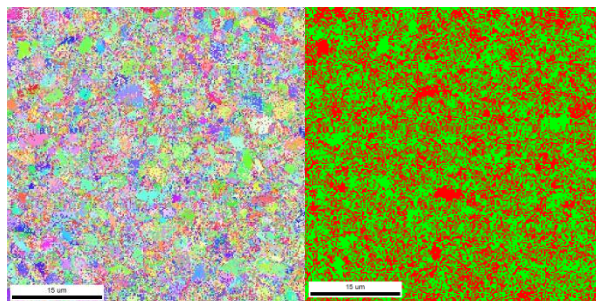

Figure 72. **IPF and phase map for SiC 5BN 0min.**

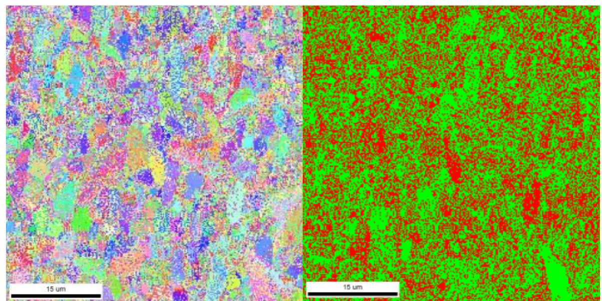

Figure 73. **IPF and phase map for SiC 5BN 30min.**

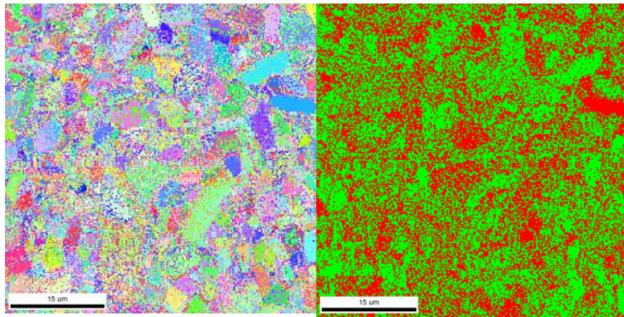

Figure 75. **IPF and phase map for SiC 5BN 60min.**

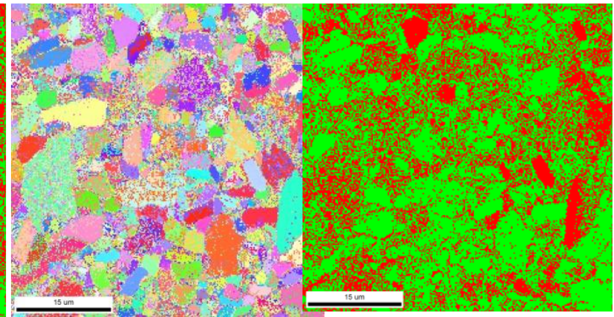

Figure 74. **IPF and phase map for SiC 5BN 60min with viewing angle normal to pressing direction.**

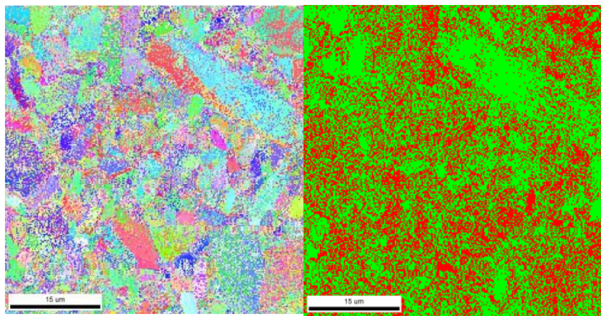

Figure 77. **IPF and phase map for SiC 10BN 0min.**

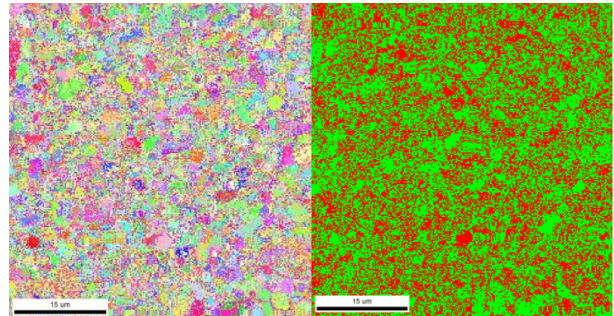

Figure 76. **IPF and phase map for SiC 10BN 30min.**

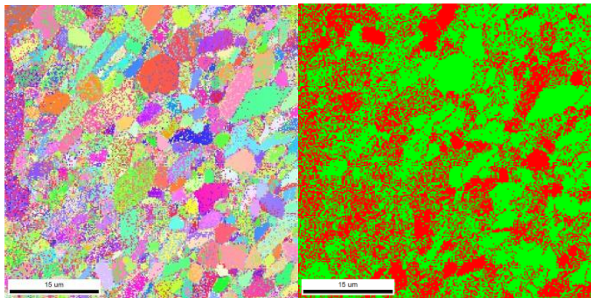

Figure 79. **IPF and phase map for SiC 0BN 60min.**

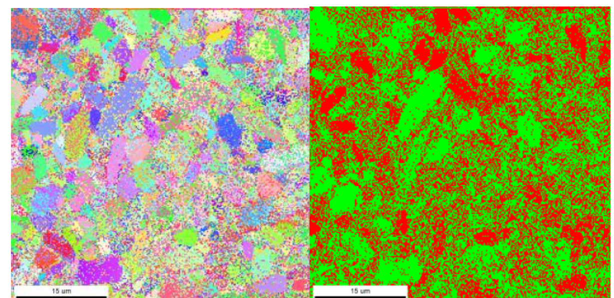

Figure 78. **IPF and phase map for SiC 10BN 60min with viewing angle normal to pressing direction.**

12 Appendix F – Secondary electron images of EBSD surfaces with scanned area highlighted

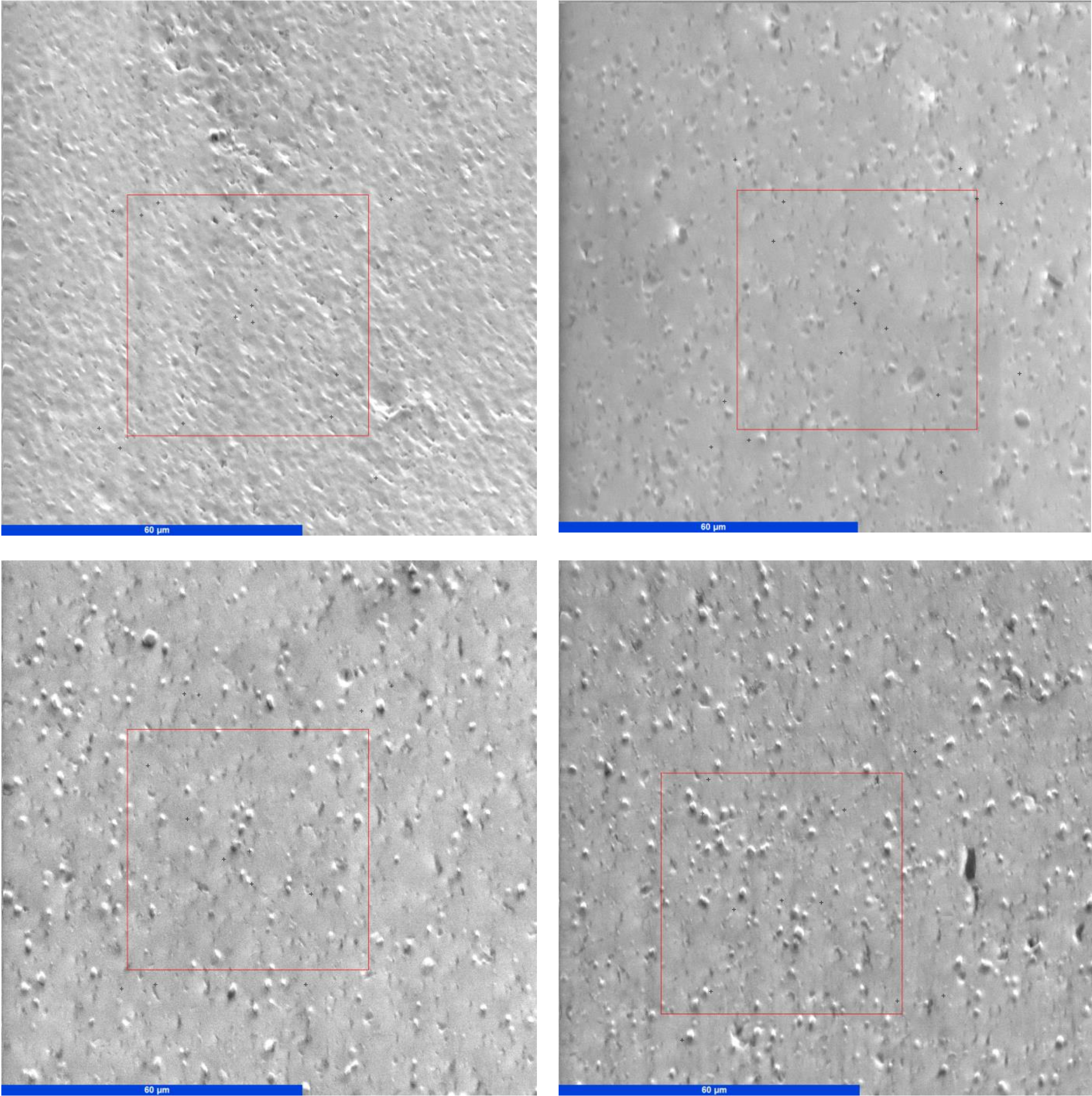

Figure 80. **Electron images of polished SiC 0BN samples with 0min (top left), 30 (top right) and 60 minute (bottom) sintering time. Bottom right is viewed normal to pressing direction, the rest parallel. The red square is the area scanned in EBSD. The scale bar is 60 µm.**

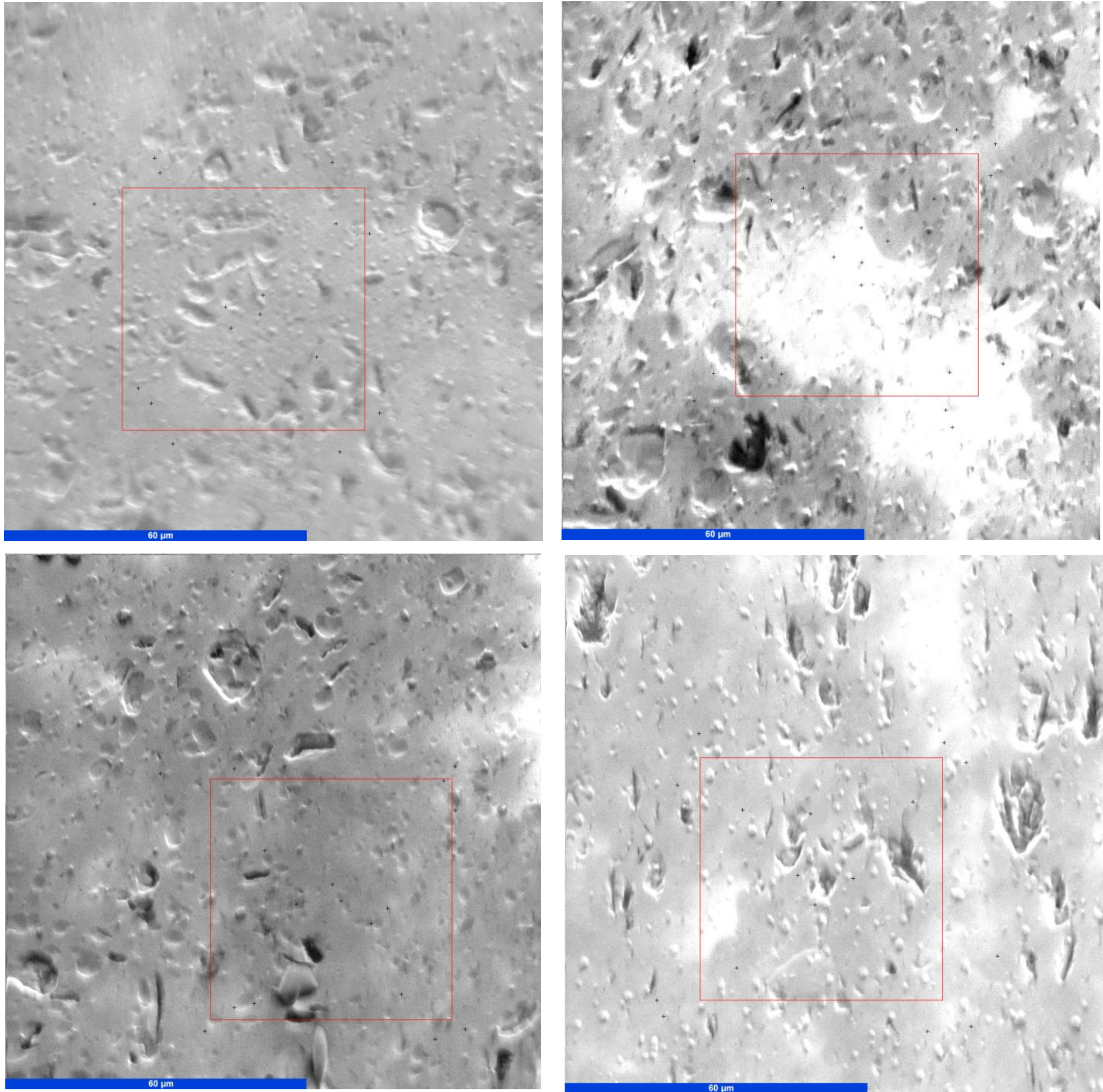

Figure 81. **Electron images of polished SiC 5BN samples with 0min (top left), 30 (top right) and 60 minute (bottom) sintering time. Bottom right is viewed normal to pressing direction, the rest parallel. The red square is the area scanned in EBSD. The scale bar is 60 µm.**

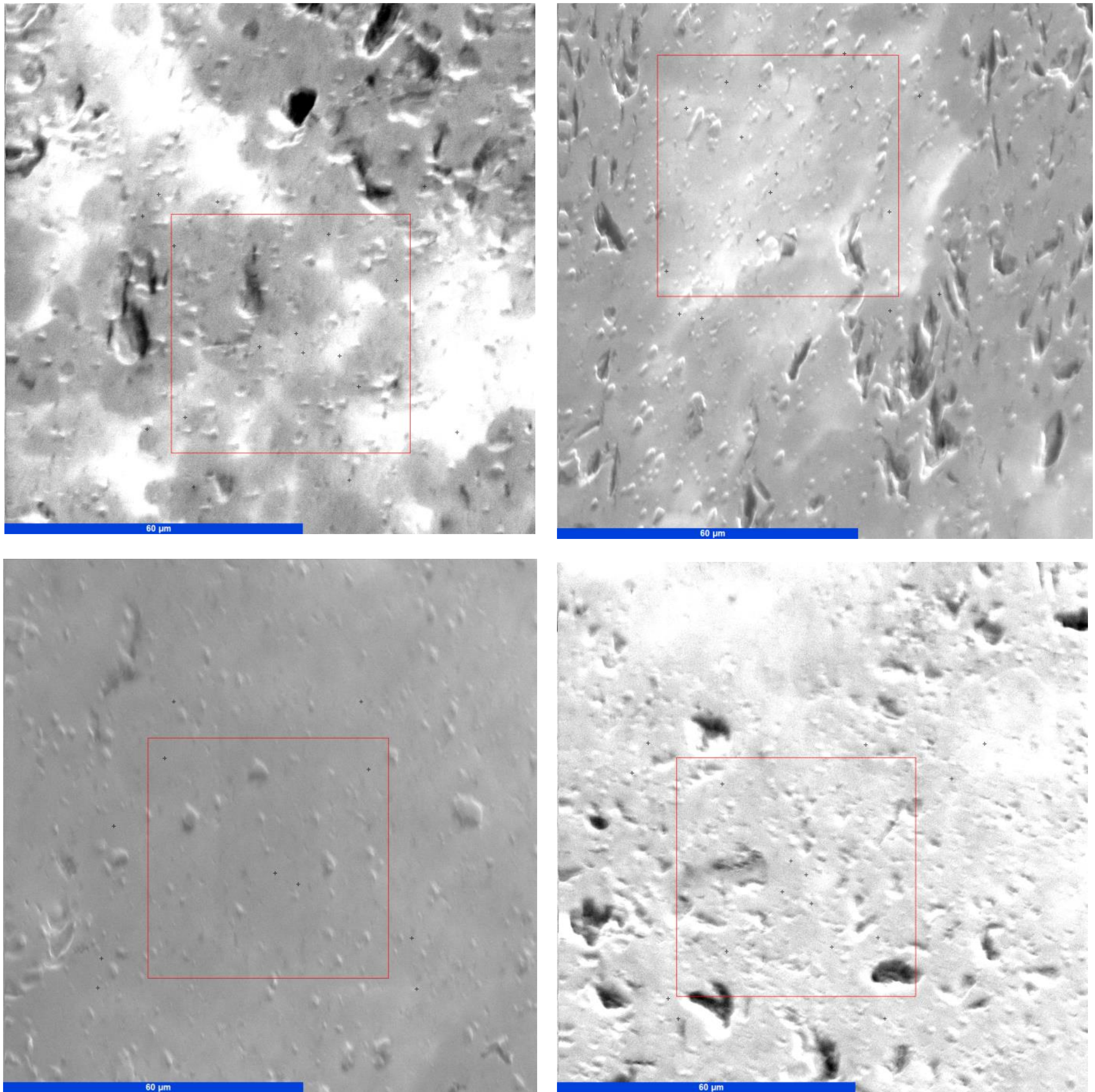

Figure 82. **Electron images of polished SiC 10BN samples with 0min (top left), 30 (top right) and 60 minute (bottom) sintering time. Bottom right is viewed normal to pressing direction, the rest parallel. The red square is the area scanned in EBSD. The scale bar is 60 µm.**

13 Appendix G – Weight percent to atomic percent calculations

Table 10. Wt% to at% conversion for SiC-5BN, using values from SI chemical data [85].

Compound	Wt%	Element	Wt%	Compound molar weight	Element	At%
SiC	91.3	Si	64.0		Si	43.2
B4C	01.2	B	03.1		B	05.4
BN	05.0	C	30.1	22.32	C	47.6
C	02.5	N	02.8		N	03.8

Table 11. Wt% to at% conversion for SiC-10BN, using values from SI chemical data [83].

Compound	Wt%	Element	Wt%	Compound molar weight	Element	At%
SiC	86.3	Si	60.4		Si	39.6
B4C	01.2	B	05.3		B	09.0
BN	10.0	C	28.6	21.77	C	43.8
C	02.5	N	05.7		N	07.6

14 Appendix H – Lattice parameter and d-spacing measurements

Table 12. Lattice parameters for SiC in SiC 0BN, as measured by Rietveld fitting in *Topas*.

Powder name	4H-a [Å]	4H-c [Å]	6H-a [Å]	6H-c [Å]
SiC 0BN powder	3.0754	10.0814	3.0800	15.1137
SiC 0BN 1600 0min	3.0732	10.1001	3.0824	15.1241
SiC 0BN 1600 30min	3.0729	10.0866	3.0823	15.1241
SiC 0BN 1600 60min	3.0708	10.1540	3.0825	15.1253
SiC 0BN 0min	3.0738	10.0866	3.0819	15.1226
SiC 0BN 30min	3.0751	10.0928	3.0818	15.1222
SiC 0BN 60min	3.0753	10.0921	3.0821	15.1236

Table 13. Lattice parameters for SiC in SiC 5BN, as measured by Rietveld fitting in *Topas*.

Powder name	4H-a [Å]	4H-c [Å]	6H-a [Å]	6H-c [Å]
SiC 5BN powder	3.0732	9.9521	3.0819	15.1190
SiC 5BN 1600 0min	3.0782	10.0235	3.0809	15.1162
SiC 5BN 1600 30min	3.0778	10.0866	3.0798	15.1026
SiC 5BN 1600 60min	3.0770	10.0921	3.0807	15.1171
SiC 5BN 0min	3.0785	10.0844	3.0808	15.1176
SiC 5BN 30min	3.0793	10.0818	3.0805	15.1155
SiC 5BN 60min	3.0796	10.0821	3.0804	15.1152

Table 14. Lattice parameters for SiC in SiC 10BN, as measured by Rietveld fitting in *Topas*.

Powder name	4H-a [Å]	4H-c [Å]	6H-a [Å]	6H-c [Å]
SiC 10BN powder	3.0792	10.0896	3.0826	15.1171
SiC 10BN 1600 0min	3.0742	10.1444	3.0811	15.1167
SiC 10BN 1600 30min	3.0764	10.1540	3.0832	15.1287
SiC 10BN 1600 60min	3.0817	10.1005	3.0843	15.1338
SiC 10BN 0min	3.0803	10.0830	3.0813	15.1148
SiC 10BN 30min	3.0805	10.0854	3.0815	15.1198
SiC 10BN 60min	3.0849	10.0961	3.0864	15.1212

Table 15. d-spacing for BN and graphite peaks in SiC 5BN, measured manually in *EVA*.

Powder name	d-spacing BN [Å]	d-spacing graphite [Å]
SiC 5BN powder	3.3341	
SiC 5BN 1600 0min	3.3192	
SiC 5BN 1600 30min	3.3108	
SiC 5BN 1600 60min	3.3199	
SiC 5BN 0min	3.3242	3.3907
SiC 5BN 30min	3.3227	3.3644
SiC 5BN 60min	3.3227	3.3651

Table 16. d-spacing for BN and graphite peaks in SiC 5BN, measured manually in *EVA*.

Powder name	d-spacing BN [Å]	d-spacing graphite [Å]
SiC 10BN powder	3.3287	
SiC 10N 1600 0min	3.3214	
SiC 10BN 1600 30min	3.3262	
SiC 10BN 1600 60min	3.3238	
SiC 10BN 0min	3.3105	3.3397
SiC 10BN 30min	3.3141	3.3557
SiC 10BN 60min	3.3214	3.3732